



# Kent Academic Repository

**Soltani, Shaghayegh (2021) *Pop-Up Stretchable Sensor Designs Using Multiphysics Modelling*. Doctor of Philosophy (PhD) thesis, University of Kent,.**

## Downloaded from

<https://kar.kent.ac.uk/87964/> The University of Kent's Academic Repository KAR

## The version of record is available from

<https://doi.org/10.22024/UniKent/01.02.87964>

## This document version

UNSPECIFIED

## DOI for this version

## Licence for this version

UNSPECIFIED

## Additional information

## Versions of research works

### Versions of Record

If this version is the version of record, it is the same as the published version available on the publisher's web site. Cite as the published version.

### Author Accepted Manuscripts

If this document is identified as the Author Accepted Manuscript it is the version after peer review but before type setting, copy editing or publisher branding. Cite as Surname, Initial. (Year) 'Title of article'. To be published in *Title of Journal*, Volume and issue numbers [peer-reviewed accepted version]. Available at: DOI or URL (Accessed: date).

## Enquiries

If you have questions about this document contact [ResearchSupport@kent.ac.uk](mailto:ResearchSupport@kent.ac.uk). Please include the URL of the record in KAR. If you believe that your, or a third party's rights have been compromised through this document please see our [Take Down policy](https://www.kent.ac.uk/guides/kar-the-kent-academic-repository#policies) (available from <https://www.kent.ac.uk/guides/kar-the-kent-academic-repository#policies>).

# **POP-UP STRETCHABLE SENSOR DESIGNS USING MULTIPHYSICS MODELING**

---

A Thesis Submitted to the University of Kent  
For the Degree of PhD  
In Electronic Engineering

---

**By**  
**Shaghayegh Soltani**  
**January 2021**

## Abstract

Stretchable electronic devices are critical for the future of wearable sensor technology, where existing rigid and non-flexible devices severely limit the applicability of them in many areas. Stretchable electronics extend flexible electronics one step further by introducing significant elastic deformation. Stretchable electronics can conform to curvy geometries like human skin which enables new applications such as fully wearable electronics whose properties can be tuned through mechanical deformation. Much of the effort in stretchable electronics has focused on investigation of the optimum fabrication method to make a trade-off between the manufacturing cost and acceptable performance. Here in this thesis a novel pop-up strain sensor design is introduced and tested.

This technique is simple to use and can be applied to almost all available materials such as metals, dielectrics, semiconductors and different scales from centi-meter to nanoscale. Using this method three main electronic devices have been designed for different applications. The first category is pop-up antennas that are able to reconfigure their frequency response with respect to the mechanical deformation by out of plane displacement. The second category is pop-up frequency selective surface which similarly can change its frequency behaviour due to applied strain. This ability to accommodate the applied stress by three-dimensional (3D) deformation, making these devices ideal for strain sensing applications such as vapor sensing or on skin mountable sensors. Using the advantage of RFID technology in terms of wireless monitoring, the third category has been introduced which is a pop-up capacitor sensor integrating with an RFID chip to detect finger joint bending that can help those patients who are recovering after stroke. The proposed devices have been modelled using COMSOL Multiphysics and Extensive evaluations of the prototype system were conducted on purpose-built laboratory scale test rigs. Both results are in good correlation which makes them applicable for sensing purposes.

## Acknowledgment

Foremost, I would like to express my sincere gratitude to my supervisor *Prof. John C. Batchelor* for the continuous support of my PhD study and research, for his patience, motivation, enthusiasm, and immense knowledge. His guidance helped me in all the time of research and writing of this thesis. My sincere thanks also go to *Dr. Paul Taylor* for his consistent support and guidance during the running of this project and *Dr. Robert Horne* for his encouragement and invaluable recommendations and feedbacks.

Furthermore, I'd like to express my thanks to:

*Simon Jakes* for his technical advice in mechanical design and the excellent practical skills helped produce the sensor designs involved in the research.

*University of Kent* for providing the funding which allowed me to undertake this research.

*My lab mates* for the inspiring discussions throughout my study.

Last but not the least, I would like to thank my *parents* who set me off on the road to this PhD a long time ago and my sister *Niloofar* and my brother-in-law *Amin* for their continuous help throughout this journey. Finally, my special thank goes to my fiancé *Kamel* for his unconditional love and support while I was working on my thesis.

# Contents

<b>Chapter 1 Introduction</b> .....	1
1.1 Background and Motivation.....	1
1.2 Design Strategies of 2D Precursors.....	3
1.2.1 Filamentary Designs of 2D Precursors.....	3
1.2.2 Kirigami Designs of 2D Precursors.....	4
1.2.3 Origami Designs of 2D Precursors.....	4
1.3 Analytic Model for Pop-up Configurations .....	5
1.3.1 Straight Thin Ribbon .....	5
1.3.2 Wavy Thin Ribbon .....	6
1.4 Introduction to COMSOL Multiphysics .....	8
1.5 Technical Challenges in the Use of Current Stretchable Strain Sensors.....	10
1.6 Aim and Objectives of the Research Programme .....	11
<b>Chapter 2 Literature Review</b> .....	14
2.1 Soft Electronics .....	14
2.1.1 Origami Design.....	16
2.1.2 Kirigami Design .....	16
2.1.3 Textile Embedding .....	16
2.1.4 Buckling Techniques .....	16
2.1.4.1 Wrinkling Structures.....	16
2.1.4.2 Wavy 2D Designs.....	18
2.1.4.3 Fully Bonded, Stiff 2D Structures .....	20
2.1.4.4 Fully Bonded, Soft 2D Structures.....	20
2.1.4.5 Selectively Bonded, Rigid 2D Structures .....	20
2.1.4.6 Selectively Bonded, Soft 2D Structures .....	21
2.1.4.7 Island-Bridge Structure.....	22

2.1.4.8 Transforming Beyond 2D .....	23
2.1.4.9 Buckling from 2D to 3D .....	23
2.2 Stretchable Strain Sensors .....	30
2.3 Stretchable Antenna .....	30
2.3.1 Conductive Materials.....	30
2.3.2 Substrate .....	31
2.3.3 Fabrication Techniques for Stretchable Antennas.....	33
<b>Chapter 3 Pop-up Antennas and Pop-up Frequency Selective Surfaces .....</b>	<b>35</b>
3.1 Introduction .....	35
3.2 Highly Flexible Strain Sensor Based on Pop-up Dipole Antenna for On-Body Applications .....	36
3.2.1 Abstract.....	36
3.2.2 Introduction .....	36
3.2.3 Methods .....	37
3.2.4 Results and Discussion .....	38
3.2.5 Summary and Conclusion.....	42
3.3 A Dual-band Strain Sensor Based On Pop-up Half Wavelength Dipole Antenna .....	43
3.3.1 Abstract.....	43
3.3.2 Introduction .....	43
3.3.3 Antenna Design and Results.....	44
3.4 Mechanically Influenced Antennas for Strain Sensing Applications Using Multiphysics Modelling .....	47
3.4.1 Abstract.....	47
3.4.2 Introduction .....	47
3.4.3 Methodology.....	48
3.4.4 Pop-up Convolute Loop Antenna.....	49
3.4.5 Pop-up Multilayer Dipole Antenna .....	50

3.4.6 Summary and Conclusion.....	53
3.5 Antenna-Based Pop-up Vapor Sensor Guided by Controlled Compressive Buckling.....	54
3.5.1 Abstract.....	54
3.5.2 Introduction .....	54
3.5.3 Sensor Design and Working Principle.....	55
3.5.4 Equivalent Circuit Model .....	58
3.5.5 Numerical Results and Discussion .....	61
3.5.6 Experimental.....	66
3.5.7 Summary and Conclusion.....	70
3.6 Pop-up Tunable Frequency Selective Surfaces for Strain Sensing .....	71
3.6.1 Abstract.....	71
3.6.2 Introduction .....	71
3.6.3 Design and Working Principle .....	73
3.6.4 Results and Discussion .....	75
3.6.5 Summary and Conclusion.....	79
<b>Chapter 4 Pop-up Capacitive Sensors .....</b>	<b>80</b>
4.1 Wireless Finger-Worn Strain Sensing Using Passive RFID Technology .....	80
4.1.1 Abstract.....	80
4.1.2 Introduction .....	80
4.1.3 Antenna Design and Numerical Results .....	81
4.1.4 Pop-up Capacitive Sensor Design .....	84
4.1.5 Experiments .....	87
4.1.6 Conclusion .....	89
<b>Chapter 5 Conclusion and Recommendations for Future Works.....</b>	<b>91</b>
5.1 Research Contributions .....	91
5.1.1 Modelling Pop-up Antennas .....	91

5.1.2 Integration of Human Body and Pop-up Antennas .....	92
5.1.3 Integration of Pop-up Capacitive Sensor with RFID Technology .....	92
5.2 Recommendations for Future Research .....	93

## List of Figures

Fig. 1.1 Stretchable strain sensors on curved surface. These sensors allow interfacing with non-planar surfaces . . . . .	1
Fig. 1.2 Schematic illustration of compressive buckling technique in three steps, cutting a 2D precursor, bonding it selectively to an pre-strained elastomeric substrate and finally releasing the substrate to initiate out of plane deformation . . . . .	3
Fig. 1.3 Mechanically guided buckling of thin ribbon-shape precursor . . . . .	3
Fig. 1.4 Compressing buckling of Kirigami-designed 2D . . . . .	4
Fig. 1.5 2D to 3D structural conversion of Origami-designed 2D precursor . . . . .	4
Fig. 1.6 Processing steps for controlled thin film buckling on elastomeric substrate. (a) Pre-strained PDMS with periodic bonded and unbonded patterns. The widths of bonded and unbonded sites are denoted as $W_{\text{bonded}}$ and $W_{\text{unbonded}}$ , respectively. (b) A thin film parallel to the pre-strain direction is attached to the pre-strained substrate. (c) The relaxation of the pre-strain in the support leads to buckles of thin film. (d) Scanning electron microscope (SEM) image of buckled thin films formed using the previous procedures . . . . .	6
Fig. 1.7 Schematic illustration for the theoretical model of geometric configurations of a 3D helix: (a) Top view of a thin ribbon consisting of two arcs. (b) 3D view of the pop-up configuration after compression from the two ends . . . . .	8
Fig. 1.8 (a) Modules involved in the simulation of pop-up sensors using COMSOL. (b) Modelling a flat dipole antenna at 2.4 GHz using RF module. (c) Modelling the antenna deformation using structural mechanics module. (d) Modelling the buckled dipole antenna using RF module. . . . .	9
Fig. 2.1 Schematic illustration of two different bonding strategies on the elastomeric PDMS substrate for wavy structures, that are fully and selectively bonded onto the substrate . . . . .	21
Fig. 2.2 Schematic illustration of the mechanics model of the device island mesh with arc-shaped design . . . . .	23
Fig. 2.3 Strategies of mechanically guided structural designs in stretchable electronics. Structural designs of devices and systems, including wavy designs, island-bridge designs (e.g., arc-shaped, serpentine, 2D spiral, 3D helical), fractal-inspired designs and kirigami strategy. . . . .	25
Fig. 2.4 Wearable and stretchable strain sensor. . . . .	29
Fig. 3.1 Schematic of half wavelength dipole. . . . .	37

Fig. 3.2 Buckled ribbon with different uniaxial strains on the elastomeric substrate. (a) Simulation. (b) Antenna samples, the antenna was tested on forearm. ....	37
Fig. 3.3 Von mises stress for (a) 10%, and (b) 60% strain. ....	39
Fig. 3.4 Numerical and experimental reflection coefficient (dB) of half wavelength dipole antenna versus frequency (GHz) with 0% and 60% strain. ....	40
Fig. 3.5 Resonant frequency shift as a function of the applied strain. ....	41
Fig. 3.6 XY-plane, YZ-plane and XZ-plane of far field gain (dBi) for, (a) 60%, and (b) 0 % strain. (c) Orientation of the antenna on the three-layer human body tissues.....	41
Fig. 3.7 Schematic of the designed dual band half wavelength dipole antenna. ....	44
Fig. 3.8 (a) Numerical and experimental reflection coefficients (dB) of the pop-up half wave dipole antenna versus frequency (GHz) for 0% and 30 % strain in the substrate. (b) Frequency shift versus strain. (c) Von Mises (MPa) stress on the antenna and substrate. (d) Antenna prototype for 10%, 20% and 30% strain in the substrate.....	45
Fig. 3.9 3D assembly of loop precursor. (a) Buckling process. (b) Numerical and experimental studies of two 3D convoluted loop and 3D flower loop antennas with different bonding patterns (red circles), Top: convoluted loop and down: flower-shape loop antennas. ....	49
Fig. 3.10 Experimental and numerical results of reflection coefficient (dB) vs resonant frequency (GHz) for flat wavy loop antenna (30% strained substrate) and convoluted loop antenna (relaxed substrate). The sensor can measure up to 30% biaxial strain through 570 MHz downshift. Linear interpolation was used to obtain the sensing pattern. ....	50
Fig. 3.11 (a) 3D assembly of multi-layer dipole antenna via compressive buckling. (b) Geometrical parameters of the design. (c) Simulation results. (d) A prototype of the design. ....	51
Fig. 3.12 Reflection coefficient as a function of resonant frequency for (a) fully stretched substrate (30% strain) and (b) relaxed substrate (0% strain). ....	52
Fig. 3.13 Geometry of the designed half wavelength dipole antenna.....	56
Fig. 3.14 Schematic illustration of the designed pop-up sensor by mechanically guided 3D assembly through PDMS swelling and deswelling.....	58
Fig. 3.15 (a) Equivalent circuit model used for modeling pop-up dipole antenna. (b) Surface current (A/m) on the buckling dipole after deswelling and returning to the original PDMS size. (c) Diagram of mechanics model for a meander section of a buckled ribbon. ....	60
Fig. 3.16 Resonant frequency as a function of strain value in PDMS ( $\epsilon_{app}$ ). Plot compares the results from numerical simulation in COMSOL and predictions from geometry-based model. Note that $N = 2$ in this study. ....	61

Fig. 3.17 Von Mises stress (MPa) in the antenna and substrate after release of 60% strain in the PDMS.....	62
Fig. 3.18 Resonant frequency shift vs strain value in the PDMS substrate for the half wave length dipole antenna with buckled sections $N = 1$ to $N = 5$ . Inset figure presents reflection coefficient (dB) versus frequency (GHz) for the sensor in the relaxed mode with unswollen PDMS and shows a good antenna match with $N = 2$ and $N = 3$ . ....	63
Fig. 3.19 Number of cycles to failure for the half wavelength dipole antenna on a PDMS substrate after release of 60% strain. ....	65
Fig. 3.20 Reflection coefficient (dB) versus frequency (GHz) for half wave dipole on a PDMS substrate with thicknesses of 0.4, 0.8 and 1mm for 60% strained PDMS and strain-free PDMS substrate. ....	65
Fig. 3.21 (a) Swelling degree vs exposure time for three thicknesses (0.4 mm, 0.8 mm and 1 mm). (b) Fabrication process. Step one, the flat dipole antenna is superglued at six bonding zones (specified with red color). In step two, the antenna is attached to the fully swollen PDMS in the desiccator. Note that all experiments were performed in clean room to ensure the safety and finally in step three, the sample is removed from the desiccator to deswell. At this point due to the induced compressive force, buckled dipole is formed. ....	68
Fig. 3.22 (a) Experimental set up, sensor placement in desiccator. (b) Experimental curve for resonant frequency vs diethyl ether concentration (ppm), Linear correlation between frequency and gas concentration could be used for calibrating the sensor. (c) a comparison of resonant frequency vs gas concentration curve between diethyl ether and acetone.....	69
Fig. 3.23 Pop-up formation procedure of the FSS structure. (a) Elastomeric substrate is under strain (2D unit cells). (b) Substrate is relaxed and 3D unit cells are formed due to induced compressive force. (c) Geometry parameters of each unit cell.....	73
Fig. 3.24 Biaxial stretching of an elastomeric substrate. ....	74
Fig. 3.25 (a) Experimental set-up. (b) FSS prototypes. The right hand side sample has been undergone 50% strain in its elastomeric substrate and the left hand side sample is strain free. ....	76
Fig. 3.26 Numerical and experimental results for resonant frequency shift vs strain values in the elastomeric substrate for normal incidence and TM polarization.....	77
Fig. 3.27 Surface current (A/m) on the buckled crossed dipole. The currents flow in opposite directions on adjacent vertical arms and have cancelling effect leading the structure to be electrically smaller than the actual physical size. ....	77

Fig. 3.28 A comparison between an FSS structure with 3D buckled crossed dipole unit cell and similar flat counterparts with equal periodicity in terms of stability. ....	78
Fig. 3.29 Numerical and experimental results for TE incidence at four angles of $0^\circ$ , $15^\circ$ , $30^\circ$ and $45^\circ$ . (a) 50% strain in the elastomeric substrate (simulation), (b) 50% strain in the elastomeric substrate (experiment), (c) strain-free elastomeric substrate (simulation) and (d) strain-free elastomeric substrate (experiment).....	79
Fig. 4.1 Schematic of the antenna design, (a) dimension parameters of the antenna layout, (b) antenna design on a finger model. ....	82
Fig. 4.2 Finger phantom 4 layer cylindrical model, including bone, tendon, fat, skin and the mounted tag.....	83
Fig. 4.3 (a) Reflection coefficient versus frequency (S11). The antenna resonates at 866 MHz with the bandwidth of $\sim 15$ MHz. (b) Simulated realized gain plot for the ring (diameter:-21 mm). (c) Simulated surface current for the single finger phantom.....	84
Fig. 4.4 Geometry of the capacitive sensor.....	86
Fig. 4.5 Schematic of pop-up capacitor sensor on hand phantom. (a) When finger is straight ( $\theta = 0^\circ$ ), (b) ( $\theta = 30^\circ$ ), (c) ( $\theta = 60^\circ$ ) .....	86
Fig. 4.6 Fabrication route of the capacitive sensor on finger phantom.....	87
Fig. 4.7 Schematic of finger joints modelled with hinges in Comsol Multiphysics.....	87
Fig. 4.8 Sensor prototype. (a) Straight finger, (b) 22.5 degree bending, (c) 45 degree and (d) 90 degree corresponding to fully bent finger. ....	87
Fig. 4.9 Sensor code versus different degrees of finger bending. Inset graph illustrates a comparison between capacitance values obtained by simulation and experiment using the tag provider sample as reference [188]. This difference is mainly due to introduction of electrodes. ....	87
Fig. 4.10 Read range of the sensor on candidate 1 at different levels of finger bending.....	90

## List of Tables

Table 2.1 A comparison of the current stretchability methods.....	37
Table 3.1 Dimension parameters of the antenna design. ....	37
Table 3.2 Properties of a three-layer model of human body.....	38
Table 3.3 Dimension parameter of the antenna design.....	44
Table 3.4 Parameter for antenna design.....	49
Table 3.5 Dimensions of the designed multi-layered antenna. ....	51
Table 3.6 Matched frequency bands, simulated gain and simulated total efficiency of the 3D multi-layered antenna as a function of sensing strain. ....	52
Table 3.7 Parameters for the designed antenna. ....	56
Table 3.8 Properties of the substrate used in the sensor design.....	56
Table 3.9 Maximum stress level in the PDMS substrate with different thicknesses. ....	65
Table 3.10 Summary of measure .....	67
Table 3.11 Comparison with other works.....	68
Table 3.12 Parameters for the designed FSS .....	74
Table 4.1 Dimension values of the antenna structure. ....	82
Table 4.2 Electrical properties of different layers of the finger phantom.....	83
Table 4.3 Dimension values of the capacitive sensor design.....	86

## Nomenclature

Symbol	Meaning
$A$	Buckling amplitude
$C$	Capacitance
$I_i$	Cauchy-Green invariants
$\epsilon_{comp}$	Compressive strain
$\epsilon_c$	Critical strain
$L_{rib}$	Distance between bonding sites after compression
$L$	Inductance
$c_i$	Mooney-Rivlin parameter
$\epsilon_{pre}$	Pre-strain
$f_0$	Resonant frequency
$W$	Strain energy density function
$L_{rib}^0$	Total length of the ribbon
$T_g$	Transition temperature
$W_{bonded}$	Width of bonded areas
$W_{unbonded}$	Width of unbonded areas

## List of Abbreviations

<b>Abbreviation</b>	<b>Meaning</b>
<b>CP</b>	Circular Polarization
<b>ELD</b>	Electroless Deposition
<b>FEA</b>	Finite Element Analysis
<b>FSS</b>	Frequency Selective Surface
<b>GWF</b>	Graphene Woven Fabric
<b>LIG</b>	Laser-Induced Graphene
<b>LCP</b>	Liquid crystal polymer
<b>MEMS</b>	Micro-Electromechanical systems
<b>NFC</b>	Near Field Communication
<b>NWCF</b>	Non-Woven Conductive Fabrics
<b>PML</b>	Perfectly Matched Layer
<b>PET</b>	Polyethylene terephthalate
<b>PDMS</b>	Polydimethylsiloxane
<b>PI</b>	Polyimide
<b>RFID</b>	Radio Frequency Identification
<b>3D</b>	Three dimensional
<b>TM</b>	Transverse Magnetic wave
<b>TE</b>	Transverse Electric wave
<b>2D</b>	Two dimensional
<b>UHF</b>	Ultra High Frequency
<b>WLAN</b>	Wireless Local Area Network

## List of published or submitted papers

- 1- **S. Soltani** and J. C. Batchelor, "Highly flexible strain sensor based on pop-up dipole antenna for on-body applications," *The Loughborough Antennas & Propagation Conference (LAPC 2018)*, Loughborough, 2018, pp. 1-4.
- 2- **S. Soltani**, P. S. Taylor, J. C. Batchelor, A Dual-band Strain Sensor Based On Pop-up Half Wavelength Dipole Antenna, *Antenna, IEEE international Symposium on Antennas and Propagation (APS/URSI 2019)*, Atlanta, Georgia, USA, 2019.
- 3- **S. Soltani**, P. S. Taylor, J. C. Batchelor, Mechanically Influenced Antennas for Strain Sensing Applications Using Multiphysics Modelling, *14th European Conference on Antennas and Propagation, EuCAP 2020*, Copenhagen, Denmark.
- 4- **S. Soltani**, A. J. R. Hillier, S. J. Holder and J. C. Batchelor, "Antenna-Based Pop-up Vapor Sensor Guided by Controlled Compressive Buckling," in *IEEE Sensors Journal*, vol. 20, no. 50, 2020.
- 5- **S. Soltani**, P. S. Taylor, E. A. Parker and J. C. Batchelor, "Pop-up Tunable Frequency Selective Surfaces for Strain Sensing," in *IEEE Sensors Letters*, vol. 4, no. 4, pp. 1-4, April 2020.
- 6- **S. Soltani**, P. S. Taylor, J. C. Batchelor, "Wireless Finger-Worn Strain Sensing Using Passive RFID Technology", in *IEEE Journal of Radio Frequency Identification*. Submitted.

# Chapter 1

## Introduction

### 1.1 Background and Motivation

The great majority of effort in electronic industry has been focused on miniaturized and fast-responsive devices. However, these devices are limited to planar rigid silicon wafers. Over the past decade a new study direction has been emerged which is stretchable electronics. This technology offers the performance of conventional rigid devices with mechanical properties of a rubber band which can be stretched, bent and twisted. This ability enables many new applications, mainly the close integration of electronics with human body or curved surfaces. Examples include wearable health monitors [1], stretchable strain gauge [2], energy harvester [3], as shown in Fig. 1.1.

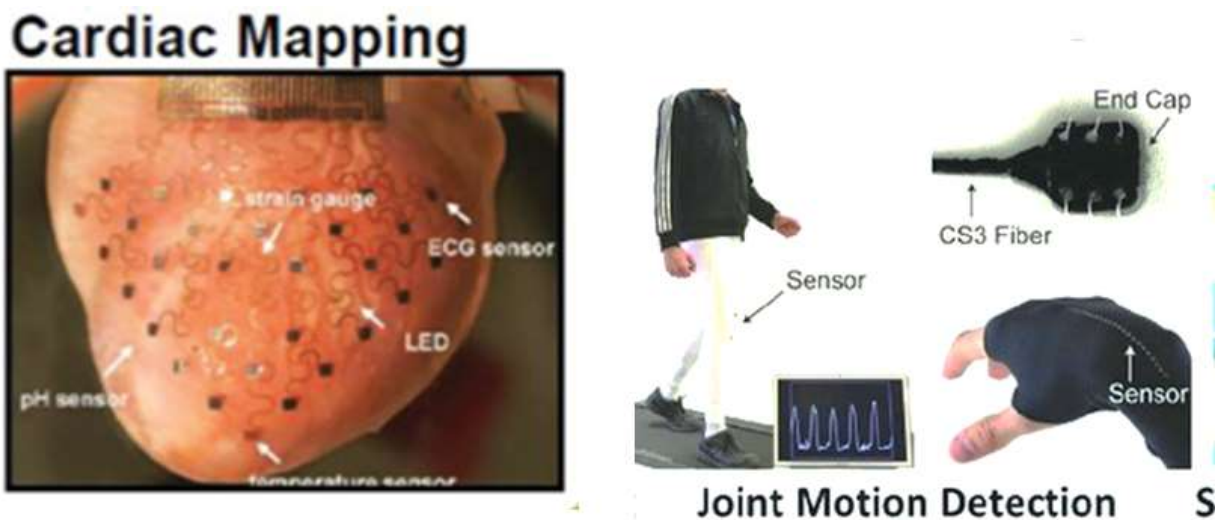


Fig. 1.1 Stretchable strain sensors on curved surface. These sensors allow interfacing with non-planar surfaces [1],[2].

The main challenge in this area is the mismatch between the mechanical properties of soft and elastic requirements of applications and the intrinsic hard and rigid features of electronic components. Several mechanical strategies have been developed to make rigid electronic components stretchable on elastomeric substrates. Among all, the most effective route is structural design approach which bestows stretchability to those intrinsically rigid components by buckling or twisting in order to absorb the extra strain. Moreover, nearly all micro/nano-

systems found in biology and generally in nature have three-dimensional (3D) structures which requires similar 3D architectures in man-made devices for applications in biomedicine, sensing, energy storage and electronics and many other areas of advanced technology. Great efforts have been devoted to the development of 3D electronics, through either direct 3D fabrication or indirect 3D assembly. Direct technologies including microfabrication or 3D printing are typically constrained by the accessible range of sophisticated 3D geometries, limited selection of material, the complexity of the fabrication processes, manufacturing cost, electrical and mechanical properties of electronic materials, printing speed and accuracy. As an alternative route, 3D assembly methods make full use of mature planar technologies to form predefined 2D precursor structures in the desired materials and sizes, which are then transformed into targeted 3D structures by mechanical deformation. This technique is compressive buckling, and the strategy is similar to pop-up books.

This method can bypass some of the challenges encountered by direct 3D fabrication. For example, the 3D assembly methods apply well to nearly any type of advanced electronic materials, including but not limited to metallic conductors, semiconductors, dielectrics and 2D materials such as graphene. Moreover, a diversity of 3D geometries can be formed using 3D assembly methods, through strategic mechanical deformations of engineered 2D precursor structures. This geometric diversity can be regarded as an advantage over the direct 3D fabrication methods of semiconductor materials. Buckling assembly methods rely on a deformable substrate to serve as the assembly platform, which provides the mechanical forces needed to drive the 3D assembly. This assembly process consists of three key steps: 2D precursor fabrication and then selective bonding to pre-strain elastomeric substrate and finally release of the substrate which generates compressive forces at the bonding sites. This assembly process can be controlled by several key factors, such as the patterns of 2D precursors, the strain distributions of supporting substrates, and the paths of strain release. Fig. 1.2 shows a schematic of the working strategy of compressive buckling technique in making pop-up structures.

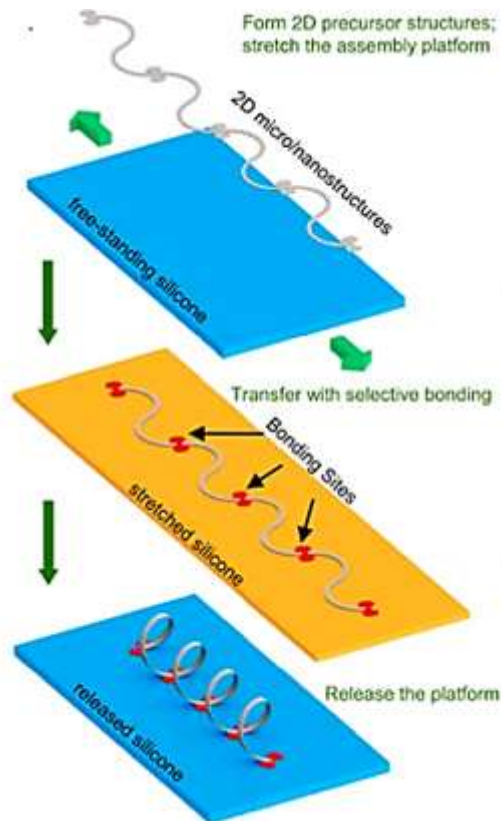


Fig. 1.2 Schematic illustration of compressive buckling technique in three steps, cutting a 2D precursor, bonding it selectively to an pre-stained elastomeric substrate and finally releasing the substrate to initiate out of plane deformation [3].

## 1.2 Design Strategies of 2D Precursors

### 1.2.1 Filamentary Designs of 2D Precursors

Filamentary structures typically consist of thin ribbons with the thickness much smaller than the width, and the width much smaller than the arc length. Such geometric features ensure that the filamentary structures are governed by out-of-plane bending deformations with respect to the width direction. By exploiting different 2D filamentary geometries or bonding sites, different structures can be achieved, as illustrated in Fig. 1.3.

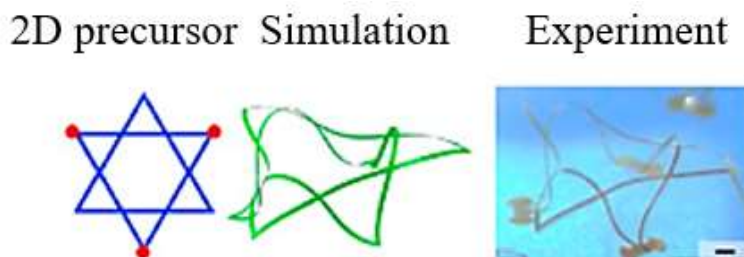


Fig. 1.3 Mechanically guided buckling of thin ribbon-shape precursor [4].

### 1.2.2 Kirigami Designs of 2D Precursors

The kirigami strategy can enable the formation of diverse 3D membrane structures with strategically designed cut patterns. One of the advantages through use of the kirigami strategy is the evident reduction of stress concentration during the buckling assembly. In fact, structures without radial cuts undergo obvious folding creases, and thereby, the maximum strain is much larger than the one with radial cuts. Another advantage of the kirigami strategy is the high design flexibility, which is useful for controlling the curved geometry during the buckling assembly, as shown in Fig. 1.4.



Fig. 1.4 Compressing buckling of Kirigami-designed 2D [4].

### 1.2.3 Origami Designs of 2D Precursors

This approach relies on a spatial variation of thickness in the initial 2D structures as an effective strategy to produce engineered folding creases during the compressive buckling process. The main difference here is that the 2D precursor includes engineered variations in thickness to initiate folding deformations at specific desired locations. Fig. 1.5 illustrates a ribbon (length  $L$  excluding the bonding locations) including five segments, two of which are thicker than the other three (in grey colour). When the thickness ratio ( $t_2/t_1$ ) is relatively small, the thick segments undergo negligible deformation while the thin ones absorb the stress via folding.

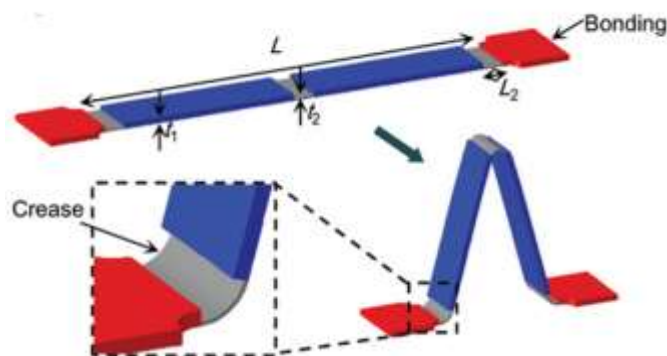


Fig. 1.5 2D to 3D structural conversion of Origami-designed 2D precursor [4].

## 1.3 Analytic Model for the Pop-up Configurations

### 1.3.1 Straight Thin Ribbon

Formation of pop-up structures using compressive buckling technique follows from a process of controlled Euler buckling. The whole structure is comprised of elastomeric substrate and very thin copper ribbons. Here the bonding sites on the elastomeric substrate activated using super glue. However, in smaller scales such as micro/nano scales this activation is usually selectively activated with UV/ozone exposure or by oxygen plasma treatment to allow chemical bonding to thin ribbon upon contact, while the inactivated region adhere by weak van der Waals interactions. The widths of bonded and unbonded sites are denoted as  $W_{bonded}$  and  $W_{unbonded}$ , respectively, as shown in Fig 1.6 (a). Thin film ribbons oriented parallel to the pre-strain direction are attached to the pre-strained elastomeric substrate, as illustrated in Fig 1.6 (b). The relaxation of the pre-strain in the support leads buckling of these ribbons due to the physical separation of the ribbons from the unbonded sites, as presented in Fig 1.6 (c) and 1.6 (d), [4].

Theoretical analysis shows that the buckling profile can be expressed by a sinusoidal function as [5] :

$$w = \begin{cases} w_1 = \frac{1}{2}A \left(1 + \cos \frac{\pi x}{2}\right) & -L_1 < x < L_1 \\ w_2 = 0 & L_1 < |x| < L_2 \end{cases} \quad (1.1)$$

Where  $w_1$  and  $w_2$  are the height of unbonded and bonded parts,  $A$  is the buckling amplitude,  $2L_1$  is the buckling wavelength, and  $2L_2$  is the total length of bonded and unbonded regions after relaxation, as seen in Fig 1.6.

$$A = \frac{4}{\pi} \sqrt{L_1 L_2 (\varepsilon_{pre} - \varepsilon_c)} \approx \frac{2}{\pi} \frac{\sqrt{w_{unbonded} (w_{unbonded} + w_{bonded}) \varepsilon_{pre}}}{1 + \varepsilon_{pre}} \quad (1.2)$$

where  $\varepsilon_c = h_f^2 \pi^2 / 12 L_1^2$  is the critical strain to initiate the buckling and is much smaller than the pre-strain ( $\varepsilon_{pre}$ ) in practical applications. Based on this equation, the amplitude is independent of the mechanical properties and the ribbon thickness and is mainly dependent on the pre-strain ( $\varepsilon_{pre}$ ) and the bonding sites configuration. The peak strain in the buckled thin film is  $\varepsilon_{peak} \approx \pi \frac{h_f}{L_1} \sqrt{\frac{L_2}{L_1} \varepsilon_{pre}}$ , which is typically much smaller than the pre-strain.

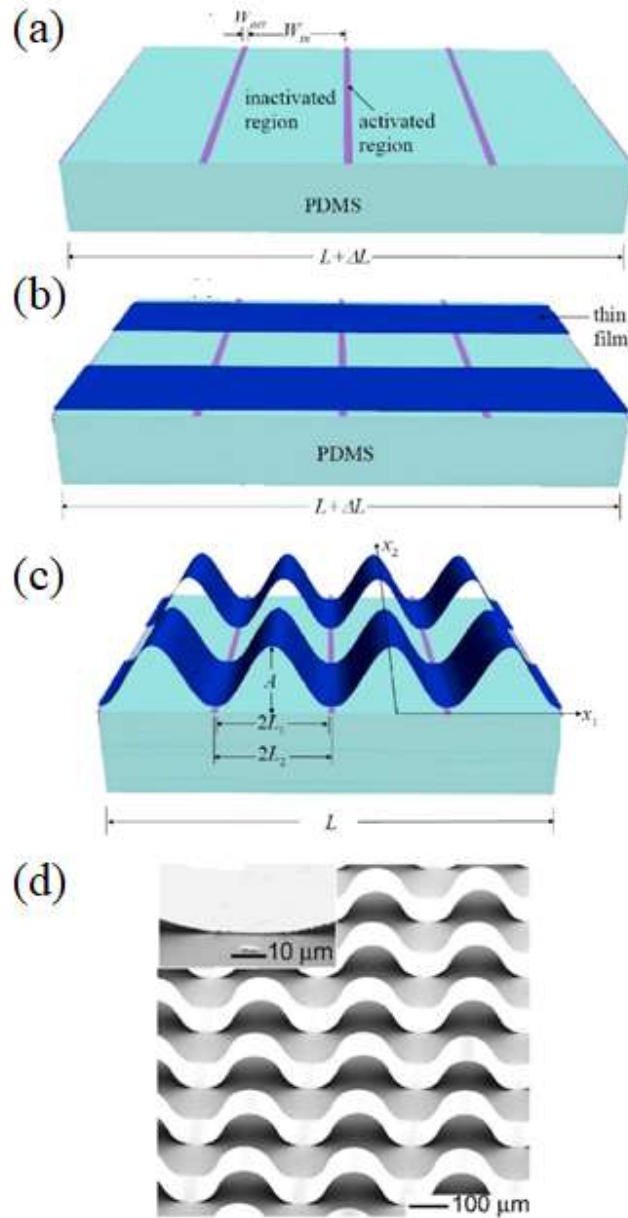


Fig. 1.6 Processing steps for controlled thin film buckling on elastomeric substrate. (a) Pre-strained PDMS with periodic bonded and unbonded patterns. The widths of bonded and unbonded sites are denoted as  $W_{bonded}$  and  $W_{unbonded}$ , respectively. (b) A thin film parallel to the pre-strain direction is attached to the pre-strained substrate. (c) The relaxation of the pre-strain in the support leads to buckles of thin film. (d) Scanning electron microscope (SEM) image of buckled thin films formed using the previous procedures [4].

### 1.3.2 Wavy Thin Ribbon

The 3D helical structures as very attractive designs in stretchable electronics offer structural design with exceptionally high elastic stretchability. The 3D helical layouts involve only minor physical coupling to the substrate, and therefore, can effectively suppress the induced compressive strain concentrations through more uniform 3D spatial deformations. A Cartesian coordinate system has its origin at the left end of the wire, where the  $x$  and  $z$  axes correspond to the axial and out-of-plane direction of the serpentine wire. A parametric coordinate  $\theta$  denotes

the location of the central axis of the arcs, such that  $\theta \in [0, \theta_0]$  and  $[\theta_0, 2\theta_0]$  represent the first and second arc, respectively. The 2D configuration wavy ribbon can be denoted as follows [6]:

$$\begin{cases} x = r_0[\sin(\frac{\theta_0}{2}) - \sin(\frac{\theta_0}{2} - t)] \\ y = r_0[\cos(\frac{\theta_0}{2} - t) - \cos(\frac{\theta_0}{2})] \\ z = 0 \end{cases} \quad 0 \leq t \leq \theta_0 \quad (1.3)$$

$$\begin{cases} x = r_0[3 \sin(\frac{\theta_0}{2}) + \sin(\frac{\theta_0}{2} - t)] \\ y = r_0[\cos(\frac{\theta_0}{2} - t) - \cos(\frac{\theta_0}{2})] \\ z = 0 \end{cases} \quad \theta_0 \leq t \leq 2\theta_0$$

Upon release of the pre-strain ( $\varepsilon_{pre}$ ), the thin ribbon undergoes compressive strain,  $\varepsilon_{comp} = \varepsilon_{pre}/(1 + \varepsilon_{pre})$  leading to its buckling. This process can release the relatively large strain energy associated with in-plane bending. During this post-buckling process, the displacement ( $v$ ) along y axis is negligible since the compression lies along the x axis ( $u$ ) and the buckling mainly induces out-of-plane displacements, along the z axis ( $w$ ). Based on these observations, the deformed configuration of the 3D helix can be written as:

$$\begin{cases} x = \frac{r_0}{1 + \varepsilon_{pre}} [\sin(\frac{\theta_0}{2}) - \sin(\frac{\theta_0}{2} - t)] + \frac{C(\theta_0)\varepsilon_{pre}r_0}{1 + \varepsilon_{pre}} \sin \frac{\pi t}{\theta_0} \\ y = r_0[\cos(\frac{\theta_0}{2} - t) - \cos(\frac{\theta_0}{2})] \\ z = br_0[1 - \cos \frac{\pi t}{\theta_0}] \end{cases} \quad 0 \leq t \leq \theta_0 \quad (1.4)$$

$$\begin{cases} x = \frac{r_0}{1 + \varepsilon_{pre}} [3 \sin(\frac{\theta_0}{2}) + \sin(\frac{\theta_0}{2} - t)] + \frac{C(\theta_0)\varepsilon_{pre}r_0}{1 + \varepsilon_{pre}} \sin \frac{\pi t}{\theta_0} \\ y = r_0[\cos(\frac{\theta_0}{2} - t) - \cos(\frac{\theta_0}{2})] \\ z = br_0[1 - \cos \frac{\pi t}{\theta_0}] \end{cases} \quad \theta_0 \leq t \leq 2\theta_0$$

The pitch of the 3D helix is  $4r_0 \sin \frac{\theta_0}{2} / (1 + \varepsilon_{pre})$ . Because the wire is highly flexible, its membrane strain can be neglected, such that the total arc length along the central axis will remain unchanged during the post-buckling. The associated requirement can be written as:

$$2 \int_0^{\theta_0} \sqrt{\left(\frac{dx}{dt}\right)^2 + \left(\frac{dy}{dt}\right)^2 + \left(\frac{dz}{dt}\right)^2} dt = 2\theta_0 r_0 \quad (1.5)$$

which can be re-arranged to: (1.6)

$$\int_0^{\theta_0} \sqrt{\left[ \frac{\cos\left(t - \frac{\theta_0}{2}\right)}{1 + \varepsilon_{pre}} + \frac{C(\theta_0)\varepsilon_{pre}}{1 + \varepsilon_{pre}} \frac{\pi}{\theta_0} \cos \frac{\pi t}{\theta_0} \right]^2 + \sin^2\left(t - \frac{\theta_0}{2}\right) + b^2 \left(\frac{\pi}{\theta_0}\right)^2 \sin^2\left(\frac{\pi t}{\theta_0}\right)} dt = \theta_0$$

By solving equation (1.6) the parameters can be obtained. Fig. 1.7 shows a theoretical model of geometric configurations of a 3D helix.

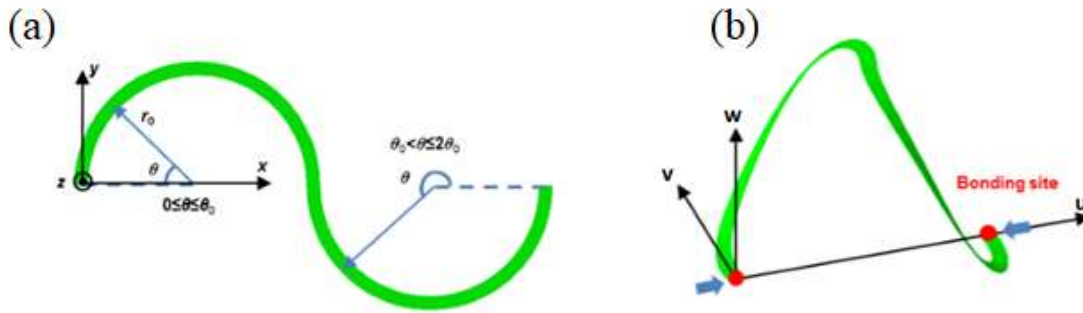


Fig. 1.7 Schematic illustration for the theoretical model of geometric configurations of a 3D helix: (a) Top view of a thin ribbon consisting of two arcs, (b) 3D view of the pop-up configuration after compression from the two ends [6].

## 1.4 Introduction to COMSOL Multiphysics

Full 3D Finite Element analysis (FEA) was adopted to analyse the buckling behaviour of 2D precursors (thin ribbons made of copper) under compressive forces associated with selective bonding to an elastomeric substrate (Dragon Skin or Polydimethylsiloxane (PDMS)) that is released from applied uniaxial or biaxial pre-strain. COMSOL Multiphysics v. 5.3a has been used for numerical simulations in this project, as seen in Fig 1.8. To see how other physics phenomena affect the design, the multiphysics modelling needed. Therefore, in each simulation, different modules have been coupled to achieve a thorough post-buckling analysis in terms of deformation shape, electrical properties and fatigue. The applied modules are as follow [7]:

- **Structural Mechanics module**: This module can analyse the mechanical behaviour of solid structures including for example, stress and strain levels, deformations, stiffness, natural frequencies response to dynamic loads and buckling instability.
- **RF module**: The RF Module is used to understand, predict, and design electromagnetic devices such as antennas. It allows users to quickly and accurately predict electromagnetic field distributions, transmission, reflection, and power dissipation in a proposed design.
- **Nonlinear structural materials module**: Many materials have a nonlinear stress-strain relationship, particularly at higher stress and strain levels. When analysing objects made of such materials, the user needs to consider nonlinearities in the material properties. It is also possible to define a material models based on the defined equations.
- **Multibody dynamics module**: The module enables the user to simulate mixed systems of flexible and rigid bodies, where each body may be subjected to large rotational or translational displacements. User can define Joints and hinges which connect two components through attachments, where one component moves independently in space while the other is constrained to follow a particular motion.
- **Fatigue module**: When structures are subjected to repeated loading and unloading, due to material fatigue, they can fail at loads below the critical limit. A fatigue analysis can be performed in the COMSOL so you can obtain the high-cycle and low-cycle fatigue regimes.

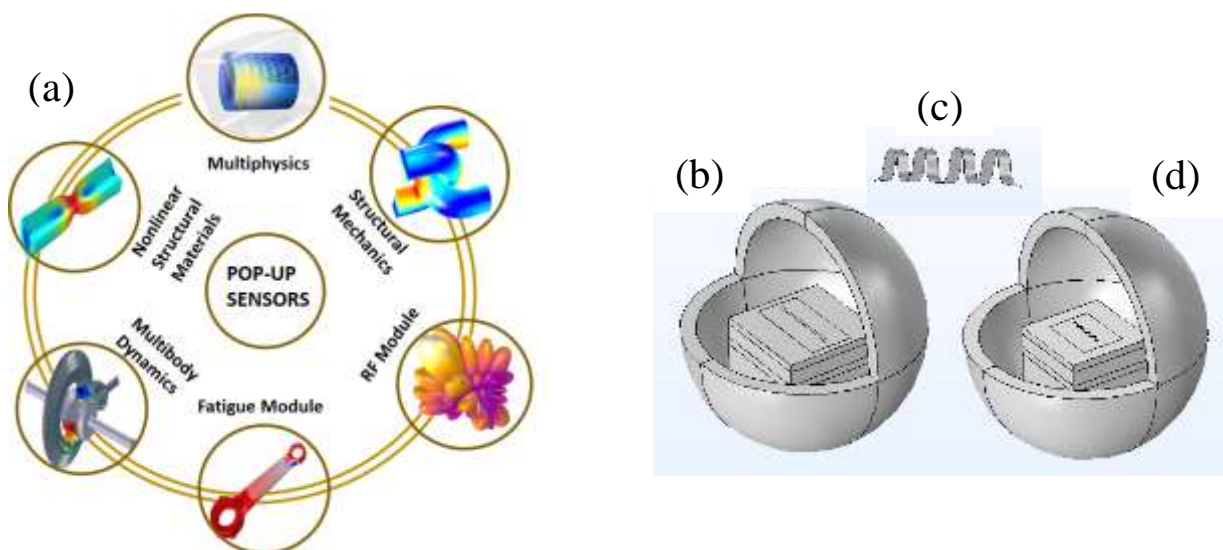


Fig. 1.8 (a) Modules involved in the simulation of pop-up sensors using COMSOL. (b) Modelling a flat dipole antenna at 2.4 GHz using RF module. (c) Modelling the antenna deformation using structural mechanics module. (d) Modelling the buckled dipole antenna using RF module.

In this study, electromagnetic components particularly antenna and FSS devices are developed which leverages controlled compressive buckling to form the devices from patterned 2D precursor structures integrated with an elastomeric substrate. Modelling of the buckling process allows a rational design of mechanically and reconfigurable antennas with desired activation strains applied to the substrate. Combined experimental and computational studies show that the developed antennas can be tuned to operate at a desired discrete frequency when they are flat and can exhibit a wide range of resonant frequency shift (more than 1 GHz) in response to an applied stress by buckling and turning into 3D shape. The design concepts and approaches reported herein could have promising applications in sensing and monitoring applications.

## **1.5 Technical Challenges in the Use of Current Stretchable Strain Sensors**

The development of stretchable strain sensors faces several technical challenges. To ensure that flexible and stretchable strain sensor function properly, the effect of large mechanical deformations on the output signal must be considered. Deformations can degrade the sensor performance by changing the sensitivity, durability and robustness.

The main technical challenges that have been identified are as follows:

- **Trade-off between stretchability and conductivity**

In order to achieve an acceptable level of conductivity for the antenna performance nanomaterial fillers are embedded into the elastomeric matrix to combine the advantages of electrical conductivity of the nanomaterial fillers and mechanical stretchability of the matrix material. To achieve high performance in both mechanical and electrical properties, a balance needs to be maintained between stretchability and conductivity. This is because more fillers used in the elastomeric substrate will increase electrical conductivity while causing the whole composite material to be stiffer. Integration of the two different phases, which typically has very different mechanical properties, presents a significant challenge. Any study in this area must address problems associated with mixing or cracking of the underlying elastomeric layer. Therefore, the selection of materials for fillers and elastomer and their embedding process determines the electrical and mechanical performances of the conductors.

- **Durability**

Flexible electronics are operated with repeated mechanical deformations, including bending, rolling, and twisting, so their mechanical reliability during repeated deformations is a critical factor to reaching real commercial viability. Large deformations beyond a critical strain fracture of the metal layer and repeated small deformations even below a critical strain can also cause mechanical and electrical failure because of metal film fatigue.

Moreover, some other works take advantage of microfluidics in which the liquid metal alloy is injected into silicone microfluidic channels to form stretchable strain sensors based on antennas. In this case, the limitation would be the leakage from microchannels when the antenna is subjected to high stress.

- **Fabrication complexity**

The common fabrication techniques when using intrinsically antenna-based stretchable strain sensors include wet-etching, inkjet printing [8], screen printing [9] and the reported non-planar stretchable antennas have been fabricated using photolithography [10] or 3D printing [11]. Resolution, printing speed, range of useful material and size scale are the main limitations of current fabrication methods and therefore must be taken into account.

- **Manufacturing cost**

The global market demand for high quality and low-cost electronic components requires innovative fabrication techniques that are both faster and cheaper compared to traditional production methods. Photolithography, a complex and time-consuming multiple steps process, requires expensive facilities. Moreover, the photolithographic process generates large volumes of hazardous waste, which damages the environment. Moreover, for printing technology there is always a trade-off between speed and cost.

Till now, development of stretchable strain sensors with both high level of stretchability and high sensitivity is still challenging.

## **1.6 Aim and Objectives of the Research Programme**

The aim of this research is to leverage mechanically guided 3D assembly to design and fabricate stretchable and reconfigurable antennas-based strain sensors whose working frequency can be tuned over a very broad range and therefore can be a good candidate in strain

sensing applications. This recently developed assembly technique has many advantages over current techniques in the area of stretchable electronics. The main advantages are:

- The 3D fabrication process starts from fabrication of 2D precursor structures which is currently well-established.
- In this process there is no limitation in terms of selection of material or size scale.
- There is less complexity in terms of fabrication compared to the literature as a whole set up includes only three steps:  
Cut, stick and release. Step one, **Cut**, denotes designing a desired 2D structure and cut it out of a metal sheet. Step two, **Stick**, denotes the selective bonding of the 2D precursor to the pre-strained elastomeric substrate. Step 3, **Release**, denotes the release of the stretched elastomeric substrate so that initiates the out of plane displacement.
- Our proposed sensor can detect multi-directional strain and multi-deformations due to the 3D structure of it.
- The sensor response is linear, so no complex calibration is involved compared to the reported designs in literature.

This proposed research aligns well with the goal of the communication group at the University of Kent. To achieve this goal, the primary objectives of this research are:

- A review of the main technical approaches for stretchable electronics to date is undertaken. Recent work on electrostatic antennas is summarised in order to highlight progress that has been made in recent years, as well as to identify areas which are still underdeveloped.
- To reveal both the mechanical and electromagnetic principles governing stretchable antennas in order to develop a detailed characterisation of their operation.
- The design and implementation of low cost, simple to fabricate pop-up antennas and pop-up FSS structures for strain sensing applications. Two main applications have been studied, vapor sensing and on-body applications.
- The design, simulation and implementation of pop-up capacitive sensor integrated with RFID technology for on-finger application to enable wireless sensing of finger bending or those patients who suffer partial paralysis.
- To evaluate the performance of the prototype sensors and the effectiveness of the sensing measurements through extensive experiments and cyclic loading in order to ensure durability.

The thesis is organised in five chapters and a brief summary of each chapter is depicted as follows:

- **Chapter 2** provides a comprehensive literature survey concerning the stretchable electronics and the fabrication techniques that were developed during recent decades. Fabrication methods and techniques based on a variety of mechanical principles are introduced along with their relative strengths/weaknesses.
- **Chapter 3** introduces the mechanical and electromagnetic principles of the pop-up antennas and FSS structures for gas sensing and skin mounting application. The sensing mechanism, modelling and characteristics of pop-up sensors are also presented and discussed. This Chapter includes five published papers of the author in this area of working. More explanation has been added to each paper when there was a need to provide more details.
- **Chapter 4** is a detailed discussion of a pop-up capacitive sensor integrated with a passive UHF radio frequency identification tag design which can detect the level of finger bending. The design includes a small loop antenna coupled to a pop-up capacitive sensor. This chapter includes a submitted paper of the author.
- **Chapter 5** draws together and concludes the research findings and their impacts in the field of stretchable antennas for strain sensing. Recommendations for future research and further applications of the developed technique are proposed.

## Chapter 2

# Literature Review

---

### 2.1 Soft Electronics

Soft electronics as substitutes for the rigid and bulky electronic counterparts have attracted great interest in recent years. These electronics allow us to build flexible circuits and devices on a substrate that can be bent, twisted, stretched or folded without losing functionality. The development of stretchable sensors, antennas, solar cells, batteries, and circuits is the product of efforts from the multidisciplinary fields of chemistry, bioscience as well as material, mechanical, and electrical engineering, and has drawn the future of electronic devices [12]. The importance of soft electronics integrating with nonplanar objects is significant. First, the close contact between the component and the nonplanar surface will allow high-quality data to be transferred, while with rigid electronics, air gaps at the interface between the component and the object decreases the contact area, and thus introduce noise and artefacts, which weaken the signal quality. Moreover, stretchable, low profile devices can enable wireless sensing, which hold great promise for Internet-of-Thing's technology. In the area of biomedical, which is the major motive of this field, These devices can conformally laminate on the body tissue to remove any motion artefacts and mismatches in mechanical properties created by conventional, rigid electronics while providing accurate, non-invasive, long-term, and continuous health monitoring [12], [13]. Generally, two routes are applied to enable stretchability which is defined as the ability for the fabricated component to be able to endure mechanical strain while maintaining normal functionality : material innovations, which rely on the synthesis of novel deformable or elastic materials that can withstand the intrinsic in-plane strain, and structural designs that adapt previously rigid components to be stretchable by translating the global strain to local bending, twisting or buckling [14]. In other words, structural design approach makes non-stretchable materials into specific structures that can absorb the applied strain without fracturing or any other damage. The first approach for soft electronics is to exploit intrinsically soft materials as building elements. Common building elements that are necessary for conventional rigid electronic devices include conductors, dielectrics, and most importantly, functional materials, e.g., semiconductors. The intrinsically soft counterparts of these building elements have been largely developed recently. Furthermore, attractive features that are absent

in conventional rigid electronics are emerging in their soft counterparts, such as self-healing and stimuli responsibility. The drawback of this approach is the limitation in the selection of the materials and this method often results in low electrical mobility and high electrical resistivity of electronic devices [15]. Hydrogels, liquid metals, conductive polymers, nanomaterials and textiles are examples of soft materials. On the other hand, structural innovations are extendable to a wider selection of materials, as traditional non-stretchable components can simply adapt the specially designed structure to achieve stretchability. Non-stretchable materials, such as metals, semiconductors, and composites, or rigid components, such as electrodes, sensors or integrated circuit chips, can thus be transformed into stretchable devices after adapting wrinkles, arches, serpentine interconnections in island-bridge structures, or kirigami structures, with little to no compromise in their performance. Moreover, both material innovation and structural innovation can be engineered simultaneously into the same design for obtaining higher stretchability and robustness against mechanical deformation. Structurally stretchable devices can be fabricated with many processes, depending on the selection of materials and requirements of the device. Microfabrication techniques (e.g., photolithography and chemical/physical vapor deposition), subtractive manufacturing (e.g., computer numerical control (CNC) machining and laser ablation), and additive manufacturing (e.g., inject molding, thick-film printing, and 3D printing), have all shown significant potential toward the fabrication of stretchable electronics [16], [17]. Among them, microfabrication techniques have pioneered the development of soft electronics, and related fabrication techniques, mechanical behaviour, and electrical performance have been studied extensively [1], [4]. However, the drawbacks of this process are high cost, limited material selection, complex fabrication procedures and low throughput, which prevent them to enter the market with competitive price and adequate scalability. On the other hand, recent studies have demonstrated the application of shape-changing materials to build soft structures showing various functionalities. These structures can respond to stimuli by expanding, buckling, bending, or actuating for various applications instead of passively enduring mechanical strains. These methods are compatible with a wide range of materials, and can thus serve as alternatives to expensive, complex, non-scalable fabrication methods for the fabrication of such novel, smart, responsive and stretchable structures.

Structural design is a powerful approach for soft electronics. It allows not only enhancing the stretchability of materials that are intrinsically soft, but also bestowing stretchability to materials that are intrinsically rigid. Recent advances in these structural designs have enabled hybridization of all classes of materials, organic or inorganic, soft or rigid, lab-made or

commercial- off-the-shelf, on the same stretchable platform, which combines the electrical properties of conventional rigid devices and the abilities of elastomers to be physically deformed [4]. The main structural designs include: Origami, Kirigami, textile embedding and buckling techniques.

Utilizing substrate engineering, structure design, selective bonding, strain localization and guided buckling strategies, can lead to the planar printing of a variety of devices with diverse wrinkling, textile-embedded, serpentine, and island-bridge structures, as well as to advanced 2D-transformed. The fabrication of such stretchable structures can be applied to a wide range of applications, such as circuit interconnects, physical and electrochemical sensing, energy storage, energy harvesting, soft robotics, and more. We will briefly review various printing strategies for fabricating novel functional structures which is unique compared to other fabrication methods. We will also discuss the combination of multiple fabrication strategies toward the 2D printing of 3D complex structures, which are compatible with a wide range of advanced materials. These capabilities offer an attractive replacement to complex photolithographic and low-throughput 3D-printing technologies. Furthermore, the theoretical limitations, practical challenges, and future of advancing the structural designs in printed devices will be discussed. Addressing the limitations, introducing advanced materials and fabrication strategies, and enhancing the fundamental understanding of printed structures will greatly expand the application of planar printing processes for fabricating a wide range of stretchable electronics.

### **2.1.1 Origami Design**

Origami is an art of paper folding with *ori-* meaning fold and *-gami* meaning paper, which can transform a planar sheet into complex 3D structures according to the predefined patterns. These periodic array of mountain and valley folds, allows the 3D structure to fold and unfold simultaneously without inducing large strain to the functional areas of soft electronics between the creases.

### **2.1.2 Kirigami Design**

Very similar to the origami, kirigami is an art combining paper folding and cutting to create stretchable electronics. Traditional manufacturing methods for assembling origami and kirigami structures mainly rely on manual or machine-assisted folding, which is challenging to implement on small scales and advanced materials [18], [19].

### **2.1.3 Textile Embedding**

Textile is one of the most important platforms for wearable soft electronics. It offers comfort, warmth, flexibility, conformity, and is used widely by human in daily life. Correspondingly, embedding the devices with the textile platform faces many challenges as its durability, flexibility, stretchability, and washability will be considered. Various studies show progress in a “bottom-up” approach where functional materials are fabricated into fibres and fabrics that can be used for energy harvesting, energy storage, and sensing. The device made using this strategy can achieve stretchability by weaving the yarns into tortuous or coiled shapes that fold and unfold during stretching. Planar printing techniques, which is commonly used for applying different patterns and logos onto clothes, can be used to directly print materials onto the textile, in low-cost, high-throughput processes that are compatible with a wide selection of materials. The printing allows the deposition of different inks into the specific location and can thus be used easily to assemble components with the designed shapes into a textile-based device. Two approaches are generally used when using textile as a substrate. The first involves printing a polymer-based lining that forms a smooth and uniform surface on top of the porous and rough textile. In this situation, substrate acts like the common elastomeric substrates. In the second case, the ink is printed directly onto the textile substrate which is nonuniform. As a result, the stretching behaviour, the porosity, and the chemical properties of the textile substrate vary based on the material, thickness, and the weaving of the yarns that make the textile, thus requiring customization to the formulation of the inks [1], [8], [20].

Overall, the main drawback of textile-embedding process is limited resolution due to the nondirectional permeation of ink and the wicking properties of the fibres [1]. Textile embedding method can be remarkably developed in future by more research on the printing resolution by utilizing strategies such as hydrophobicity coating or different ink formulations which allow selective directional ink penetration into the substrate.

### **2.1.4 Buckling Techniques**

#### **2.1.4.1 Wrinkling Structures**

Mechanically induced wrinkling structures are considered as the remarkable upturn of stretchable electronics. The wrinkles can be formed by the mismatch of mechanical properties such as strain between the substrate and the materials, which can be produced by depositing materials onto the substrate after heating or strain-induced expansion and removal. The amplitude, frequency, and shape of the wrinkling waves can be adjusted based on the level of pre-applied tensile strain, the dimensions, thicknesses, the mechanical properties of the

substrate, the deposited material and the adhesion between the two [9], [21]. Specific to printing technologies, which has not been studied in depth, probably due to the complex mechanical property of the applied inks, which are combination of different materials, and vary from study to study. Inks composed of carbon nanotubes (CNTs), conductive polymers, and composites, that share significantly different mechanical properties, can apply such wrinkling strategy to produce stretchable devices. As the deposition usually involves the use of solvents and heat-based curing process after the deposition, heat and solvent-based substrate treatment are not considered compatible with the printing processes. As a result, substrate pre-strain is mostly applied by mechanical stretching. Usually, two techniques are used in the printing of wrinkle structures. The first approach is more traditional, where the substrate is first pre-stretched, followed by the ink deposition and the release of the pre-strain to form wrinkles. The second approach is less common where a wrinkling structure is introduced first, followed by the deposition of inks onto the wrinkled substrate. Similarly, the stretchability of the printed wrinkling structure varies with the level of pre-stretching and the mechanical property of the deposited material, which can be as high as a few hundred percent.

#### **2.1.4.2 Wavy 2D Designs**

The use of 2D designs in stretchable devices make the utilization of geometry possible in the broad context of soft electronics. Patterns that represent the formation of 1D structure into a 2D plane such as triangular wave, square waves, sine waves, serpentine (arcs), or spirals are applied in devices to enable structural stretchability. The 2D designs are usually composed of periodic unit cells with their geometric length longer than their physical sizes, allowing them to respond to strain by twisting, in-plane rotations, and out-of-plane buckling to release their geometric length to compensate for the increased physical length. The concept of fractals or self-similar structures is later introduced using the strategy of substituting basic unit cells with self-similar designs that resemble the full design, aiming to further enhance the structural stretchability by compressing longer 1D structure into a specific 2D area. The fabrication of these wavy 2D designs usually requires high resolution, and is typically done via photolithography, laser ablation, and transfer printing of thin films to constitute the stretchable structures. Based on their application, a selection of materials, such as metals, semiconductors, or dielectrics, can be used to fabricate antennas, interconnects, current collectors, energy harvesters, or actuators [22], [23]. The stretchability of devices utilizing such self-similar patterns depends on several factors, including the mechanical property of the materials, the supporting substrate, and the bonding between the two, as well as the geometric properties such

as the shape, width, thickness, radius, arm length (length of the linear segment within each unit), angle, and is summarized in numerous studies [24], [25]. Most of the method used for fabricating such structures involves transfer-printing of delicate fine features with low mechanical robustness. As a result, the complexity, throughput, and cost of fabricating 2D wavy design via photolithography or laser ablation can be a massive obstacle for their prevalent applications. Nonetheless, due to its simplicity, the strategy of using 2D geometric designs to enable stretchability has been widely applied by the field of stretchable electronics. Compared to photolithography or laser ablation, most of the printing techniques have lower resolution and hence are limited in fabricating miniaturized, highly complex 2D structures. However, printing technologies offer a significantly wider range of materials, as various polymers, hydrogels and metal composites can be formulated into inks to be printed onto various substrates, thus enabling a wide range of applications that were previously extremely difficult or impossible. In addition, direct printing needs to transfer delicate structures, resulting in higher fabrication throughput, simplicity, and lower costs. The deposition of soft, conformal, and even stretchable inks onto elastic substrates using direct printing is also different from traditional microfabrication that uses rigid, non-stretchable thin films. These wavy structures can undergo larger strain and offer more robust mechanical and electrical properties if combined structural stretchability and intrinsic material stretchability within one component. Similar to traditional tortuous 2D structures, the mechanical behaviour of the resulting structures depends upon several factors such as the mechanical and geometrical properties of the materials. Common for printing technologies, the deposited ink can form structures with elastic modulus several orders of magnitude smaller than the substrate, thus showing a different mechanical behaviour compared to the nonelastic thin films. Furthermore, due to the nature of the direct printing approach, an innovative fabrication strategy is needed to allow lift-off the structure from the substrate for freestanding out-of-plane buckling. In general, wavy 2D structures can be classified into 4 different types: Fully bonded stiff 2D structures, fully bonded soft 2D structures, selectively bonded stiff 2D structures, and selectively bonded soft 2D structures, which are discussed separately below [1].

#### **2.1.4.3 Fully Bonded, Stiff 2D Structures**

The bonded, stiff 2D structures involves the materials that has Young's moduli that are significantly higher than their substrate while keeping contact with the substrate during deformations. These common rigid materials have Young's modulus ranging from GPa to TPa, significantly higher than elastic substrates that usually have modulus in the KPa to MPa domain

[25]. The printing or deposition of such material is mostly done via transfer printing, 3D printing, and ink-jet printing. When the entire device is stretched, the printed stiff structures are able to resist the tensile stress from the substrate and distribute the majority of the strain to the surrounding substrate.

#### **2.1.4.4 Fully Bonded, Soft 2D Structures**

In this category, structures are composed of materials that have same range of Young's modulus to the substrate, and are completely bonded onto the substrate, and thus can be easily stretched, bent and twisted with the substrate. This approach can only be used in combination with intrinsically stretchable inks, as the printed soft composite bonded to the substrate experiences a similar level of tensile strain when the substrate is stretched. Compared to the rigid materials, the soft ones can only distribute small part of the strain in the supporting substrate, which depends on Young's modulus and thickness of the whole structure including material and substrate. The thicker and stiffer the deposited materials, and the thinner and softer the substrate, the less intrinsic stretching deformation the structure will tolerate. As the printed structure bonds tightly with the substrate, its durability against shear stress is generally better than their freestanding counterparts due to the protection from the substrate. In addition, the device is more mechanically resilient with high deformations, as the intrinsically stretchable soft materials can remarkably reduce the fatigue during repeated stretch and release process [26].

#### **2.1.4.5 Selectively Bonded Rigid 2D Structures**

Selectively bonded structures are structures that are partially self-supporting and unbonded to the substrates. When the printed structure bonds to the substrate only at selective locations, allowing the remaining regions of the structure, which are unbonded from the substrate, to be deformed freely. During stretching, the unbonded domain of a wavy 2D design usually converts its strain via out-of-plane buckling in addition to the in-plane rotations, hence allowing the compressed geometric length to release with the growing physical length to its full extent, and achieving more stretchability compared to the fully bonded devices using the 2D design. The printing fabrication of the structures in this category has not been reported, with the majority of them relying on an additional transfer-printing step to achieve selective bonding. Printed-then-transferred tortuous 2D structures show minor conductivity change while exhibiting high level of stretchability [27], [28], [29]. This method like photolithographic or laser-ablation counterparts is considered less advantageous compared to the direct planar printing methods.

### 2.1.4.6 Selectively Bonded, Soft 2D Structures

A combination of the soft, stretchable material, selective bonding strategy, and well-designed 2D structures, is considered most effective among all types of printed wavy 2D structures. Such structures combine the intrinsic material stretchability with the structural stretchability of the design, thus obtaining “two degrees of stretchability. During stretching, the selectively bonded wavy structures initially buckle out-of-plane to release its compressed geometric length. Since no elongation happens at this stage, the conductivity of the buckling structure can remain mostly unchanged. After reaching the buckling critical point, the structure can be further stretched without structural failure. Such intrinsic stretching depends mostly on the material properties and is described as the “2nd degree of stretching.” The 1st degree of stretchability, like the previously described rigid wavy structures, is mainly determined by the geometric design of the structure and thus differentiates itself from the 2nd degree of stretchability, which resembles the stretchability of the soft, bonded tortuous printed structures. The main point in this category is to find a fabrication technique offering selective bonding. Development of a printable sacrificial layer that resembles the photoresist layer used in photolithography etching processes [30]. During printing, a thin layer sacrificial ink is first printed onto the substrate which defines the unbonded areas, followed by printing the main tortuous 2D structure. After curing, the sacrificial layer is dissolved from the substrate, leaving those regions unbonded to the substrate. Using this approach, the direct printing of selectively bonded wavy structures can be achieved without the need for any transfer or cutting steps, hence greatly reducing the fabrication complexity. Fig. 2.1 depicts a schematic of two different bonding strategies.

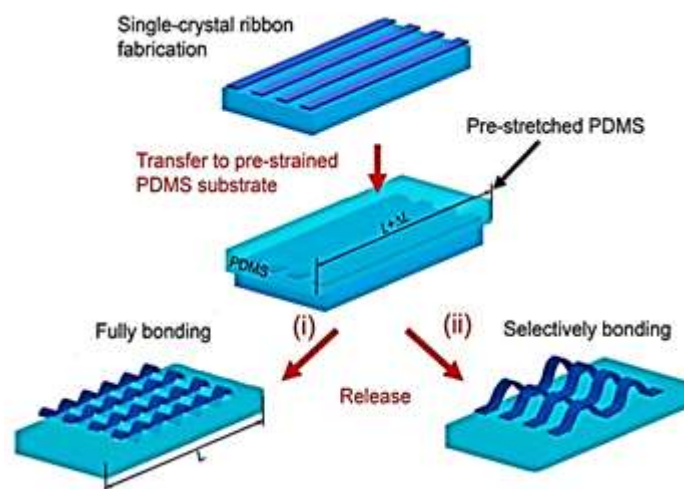


Fig. 2.1 Schematic illustration of two different bonding strategies on the elastomeric PDMS substrate for wavy structures, that are fully and selectively bonded onto the substrate [20]

#### **2.1.4.7 Island-Bridge Structure**

The “island-bridge” structure describes the combination of bulky and non-stretchable devices and stretchable interconnects. The structure emphasizes on accommodating the traditional bulky non-stretchable elements onto the non-stretchable island regions, while localizing the strain to the peripheral stretchable interconnects featuring structurally stretchable tortuous, and buckling-enabled designs, hence achieve stretchability. Numerous studies reported stretchable sensors and circuits non-stretchable elements such as transistors, electrodes, or integrated circuit chips based on the “island-bridge” structure [5]. In these applications, the interconnecting “bridges” contribute directly to the device stretchability, allowing the rigid, bonded functional “islands” to deliver normal performance during deformations. However, the fabrication of these attractive structures requires high accuracy which affect the fabrication cost and throughput. The device stretchability is limited by the bridge stretchability, the bridge/island ratio, as well as the stability of the islands against tensile and shear stresses. Therefore, the shape design of the bridges and the islands, the compatibility between inks, and the bonding between ink and the substrate must be taken into careful consideration. In addition, strain localization strategy requires the island region to experience as little shape change as possible, thus requiring a combination of various inks to form strong, rigid islands to resist any deformation, with soft, resilient bridges to accommodate for the shape change. By addressing the above considerations via careful materials selection and process engineering, the “island-bridge” structure can be successfully implemented in printing technologies [31]. Fig. 2.2 shows a schematic of island -bridge mechanical structure.

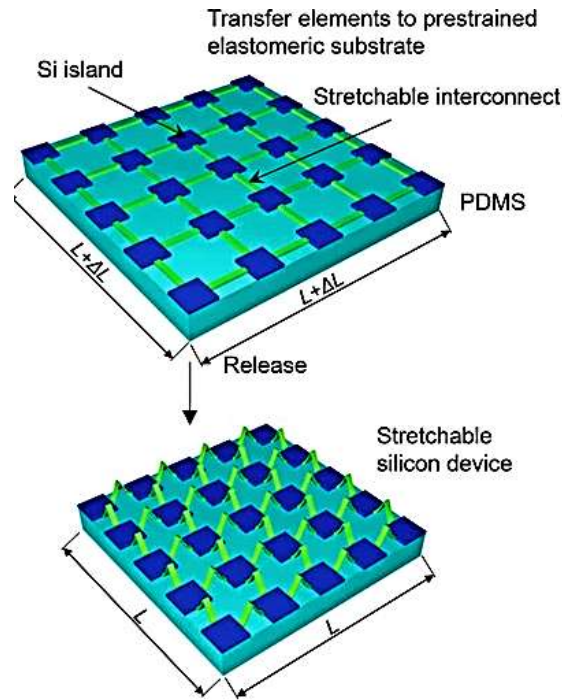


Fig. 2.2 Schematic illustration of the mechanics model of the device island mesh with arc-shaped design [20].

#### 2.1.4.8 Transforming Beyond 2D

From the transformation from 1D linear interconnects to a wavy design that occupies a 2D plane, and from the transformation from fully bonded 2D designs to selectively bonded structures buckling into the 3D space, printed complex structures offer abilities to release the compressed designs in 2D into 3D to enhance the stretchability. Such structural innovations have the potential to offer additional functionalities other than stretchability. Through the introduction of multiple fabrication strategies in direct 2D printing technologies, additional processes can be offered to prepare more complex structures that fully exploit the 3D space. Several recent studies have reported on the use of 2D printing techniques to fabricate 3D structures through the combination of selective bonding, and controlled buckling, which greatly improved the functionality of these structures beyond stretchability. The strategies and challenges of fabricating 3D structures using planar 2D precursors are shortly discussed below.

#### 2.1.4.9 Buckling From 2D to 3D

The development of assembly techniques for 3D structures is witnessing increasing attention, due to the broad implication across a wide range of engineering applications, from microelectromechanical systems (MEMS) and robots [32], [33] and to biomedical devices [34], [35] and metamaterial [36]-[38]. Fully compatible with well-established planar manufacturing

technologies, the 3D assembly techniques are mostly applicable to a broad selection of high-performance materials, including electronic or optoelectronic materials, as well as a wide range of length scales (from several tens of nano-meters to milli-meters). Depending on the different deformation characteristic, the 3D fabrication techniques can be divided into four main categories: rolling [39]-[41] , folding [42], [43], curving [44]-[46] and buckling [47]-[49]. Compared to the first three approaches, the buckling-guided approaches offer access to a diverse range of 3D shapes. Based on this technique the 3D assemblies start first from designing 2D precursor structures which make it easier to achieve much more complex deformations during the assembly process [50], [51]. In particular, the buckling-guided approaches usually rely on a pre-stretched elastomer substrate to serve as the assembly platform, where the 2D precursor structures are imbedded, with strong covalent bonding produced at selective locations. Release of the pre-stretch in this assembly platform provides compressive forces and results in the 2D-to-3D transformation of the precursor structures, through rotation and out of plane buckling deformations. To achieve non-uniform 3D structures, engineered elastomer substrates with either spatial variation of thickness or modulus were introduced that can offer desired strain distributions [52]. Fig. 2.3 summarizes the main strategies of mechanically guided structural designs in stretchable electronics. A series of studies following this concept demonstrated the use of control of pre-stretching of the elastomeric substrate and its selective bonding to form 2D thin films that can easily buckle into various complex 3D structures, such as coils, waves, helixes, tables, flowers, and boxes. The compressive force from the relaxing pre-stretched substrate transferred onto the bonded location of the planar structure as shear forces, which is lead to the upward buckling that results in the pop-up of the desired 3D structures. While still relying on costly, complex fabrication techniques, this work leverages the combination of multiple strategies applicable in 2D printing processes [33].

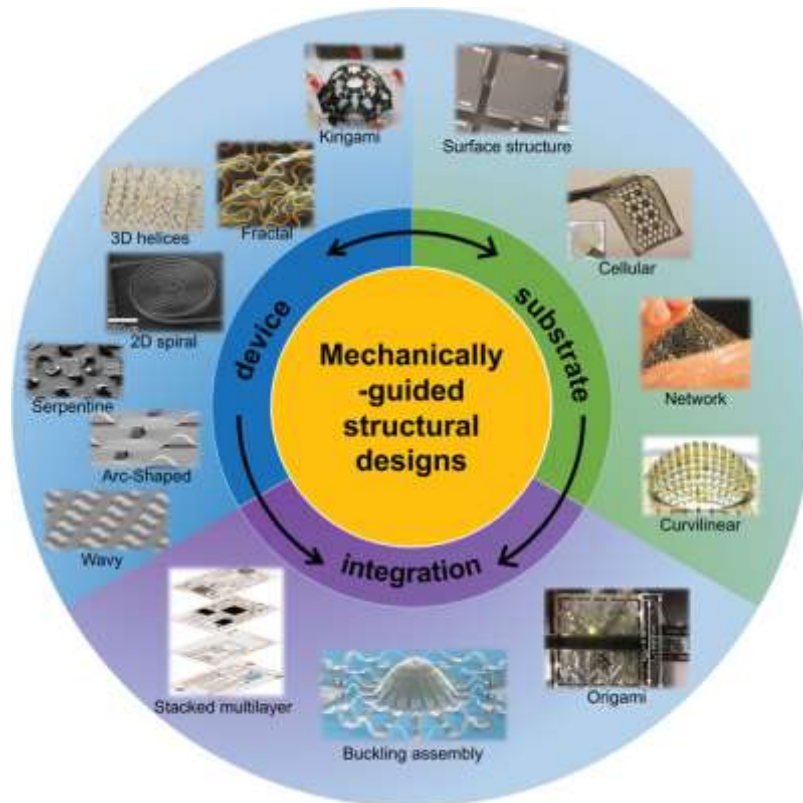


Fig. 2.3 Strategies of mechanically guided structural designs in stretchable electronics. Structural designs of devices and systems, including wavy designs, island-bridge designs (e.g., arc-shaped, serpentine, 2D spiral, 3D helical), fractal-inspired designs and kirigami strategy [20].

The successful transformation of this concept from photolithographic fabrication to screen printing was first presented in [53]. The author of this paper not only combined substrate engineering, selective bonding, and strain localization strategies, but also introduced the concept of programmed buckling. For this purpose, the sacrificial layer and multiple layers of soft polymer composite inks were printed onto a pre-stretched substrate. Upon dissolving the sacrificial layer and releasing the strain from the substrate, the printed composites were able to buckle into 3D structures. The shape of the 3D structures was “programmed” into the 2D stencil printed designs by the accurate control of the deposition thickness and the appropriate selection of ink composites. Screen printing, as a thick-film technology, uses viscous polymer and composite inks to deposit films with thickness up to several hundreds of microns. By depositing multiple layers of inks, the printed 2D structure was partitioned into thicker and thinner regions, where the thinner regions were more likely to deform when applying buckling stress, as predicted by finite element analysis (FEA). The thicker regions, referred to as the “guiding layer,” acting similar to the supporting layer that localizes the strain, define the area where buckling is to be avoided, and direct the strain to the thinner regions, where the majority of the buckling occurred. Coupling these segmented 2D prints with different levels of pre-stretching on the substrate enabled the fabrication of various 3D structures, including coils, triangular

waves, square waves, tables, and pyramids, via programmed buckling. The selection of material is also important when using such strategy, as the localized buckling results in high local tensile stress, which may lead to structural failure if the stress surpasses the ultimate capacity of the structure. In this work, a stretchable elastomer composite ink was used, which allowed the reversible transformation between the 2D and 3D structure without fatigue, as well as stretching deformations without structural failure. Using printing, various functional material, can be deposited onto the guiding layer, which can serve its unique functionality upon transforming into the programmed 3D structure. Upon re-stretching and releasing the substrate, the tensile or compressive stress from the substrate can be effectively transferred to the printed structures as a shear stress on the bonding sites which allow the printed structures to reversibly go flat and pop-up into the reprogrammed shape [1].

The programmable buckling strategy allows a wide range of structures that can reversibly change between the 2D and 3D spaces. Adjusting several parameters, including the magnitude and direction of the pre-stretching, the patterns and thickness of the deposited layers, the location of bonding sites, and the mechanical properties of the deposited elastomers, led to numerous 3D structures, such as helices, boxes, tables, and grippers. The programmed shape change is directly caused by the compressive force as the result of the two competing forces between the compressive pre-stretched layer and the opposing rigid, non-stretched layer. Overall, the combination of multiple fabrication strategies with programmed buckling allows the printing of diverse complex 3D structures via mechanically buckled 2D planar shapes. When coupled with highly scalable printing techniques, which are compatible with a wide range of materials, such strategies become a competitive alternative to complex photolithographic methods and 3D printing technologies.

There exists a considerable body of literature on compressive buckling technique. For example in [24] authors have reported the use of releasable, multi-layered 2D precursors to enable the assembly of different classes of 3D structures, These structures can be coupled with deterministic, substrate-induced buckling processes, open access to a wide range of 3D structures, all starting with 2D precursors that can be formed using the most sophisticated materials and methods in existing microsystems technologies. A mechanically tunable spiral NFC device provides an application example, where the 3D multilayer geometry enhances the  $Q$  factor and broadens the working angle during wireless communication with a primary coil. Other study in [54] reports the design, fabrication, and modelling of LIG-based, soft,

electrothermal actuators, and explore their applications in mechanically guided 3D assembly and human–soft actuators interaction. The actuators consist of the PI, LIG, and polydimethylsiloxane (PDMS) tri-layer. LIG serves as a pliable heater to introduce temperature differences via joule heating. The stress caused by the significant thermal expansion difference between PI and PDMS can deform strategically designed 2D precursors into programmed 3D architectures via global folding and/or local bending in a reversible manner. Recent study in [55] explored the use of 2D materials in functional, 3D systems formed via geometry transformation guided by compressive buckling, with a focus examples in constructs that provide 3D photodetection/imaging capabilities by use of light sensing elements that incorporate monolayer MoS<sub>2</sub> and graphene, each of which offers an extraordinary combination of electrical, mechanical and optical properties. Another research group in [56] analysed the mechanically assembled 3D spiral structures with applications as tunable inductors. The 3D spiral-shaped structure is constructed from 3D transformation a bilayer precursor that consists of a supporting ribbon and a 2D coil on its top. An interesting application for this technique has been reported in [57] which is a strain sensor that offers visible readout and large detectable strain range through a collection of mechanically triggered electrical switches and LEDs. The 2D precursor structure (Cu; 6 μm) consists of two identical spiral ribbons (each with two half-circles of different radii) separated from one another. Uniaxially stretching the substrate leads to tensile buckling processes that transform the spiral ribbons into 3D configurations. The two separate structures approach one another. As the applied strain reaches a critical value, the two ribbons begin to contact, thereby turning the LED on. There has been numerous studies to investigate the theory of the compressive buckling technique or they have investigated new possible designs [58]-[60]. For example, in [48] an analytic model of compressive buckling is presented in the framework of energetic approach, taking into account the contributions of spatial bending deformations and twisting deformations and three different frame geometries are studied, including ‘+’, ‘T’ and ‘H’ shaped designs. A series of recent studies has theoretically investigated the structures that can be reshaped between different geometries as well as those that can morph into three or more distinct states. The approaches rely on elastomer platforms deformed in different time sequences to elastically alter the 3D geometries of supported structures via nonlinear mechanical buckling [61].

The main focus of this document will be on stretchable antennas and different fabrication methods that have been studied in the last decade.

Table 2.1 summarizes the advantages and limitations of the main techniques that have been applied to enable stretchability in electronics.

Table 2.1 Comparison of the current stretchability methods.

		<b>Advantages</b>	<b>Limitations</b>
<b>Material Innovation</b>	<b><u>Hydrogel</u></b> <b>[23], [25]</b>	Super stretchability Biocompatibility Self-healing Stimuli-responsibility	Environmental Instability Expensive Difficult to handling. Non-adherent.
	<b><u>Liquid Metal</u></b> <b>[24], [25]</b>	High electrical conductivity Mechanical stability Self-healing	Corrosive Complexity Non-stimuli-responsibility
	<b><u>Nanomaterial</u></b> <b>[39], [41]</b>	Cost-effective Good mechanical compliance	Trade-off between stretchability and conductivity Weak interfacial bonding
	<b><u>Conductive Polymers</u></b> <b>[43]</b>	Chemical stability Biocompatibility Cost-effective Commercial availability	Low conductivity Prone to crack
<b>Structural Design</b>	<b><u>Origami/Kirigami</u></b> <b>[18], [19], [34], [42]</b>	No need for elastomeric substrate 3D structure	Challenging for small scales and different materials
	<b><u>Textile Embedding</u></b> <b>[20]</b>	Natural stretchability Comfortable Washable	Non-directional permeation of ink Wicking properties of fiber
	<b><u>Planar Buckling</u></b> <b>[58]-[60]</b>	High stretchability Cost-effective All materials/All scales Straightforward fabrication	Spacious when in compressed state

## 2.2 Stretchable Strain Sensors

Capacitive, resistive, piezoelectric, triboelectric, and optical strain sensors are the well-known stretchable strain sensors. Among them, piezoelectric and triboelectric strain sensors usually work at high frequencies and have difficulty in capturing the static strain because of the rapid charge transfer. Thus, they face limitation when using in multiscale and wearable strain sensing applications.

The resistive strain sensors based on metal sheets were initially proposed in the early 1940s and have been utilized for detecting strains up to 5%, such as small deformations in composites and rigid bodies [62], [63]. Currently, the demand for wearable electronic devices has changed the structure of resistive-type strain sensors from rigid to stretchable type. Stretchable strain sensors are typically consisted of active sensing elements combined with stretchable supports [62]. The active materials are usually in the forms of conducting micro-/nanomaterials–polymers composites, thin films, or conductive yarns/fabrics. In fact, the conductive platform of active materials serves as a resistor under an applied voltage. When stretched/compressed, the electrical resistance of the conductive platform changes as a function of the applied strain.

Wearable capacitive-type strain sensors are often fabricated by sandwiching an insulating film known as a dielectric layer between two stretchable electrodes. The capacitance of strain sensors, which is independent of the resistance value of the electrodes, increases under stretching due to the dimensional changes in the capacitive area. Wearable optical strain sensors usually consist of a stretchable waveguide with a core-cladding structure flanked by light emitter and photodetector. The sensing mechanism is based on the changes in the transmission of strain sensors upon deformation measured by the generated light power difference between the light source and photodetector. As aforementioned, other types of stretchable strain sensors have also been introduced in the past decade. Piezoelectric and triboelectric strain sensors are the two main types of stretchable strain sensors [64], [65]. Several limitations associated with the design, embedding, and safety of wearable and stretchable strain sensors exist. Capability of measuring multi-directional strain, complicated calibration process, Sensitivity of the output signal to environmental conditions such as temperature, biocompatibility and the capability of integrating strain sensor and flexible wireless communication systems are the main challenges. Fig. 2.4 shows a wearable strain sensor for joint motion detection.



Fig. 2.4 Wearable and stretchable strain sensor [62].

## 2.3 Stretchable Antennas

Significant advances in multidisciplinary areas including electrical and mechanical engineering as well as material science form the foundations of soft electronic platforms that have unique application in wireless sensing and monitoring. Serving as an interface between radio waves propagating through space and electric currents moving in metal conductors, the antenna is an essential link between such devices and external systems for control, power delivery, data processing and communication [66], [67]. Applications typically demands a set of considerations in performance, size, and stretchability. Some of the most effective strategies rely on intrinsically flexible materials such as liquid metals, nanowires, and woven textiles or on configured 2D/3D structures such as serpentine and helical coils of conventional materials. Examples range from dipole, monopole, and patch antennas for far-field RF operation, to magnetic loop antennas for near-field communication (NFC), where the key parameters include operating frequency,  $Q$  factor, radiation pattern, and reflection coefficient  $S_{11}$  across a range of mechanical deformations and cyclic loads [52]. There have been a number of longitudinal studies involving stretchable antennas that have reported in [68], [69].

Flexible antennas are fabricated using various conductive materials and substrates. The substrate is chosen based on their dielectric properties, tolerance to mechanical deformations and endurance in the external environment. The selection of conductive material (based on electrical conductivity) specifies the antenna performance, such as radiation efficiency.

### 2.3.1 Conductive Materials

Conductive materials with sufficient electrical conductivity is essential for ensuring high gain, efficiency, and bandwidth. Additionally, resistance to degradation due to mechanical deformation is another desired feature for the conductive material. Nanoparticle (NP) inks are used for fabricating flexible antennas due to their high electrical conductivity. Silver-nanoparticle ink is preferred over copper nanoparticles due to their low rate of oxide formation. Very few investigations have been observed for flexible antennas based on copper-based nanoparticles. Besides nanoparticles, electro-textile materials, and nonwoven conductive fabrics (NWCFs) are generally used in flexible antennas. Various types of textile and non-textile conductive materials for developing flexible antennas have been reviewed in [70]-[72]. Adhesive copper, copper tapes and copper cladding also have been reported in the development of flexible antennas.

With combined electronic properties of conductors and mechanical and processing attributes of polymers, conductive polymers (CPs) have been investigated extensively for different electronic applications. Conductive polymers including PEDOT:PSS, PANi, polypyrrole (PPy), poly(3-hexylthiophene) (P3HT), polyacetylene (PA), polythiophene (PTh) seem to be promising materials for flexible and wearable antennas. The low conductivity of conductive polymers was improved by adding carbon nanotubes, graphene, and carbon nanoparticles. Flexible antennas using graphene are promising due to their high electrical conductivity and excellent mechanical properties. Graphene paper [73], graphene ink [74], graphene oxide ink [75], and graphene nanoparticle ink [76] have been used in previous studies for fabricating stretchable antennas. key point in this strategy is maintaining interconnected pathways through these nanomaterials to enable highly conductive channels when the substrate is stretched. Despite great progress, the conductivities of such composites are typically lower than those of conventional metals. The other category of stretchable conductors is based on liquid metals patterned into channels of elastomeric materials. This structure can be bent and stretched to levels beyond those possible with conventional electronic materials. These stretchable designs exhibit high stretchability, while maintaining excellent conductivity. Drawbacks are blockage and fragmentation of liquid metal in the channels during stretching, causing oxidation over many cycles of deformation, preventing robust, reliable contacts to electronic components which results in unreliable packaging with leakage. The final category exploits mechanically guided structural designs of conventional metals, which can undergo large deformations without failure [5].

The performance of flexible antennas relies heavily on the fabricated conducting traces with high deformation sustainability while maintaining electrical conductivity.

### **2.3.2 Substrate**

Elastic substrates, which are able to tolerate the applied strain and regulate the strain distribution in circuits, are key components in stretchable electronics. Moreover, the self-healing characteristic of the substrate is the most desirable feature, so the device can recover from failure resulting from large and repetitive deformations. The substrate material used in flexible antennas need to have minimum dielectric loss, low relative permittivity, low coefficient of thermal expansion, and high thermal conductivity. Such a constraint is driven by the need for increased efficiency in different circumstances at the price of larger antenna size. The alternative strategy is the need for large dielectric constant for miniaturized antennas. Three types of substrates are usually used in the fabrication of flexible antennas: thin glass,

metal foils, and plastics or polymer substrates. Though thin glass is bendable, the intrinsic brittle property restricts its applicability. Metal foils can sustain high temperatures and provide inorganic materials to be deposited on it, but the surface roughness and high cost of the materials limit its applications. Plastic or polymer materials are the best candidates for flexible antenna applications which include: (1) the thermoplastic semi-crystalline polymers: polyethylene terephthalate (PET) and polyethylene naphthalate (PEN), (2) the thermoplastic non-crystalline polymers: polycarbonate (PC) and polyethersulphone (PES), and (3) high-glass transition temperature ( $T_g$ ) materials: polyimide (PI) [77], [78]. These polymers are popular and attractive in recent years for flexible electronics due to their robustness, flexibility, wettability, and stretchability. Due to high  $T_g$ . Polyimide is one of the most preferred materials for flexible antennas, which had been used as a substrate in previous studies [79]-[83]. PET and PEN are preferred in many flexible antenna designs due to excellent electrical, mechanical, and humidity resistant properties. For fabricating different types of flexible antennas, PET has been used due to its excellent conformal behaviour and mechanical stability. For example, [80] reported the design and performance of a bowtie shaped slot antenna on a flexible and low-cost polyethylene terephthalate (PET). The proposed antenna operates over 2.1– 4.35 GHz frequency range (69.77% fractional bandwidth) and exhibits omnidirectional radiation pattern with a peak gain of 6.3 dBi at 4.35 GHz which makes the design suitable for Internet of Things (IoT) applications. In an earlier report [85], a millimetre-wave (mm-wave) inkjet-printed flexible antenna designed on Polyethylene Terephthalate (PET) substrate for the 5<sup>th</sup> generation (5G) wireless applications. PET and PEN substrate have excellent conformality, but low glass transition temperature limits their application for the high-temperature condition. Stretchable antennas made for wearable purposes need unique attributes such as limited visibility for the user, robust antenna performance in different conditions, mechanical stability, and withstanding rigor, such as washing [86]. Different types of substrates used in wearable antennas have been reported in [87]. Silk, and electro textile materials are a few examples of substrates that have been used for wearable/flexible antennas. The use of polydimethylsiloxane (PDMS) polymer as a substrate has been emerging because of its low Young's modulus (<3 MPa) suggesting high conformality. chemical properties, good thermal stability, transparency, and biological compatibility [88].

Paper substrate has been preferred for flexible antennas due to the cost-effective nature and simplicity of manufacturing. A flexible inverted-F antenna on an ultra-low-cost paper-based organic substrate for wireless local area network (WLAN) and flexible display application has been reported in [89]. In [90] flexible antenna with low resistivity for radio-frequency

identification device (RFID) tags on paper substrates via inkjet printing combined with surface modification and electroless deposition (ELD) is demonstrated.

Liquid crystal polymer (LCP) is a flexible-printed-circuit like thin-film substrate and is considered as a good candidate for high-frequency flexible antennas due to low dielectric loss, lower moisture absorption, resistant to chemicals, and can withstand temperatures up to 300<sup>0</sup>C [87]. A metamaterial loaded circularly polarized (CP) flexible CPW fed antenna which is etched on an LCP material for WLAN and WiMAX applications [88], and an inkjet-printed broadband antenna on a flexible, low cost liquid crystal polymer (LCP) substrate for the UHF radio frequency identification (RFID) and sensing applications is proposed in [93].

It can be concluded that the substrate plays an important role in achieving the flexible antennas. Due to their conformal behaviour and suitability, flexible materials have attracted great interest. These flexible materials need to be chosen carefully to withstand the physical deformation conditions such as bending, twisting and stretching while maintaining their functionality. Flexible antennas require low-loss dielectric materials as their substrate and highly conductive materials as conductors for efficient electromagnetic radiation reception/transmission. The recent flexible substrates being introduced for wearable/flexible antennas are Kapton, PET, PDMS, paper, liquid crystal polymer, different fabrics, and paper due to their unique physical, electrical, and mechanical properties.

### **2.3.3 Fabrication Techniques for Stretchable Antennas**

The performance of a flexible antenna is determined by the fabrication method which highly dependent on the utilized substrate. The common fabrication techniques include wet-etching, inkjet printing, screen printing, and other special methods for fabricating stretchable antennas. So far all reported stretchable antenna have been fabricated using intrinsically stretchable materials and mostly planar. The reported non-planar stretchable antennas have been fabricated using photolithography or 3D printing. To the best of the author's knowledge none of them has studied the application of the compressive buckling technique in fabricating stretchable pop-up antenna. According to this technique, antenna fabrication starts with attaching thin metal ribbons on a pre-strained elastomer. Releasing the pre-strain relaxes the elastomer back to its unstrained state, leading to the formation of pop-up antenna that enables stretchability. A number of studies in this area have focused on the mechanical aspect of this technique and to the best of author's knowledge no study has studied the possibility of using compressive buckling fabrication method in antenna design. Therefore, the main focus of this thesis will be on the utilization of compressive buckling technique in designing different stretchable

electronic devices including pop-up antennas, pop-up frequency selective surfaces and pop-up capacitive sensors for strain sensing applications.

## Chapter 3

# Pop-up Antennas and Pop-up Frequency Selective Surfaces

---

### 3.1 Introduction

In this chapter two main electromagnetic devices, pop-up antenna and pop-up FSS structure are introduced, and the entire design procedure is presented in detail. The design and fabrication strategy of all introduced designs in this chapter are based on compressive buckling technique. This chapter includes five published papers. These papers offer practical applications for the designed electromagnetic pop-up devices.

- First paper presents simulation and fabrication of a pop-up antenna for on-skin application. This antenna-based strain sensor can detect skin stretch up to 60% by frequency shift. The design is small, simple to use and cost-effective. The substrate has been chosen to match the mechanical properties of human skin.
- Second paper Introduces a pop-up multiband antenna. The antenna can change its frequency response by mechanical deformation from fully flat state to fully bent state.
- Third paper offers pop-up strain sensors for biaxial strain measurement. This sensor includes a pop-up loop antenna. Different loop antennas are introduced in this paper.
- Forth paper presents a detailed study on pop-up antennas for gas sensing applications. In this paper, combination of pop-up antennas and swelling properties of the elastomeric substrate has led to a novel sensing platform which is able to detect Diethyl ether vapor by frequency shift.
- Fifth paper introduces a pop-up frequency selective surface (FSS). This is a novel structure which allows biaxial strain sensing by changing its shape from 2D to 3D. This is a unique structure as with more stretch it undergoes, more stability in the frequency response is obtained.

## **3.2 Highly Flexible Strain Sensor Based on Pop-up Dipole Antenna for On-Body Applications [94]**

### **3.2.1 Abstract**

Soft electronic systems are intensively desirable due to their similar mechanical properties to human skin. Technological advances in flexible, skin-attachable, strain sensors over the last decade have made them attractive for medical applications, in particular, out-of-the-clinic health monitoring. Here we report a novel highly stretchable strain sensor based on a compressive buckling technique for on-body applications. Our suggested sensor can measure 0 to 60% strain with the frequency shift in the range of almost 2.4 GHz to 5 GHz while keeping the on-skin antenna gain greater than -11 dBi. Finite Element Analysis (FEA) using COMSOL Multiphysics® 5.3a was adopted to analyse the buckling behaviour of the 2D metallic precursor as well as the antenna performance. Numerical results are in good agreement with the experimental data.

**Keywords:** Strain, Compressive, Buckling, Pop-up, FEM.

### **3.2.2 Introduction**

Flexible sensors offer the capability of integrating with the human body. These devices are mountable on different curvilinear surfaces, which makes them ideal candidates to be placed directly onto the skin. Designing an efficient sensor capable of detecting the amount of skin strain as well as providing real time sensing data is of great interest. To date several attempts have been made to integrate antenna design for measuring the amount of strain [95]-[99]. For example changes to the length and width of a patch antenna due to the applied strain in the range of (0%-2%) resulted in a resonant frequency down-shift between 5.8 GHz to 5.7 GHz [95]. Other study has reported an antenna design based on flexible multi-layered graphene film which can detect tensile and compressive bending with strain sensitivity of 9.8 and 9.36, respectively [96]. Strain sensitivity relations can be found in [97]. Researchers in this paper have worked on a rectangular patch antenna on paper substrate with the strain sensitivity of 3.23 and 3.34 to 1.67% of compressive and tensile bending strain, respectively. This project aims to contribute to this growing area of research by incorporating compressive buckling technique to the antenna design. This work is divided in to two steps. At first nonlinear buckling behaviour of a ribbon made of metal under different amounts of strain was studied and then results from the first step were coupled to the radio frequency physics in order to measure the antenna performance.

### 3.2.3 Methods

The proposed strain sensor function is based on the resonant frequency shift of a half wavelength dipole antenna made of 30  $\mu\text{m}$  thick copper. Fig. 3.1 shows the schematic of the dipole and all dimensions parameters are mentioned in Table 3.1. The antenna has been designed to operate at 2.4 GHz without any strain on an ultra-thin, elastomeric Silicone rubber substrate (0.4 mm thickness) with the commercial name of Dragon Skin which has effective elastic modulus ( $E_{\text{Substrate}} = 166 \text{ kPa}$ ) and Poisson ratio ( $\nu_{\text{Substrate}} = 0.49$ ) similar to human skin [6].

Structural mechanics module of COMSOL Multiphysics® software was used to model the antenna deformation with 0% to 60% strain.

Fig. 3.2 illustrates antenna samples for 0 to 60% strain as well as their functions on human forearm.

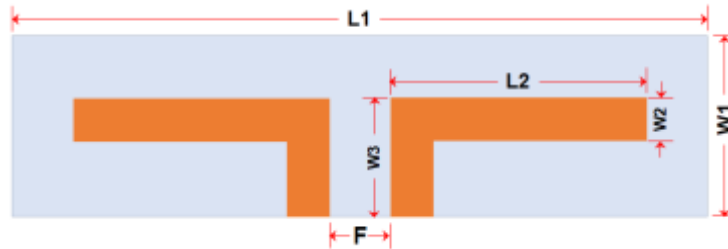


Fig. 3.1 Schematic of half wavelength dipole

Table 3.1 Dimension parameters of the antenna design.

Parameters	L1	L2	W1	W2	W3	F
Dimensions (mm)	40	16	10	1	5.5	2

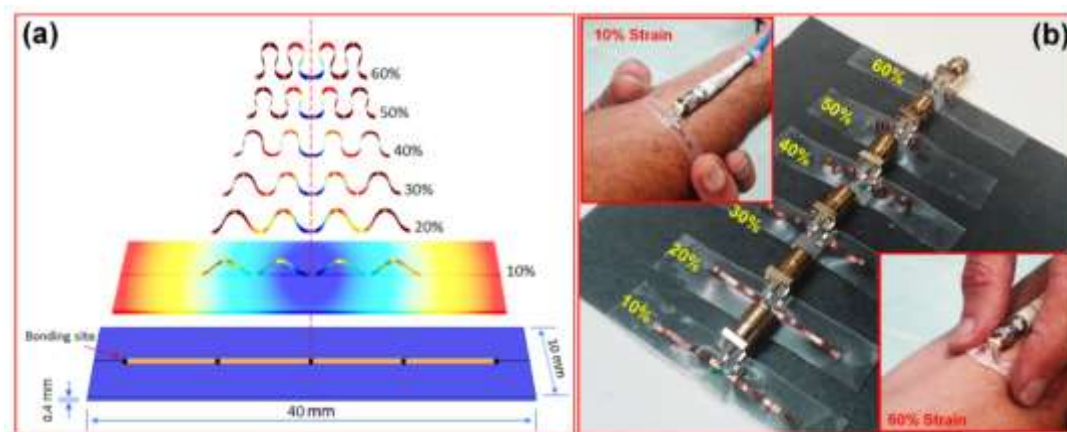


Fig. 3.2 Buckled ribbon with different uniaxial strains on the elastomeric substrate. (a) Simulation. (b) Antenna samples, the antenna was tested on forearm.

Mooney Rivlin model (two parameters) was utilised to model the hyperelastic substrate, which

can fit the measured nonlinear stress-strain curves of isotropic rubber-like materials very well [100].

$$\Psi = \sum_{i=1}^2 C_i(I_i - 3)$$

Where  $\Psi$  is strain energy function,  $I_1$  and  $I_2$  are Cauchy- Green invariants,  $C_1$  and  $C_2$  are Monney Rivilin parameters. After post-buckling analysis, the deformed structure was coupled to the RF module for evaluation of its electromagnetics characteristics as a half wavelength dipole antenna. The antenna was placed on forearm which was modelled with a multi-layered cubic structure with the dimension of 60 mm×60 mm×20 mm consisting of bone, muscle, skin and fat with their specific permittivity and conductivity in the frequency range of interest [7], [100]-[102], as presented in Table 3.2. The electrical properties of the elastomeric substrate were measured as  $1.6 \pm 0.2$  and 0.04 (S/m) for permittivity and conductivity, respectively. The input impedance of antenna is 50  $\Omega$  and perfectly matched layer (PML) boundary condition was used for absorption of outgoing waves. As the accuracy of solution intensively depends on the mesh size, mesh refinement was adopted to minimise the error between the real and approximated solutions.

Table 3.2 Properties of a three-layer model of human body.

<b>Body Layer</b>	<b>Thickness (mm)</b>	<b>Relative Permittivity</b>	<b>Electrical Conductivity (S/m)</b>	<b>Density (Kg/m<sup>3</sup>)</b>
<b>Bone</b>	5	11.4	0.38	1850
<b>Muscle</b>	10	52.8	1.71	1059
<b>Skin &amp; Fat</b>	5	38.1	1.44	1010

### 3.2.4 Results and Discussion

Skin strain due to the human motion causes a tensile stress in the substrate and when the skin returns to its normal condition the substrate is released to its original size. As a result of this stretch and release mechanism, a compressive stress is induced into the dipole antenna with the selective bonding to the substrate and initiates nonlinear buckling process which cause an extension to the third dimension. Fig. 3.3 represents the Von mises stress (MPa) along with both the substrate and the metallic ribbon with 10% and 60% strain, respectively. From the Fig. 3.3 it can be seen that amount of stress close to the bonding sites as well as the bend apexes is much higher than other parts. Due to the out of plane displacement during the buckling, a

mutual capacitance occurs between the dipole adjacent arms which leads to a decrease in the overall capacitance.

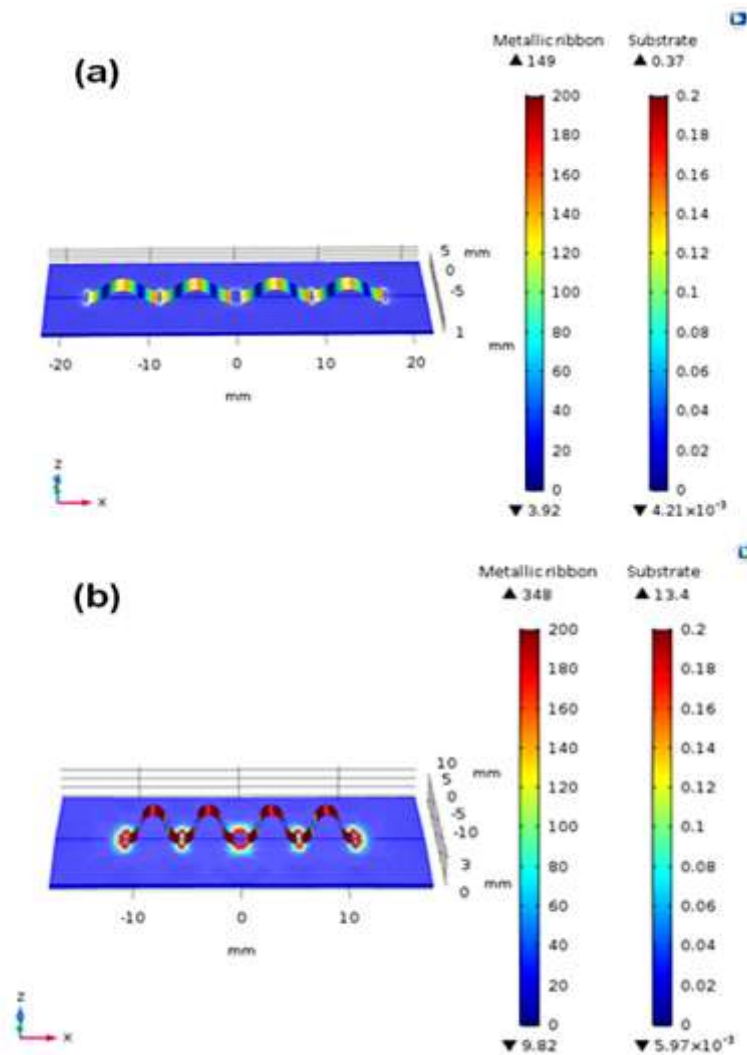


Fig. 3.3 Von mises stress for (a) 10%, and (b) 60% strain.

This factor along with the existence of air gaps between the substrate and the buckled sections will result in a quite large resonant frequency shift. By increasing the strain level, distance between two arms in each meander decreases while the height of each bend becomes greater. As the arms get closer, an increase of the in-series combined mutual capacitance is expected [103]. A decrease in the overall capacitance as well as existence of larger air gap between the dipole and substrate lead to a larger frequency shift. Fig. 3.4 plots reflection coefficient ( $S_{11}$ ) versus frequency both for numerical and experimental data. Numerical data illustrates that when dipole antenna is in flat mode (0% strain) it works at 2.4 GHz and when it goes under the

maximum compressive strain (60%) it works at 5 GHz. Note, the antenna  $S_{11}$  remains better than -20 dB across the entire stretch range.

Experimental measurement represents a maximum frequency tolerance of almost 5% which is due to the fabrication accuracy. Fig. 3.5 presents the frequencies related to the strain values between 0% and 60% which shows a nonlinear behaviour. It suggests that there is a significant frequency up-shift of about 800 MHz from 0% to 10% substrate strain and it reduces further to 500 MHz and 400 MHz for 20% and 30% strain, respectively, and then remains constant at about 300 MHz for further strain percentages.

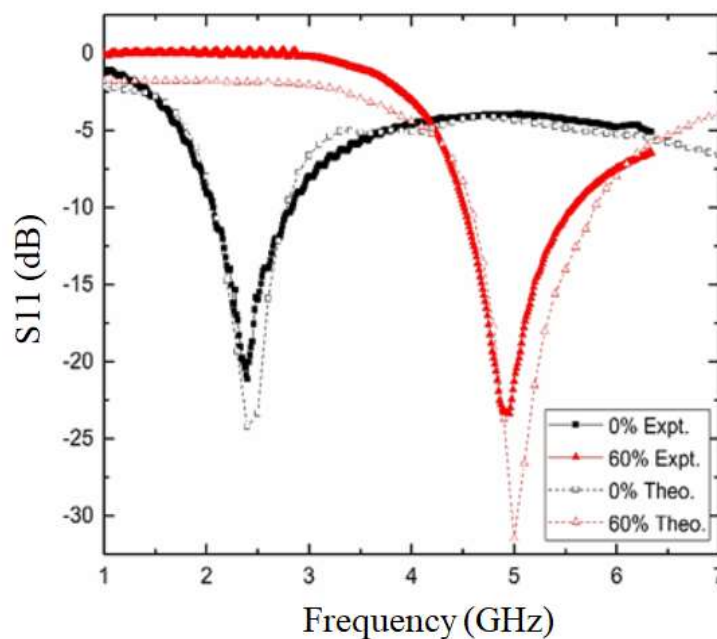


Fig. 3.4 Numerical and experimental reflection coefficient (dB) of half wavelength dipole antenna versus frequency (GHz) with 0% and 60% strain.

Fig. 3.6 shows radiation pattern of the antenna (different planes) with 0% and 60% strain. The antenna has a gain of greater than almost -11 dBi while keeping on skin which is expected due to the loss within human tissues.

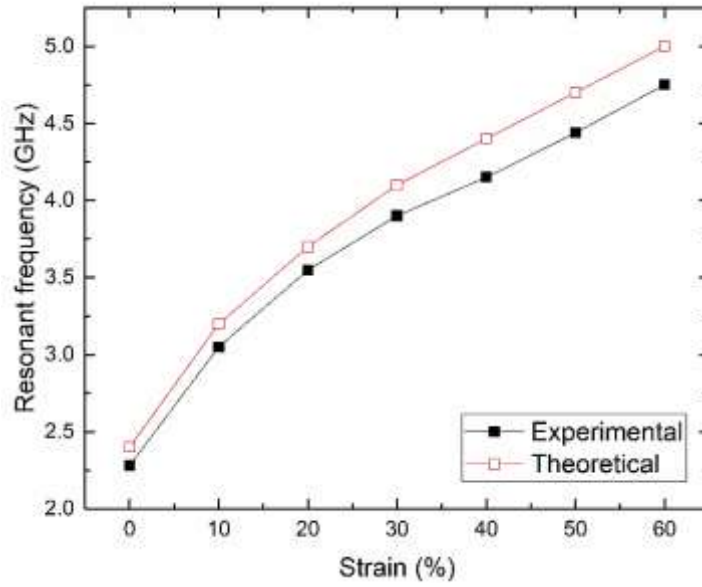


Fig. 3.5 Resonant frequency shift as a function of the applied strain.

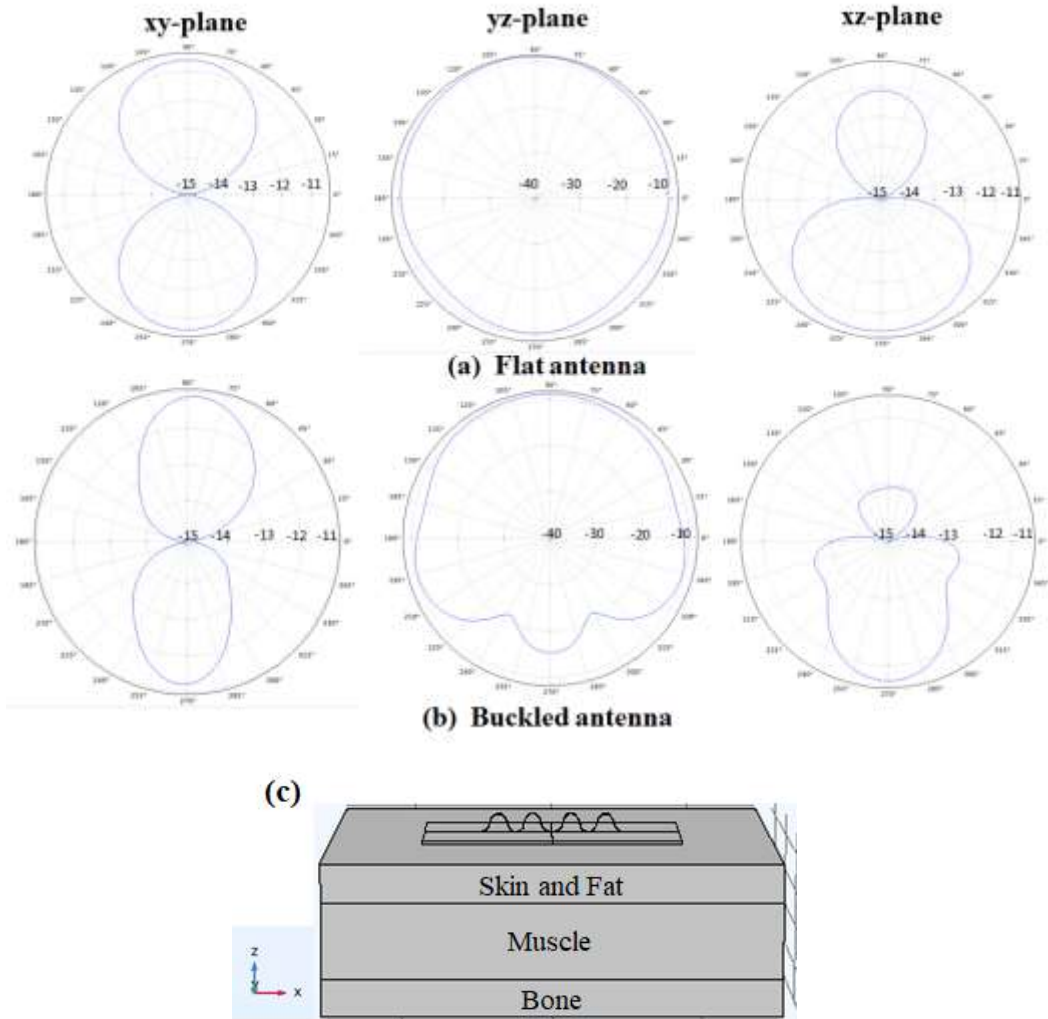


Fig. 3.6 XY-plane, YZ-plane and XZ-plane of far field gain (dBi) for, (a) 60%, and (b) 0 % strain. (c) Orientation of the antenna on the three-layer human body tissues.

### **3.2.5 Summary and conclusion**

This section presented the design, simulation result and fabrication of a novel flexible strain sensor for body mounting applications. This sensor works based on resonant frequency shift of a half wavelength dipole antenna which is deformed according to a compressive buckling technique. The proposed sensor can detect up to 60% strain with significant frequency shift in the range of 2.4 GHz to 5 GHz. The antenna gain is greater than -11 dBi when directly attached to skin for the whole strain range of interest. Antenna samples were tested on body and there was a good match between numerical data and experimental measurements.

## **3.3 A Dual-band Strain Sensor Based on Pop-up Half Wavelength Dipole Antenna [104]**

### **3.3.1 Abstract**

Here we present a pop-up half wavelength dipole antenna with dual band operation for strain sensing applications. The proposed antenna is lightweight, low cost and easy to fabricate with a simple design based on a compressive buckling technique. This flexible strain sensor can measure 0 to 30% uniaxial strain with the frequency shift in the range of 2.45 GHz to 2.9 GHz in the first band and 5.5 GHz to 6.3 GHz in the second band. A prototype of the proposed structure was fabricated and tested. Measured results show a good correlation with the Finite Element Analysis (FEA) simulation.

*Keywords:* strain; pop-up; sensing; buckling; antenna.

### **3.3.2 Introduction**

Stretchable strain sensors have been the subject of considerable research during the last decade and they are expected to significantly contribute to new technologies and be applied in various applications including health monitoring systems, human motion detection, smart cloths, environmental monitoring and so forth [105]. To date different types of antenna have been integrated in strain sensor designs [106], [107]. For example, a strain sensor based on a dual band rectangular microstrip patch antenna is reported in [106]. This sensor can measure 0 degree to 55 degree bending in the antenna by resonant frequency shift in the range of 1.8 GHz to 2.108 GHz for the first operational band and 2.4 GHz to 2.78 GHz for the second band. Other study has reported a circular microstrip patch antenna for strain sensing applications. The sensor can detect 0 to 10% strain by 10% resonant frequency down shift [108]. In [109] a microstrip patch antenna strain sensor has been designed based on the relation between the resonant frequency and the length of the microstrip patch antenna. The suggested sensor measures 0 to 5% strain by 3.6 MHz frequency down shift. Similarly, the strain sensor design reported in [107] is based on a planar dipole antenna and can detect 0 to 5% tensile strain with 28 MHz frequency down shift. This paper introduces a new stretchable strain sensor design based on pop-up half wavelength dipole antenna by using a compressive buckling technique. This technique is a simple and cost-effective fabrication process for transforming 2 dimensional (2D) layouts to 3D [94]. Finite Element Analysis (FEA) method using COMSOL multiphysics® software was applied to perform a two-step simulation [7]. At first a nonlinear buckling analysis was performed for the antenna under different strain levels from 0 to 30% and then the results from the first step were coupled to another RF simulation in order to

evaluate the antenna performance. A good consistency was observed between numerical results and experimental measurements.

### 3.3.3 Antenna design and results

The proposed half wavelength dipole antenna is made of double layer 30 thick copper ribbons that are bonded with each other at selective sites on a  $T = 0.4$  mm thick Silicone rubber substrate (Dragon Skin) with Young's modulus of 166 kPa and Poisson ratio of 0.49. The schematic of the antenna is depicted in Fig. 3.7 and all geometrical dimensions are presented in Table 3.3. The antenna has been designed to work in a single band at 2.45 GHz when flat and the metallic ribbons are electrically connected in each dipole arm. The electrical properties of the elastomeric substrate were measured as 1.6 and 0.04 S/m for permittivity and conductivity, respectively. The input impedance of the antenna is  $50 \Omega$ .

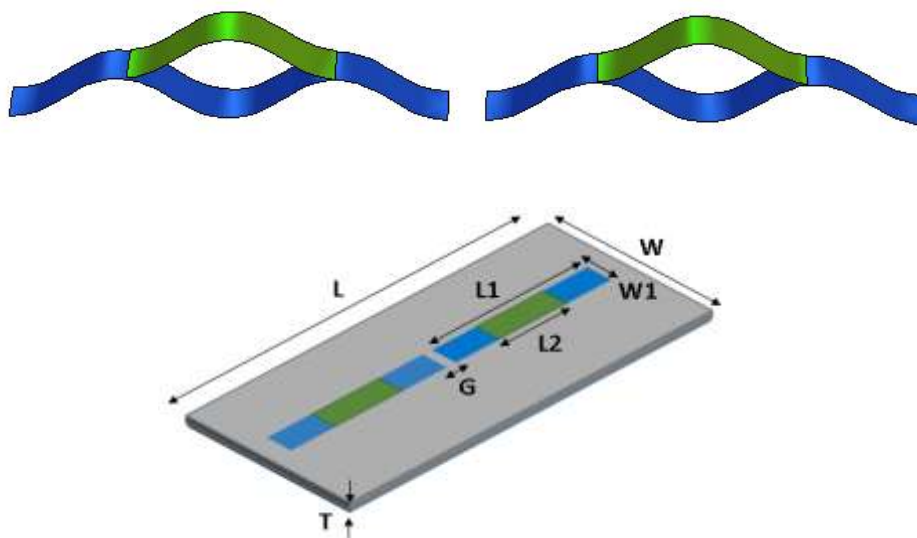


Fig. 3.7 Schematic of the designed dual band half wavelength dipole antenna.

Table 3.3 Dimension parameter of the antenna design.

Parameters	L	L1	L2	W	W1	G
Dimensions (mm)	60	25	12.5	20	3	2

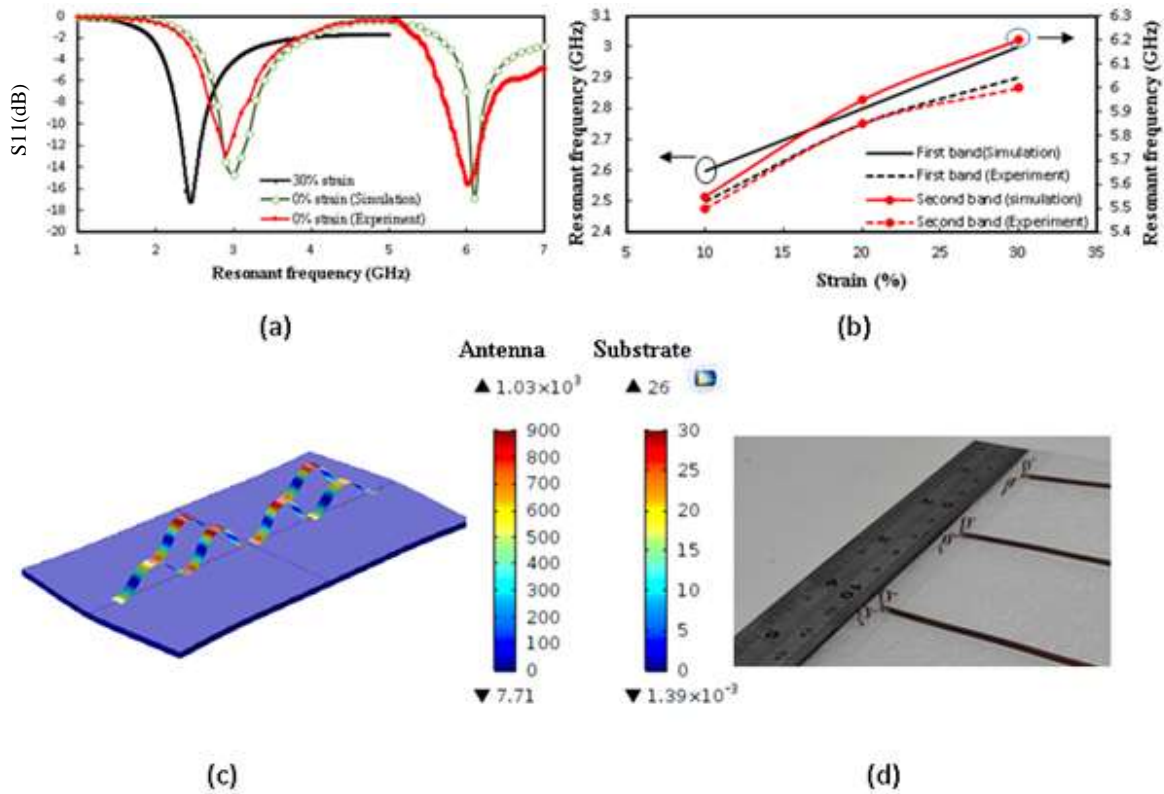


Fig. 3.8 (a) Numerical and experimental reflection coefficients (dB) of the pop-up half wave dipole antenna versus frequency (GHz) for 0% and 30 % strain in the substrate. (b) Frequency shift versus strain. (c) Von Mises (MPa) stress on the antenna and substrate. (d) Antenna prototype for 10%, 20% and 30% strain in the substrate.

perfectly matched layer (PML) boundary condition was applied to prevent spurious reflections from the inside of the computational region. The nearly incompressible hyperelastic substrate used in this sensor design was simulated with Mooney Rivlin model (two parameters) [94]. Uniaxial tensile strain in the elastomeric substrate and its return to the original dimension induce a compressive stress into the dipole antenna which is selectively bonded to the substrate and initiate buckling in the third dimension. This out of plane displacement leads to a decrease in the overall capacitance and consequently an up-shift in the resonant frequency. Moreover, two metallic ribbons in each dipole arm are insulated from each other so, buckling process and as a result capacitive interaction between the two metallic ribbons will lead to another resonant frequency (second band) due to the existence of the upper bonded layer.

Fig.3.8 represents the Von mises stress (MPa) for both the substrate and dipole after returning of the substrate to its main size (30% strain). From this figure it can be seen that the amount of stress close to the bonding zones as well as the bend peaks are much higher than other parts.

### **3.3.4 Summary and conclusion**

In this section a novel highly flexible strain sensor has been reported based on the resonant frequency up-shift of a pop-up half wavelength dipole antenna. The proposed antenna exhibits a dual band operation due to the existence of two insulated. metallic layer in each dipole arm. The suggested sensor is able to measure 0 to 30% strain in the substrate by frequency shift in the range of 2.45 to 2.9 GHz for the first band and 5.5 to 6.3 GHz for the second band. Numerical data and experimental outcomes are in good agreement with each other.

## **3.4 Mechanically Influenced Antennas for Strain Sensing Applications Using Multiphysics Modelling, paper 3 [110]**

### **3.4.1 Abstract**

Here we report highly flexible 3D antennas which leverage nonlinear compressive buckling to tune their operating frequency through 0 to 30% uniaxial or biaxial stretch /release of their elastomeric substrate. The proposed 3D designs are straightforward to fabricate compared to the existing direct 3D fabrication routes which makes them promising for strain sensing applications. By utilizing a soft silicone substrate and structural design of the conventional metallic materials, we have demonstrated two designs of 3D stretchable antennas: "Pop-up convoluted loop antenna" and "Pop-up multilayer dipole antenna". Multiphysics simulation using FEA method is used to analyze the antenna models and the numerical results are in a good correlation with measurements.

*Index Terms:* flexible, compressive buckling, pop-up, multilayer.

### **3.4.2 Introduction**

Non-planar surfaces including biological organs are prevalent in nature. Soft electronics that can effectively adapt to these surfaces significantly improve the applicability of conventional bulky and rigid electronics in sensing and monitoring [111]. Two strategies can be applied to achieve stretchability in electronics, first integrating with novel flexible materials such as conductive textiles, liquid metals, conductive polymers and nanomaterials [112]-[115] or structural design, by making non-flexible structure into specific design that can bear the applied strain without fracturing. Structural design as a powerful approach for bestowing stretchability to materials that are intrinsically rigid have received much attention in the last five years. For instance, in [59] a deformable self-similar interconnect with meander-shaped layout was proposed. This interconnect can respond to the applied strain by rotating in plane or buckling out of plane. Proposed skin-mounted technologies require integrating flexible electronic systems with stretchable antennas, enabled by the efforts with new soft substrates and novel integration approaches with structural designs to provide wireless connectivity. Reconfigurable antennas can dynamically tune their radiation characteristics in order to adapt to the constantly changing operating conditions. As a particular category, stretchable antennas are demanding due to their radiation engineering through stretch and compression. To date different types of stretchable antennas have been proposed [69], [116], [117]. For example, using stretchable conductive ink based on polysiloxane-silver composite in a patch antenna led to 200 MHz

frequency downshift in response to 20% strain [69]. Furthermore, a metamaterial inspired antenna using liquid metal has been presented in [116], which detects 60% strain by 150 MHz frequency up-shift. More recently, [117] proposed a stretchable antenna by embedding silicone based conductive adhesive. This antenna can identify 60% strain via 1 GHz frequency down shift. Although these antenna designs provide good sensing range, the conductive materials face many challenges such as low conductivity under mechanical deformation and delamination.

In this research, we used structural design technique to introduce two novel 3D stretchable antennas for strain sensing applications. These designs present advantage in terms of simplicity of fabrication over the reported designs in the literature, as the current direct 3D fabrication methods are typically constrained by the accessible range of sophisticated 3D geometries and material.

### **3.4.3 Methodology**

The proposed antennas have been designed using the compressive buckling approach. This indirect 3D assembly makes use of well-established planar technologies to transform 2D structures into 3D structures by mechanical deformation. Based on this method, the flat antenna pattern is selectively bonded to a pre-strained elastomeric substrate, so the free sections can bend up after releasing the substrate to absorb the corresponding compressive force.

Both mechanical and electromagnetic simulations were performed via FEA method using COMSOL multi- physics, version 5.3 a [7]. The antennas were fed with 50  $\Omega$  coaxial cable and a perfectly match layer (PML) was used for the radiation boundary condition. The FEA multi-physics simulation steps are as follows:

- 1- Electromagnetic simulation (COMSOL Multi-physics, RF module) models the planar antennas on a 30% stretched elastomeric substrate. Adaptive meshing convergence was used.
- 2- Mechanical simulation (COMOSL structural mechanics module) models the buckled antenna shape after 30% strain release in the substrate via nonlinear buckling.
- 3- Electromagnetic simulation of the mechanically deformed antennas (3D) resulting from step two on the relaxed substrate.

In this section two different pop-up antenna design will be introduced:

### 3.4.4 Pop-up convoluted loop antenna

The proposed flat convoluted loop antenna is made of 30  $\mu\text{m}$  thick copper foil cut by means of Cricut explore air<sup>TM</sup> machine [117] selectively bonded to an 0.5 mm thick elastomeric substrate (Dragon Skin [115]) with Young's modulus of 166 kPa and Poisson ratio of 0.49 [6], as seen in Fig. 3.10. The proposed antenna operates at 2.9 GHz on a 30 % biaxial stretched substrate with dielectric constant of 1.8 and conductivity of 0.04 S/m. The electrical properties of the substrate was measured and averaged in the frequency range of 2.9 GHz to 4 GHz using a SPEAG Dak 3.5 probe with a Rohde and Schwarz ZVL 6 GHz network analyzer using the manufacturer procedure [120]. The schematic of the antenna is illustrated in Fig. 3.9, and all geometrical parameters are presented in Table 3.4.

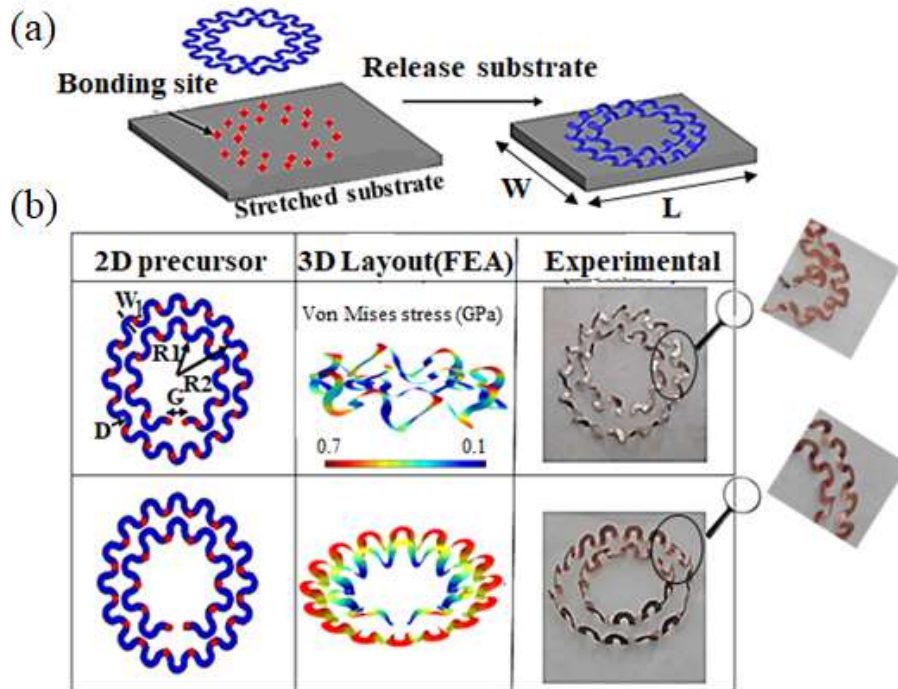


Fig. 3.9 3D assembly of loop precursor. (a) Buckling process. (b) Numerical and experimental studies of two 3D convoluted loop and 3D flower loop antennas with different bonding patterns (red circles), Top: convoluted loop and down: flower-shape loop antennas.

Table 3.4 Parameter for antenna design

Parameter	R <sub>1</sub>	R <sub>2</sub>	D	W <sub>1</sub>	G	L	W
Dimension (mm)	5.8	9.4	2.2	1	4	25	25

By changing the bonding site locations, different 3D configurations can be achieved. Fig. 3.10 shows an alternative possible 3D shape, which is a ‘flower’ loop. However, only the convoluted loop antenna has been studied in this paper. Note that 30% is the maximum strain level leading to a convoluted loop without the neighbouring meander sections touching each other. The simulated  $\lambda$  perimeter loop (larger loop) yields an input impedance of almost  $100 \Omega$  at resonance in flat mode. In order to achieve a match at the design impedance of  $50 \Omega$  and to eliminate any additional matching networks, a secondary internal convoluted loop was included in the structure. This provides the impedance transformation from  $50 \Omega$  source to the main radiating element. The designed pop-up strain sensor can indicate 0 to 30% biaxial strain by downward frequency shift from 3.47 GHz to 2.9 GHz, as illustrated in Fig. 3.10.

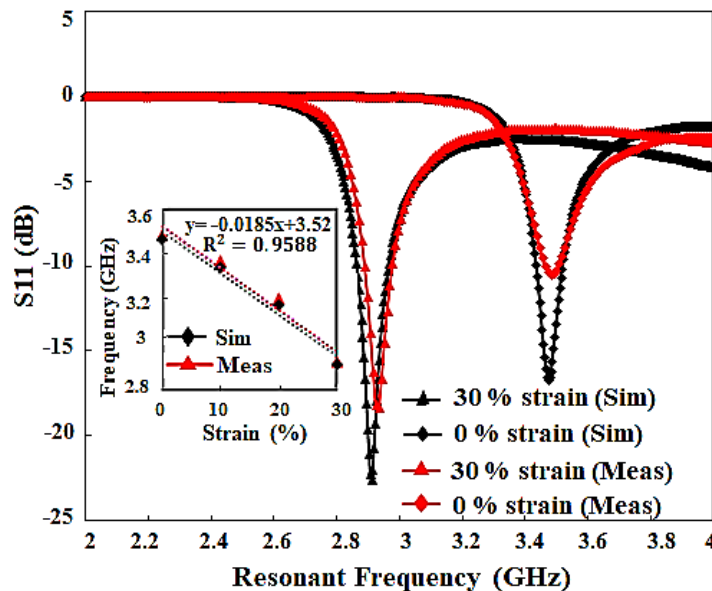


Fig. 3.10 Experimental and numerical results of reflection coefficient (dB) vs resonant frequency (GHz) for flat wavy loop antenna (30% strained substrate) and convoluted loop antenna (relaxed substrate). The sensor can measure up to 30% biaxial strain through 570 MHz downshift. Linear interpolation was used to obtain the sensing pattern.

### 3.4.5 Pop-up multilayer dipole antenna

The design of the second stretchable and reconfigurable 3D multiband antenna includes four coupled metallic ribbons that are bonded with each other at selective sites integrated with a 0.4 mm thick elastomeric substrate with electrical and mechanical properties described in the previous section. All dimensions are presented in Table 3.5. The layers are insulated from each other by means of super glue (Loctite Company) and the antenna fabrication route is illustrated in Fig. 3.11. The designed antenna resonates at 2.4 GHz when flat on a 30% uniaxial stretched substrate. Releasing the strain triggers the out-of-plane buckling of the 2D bonded multilayers,

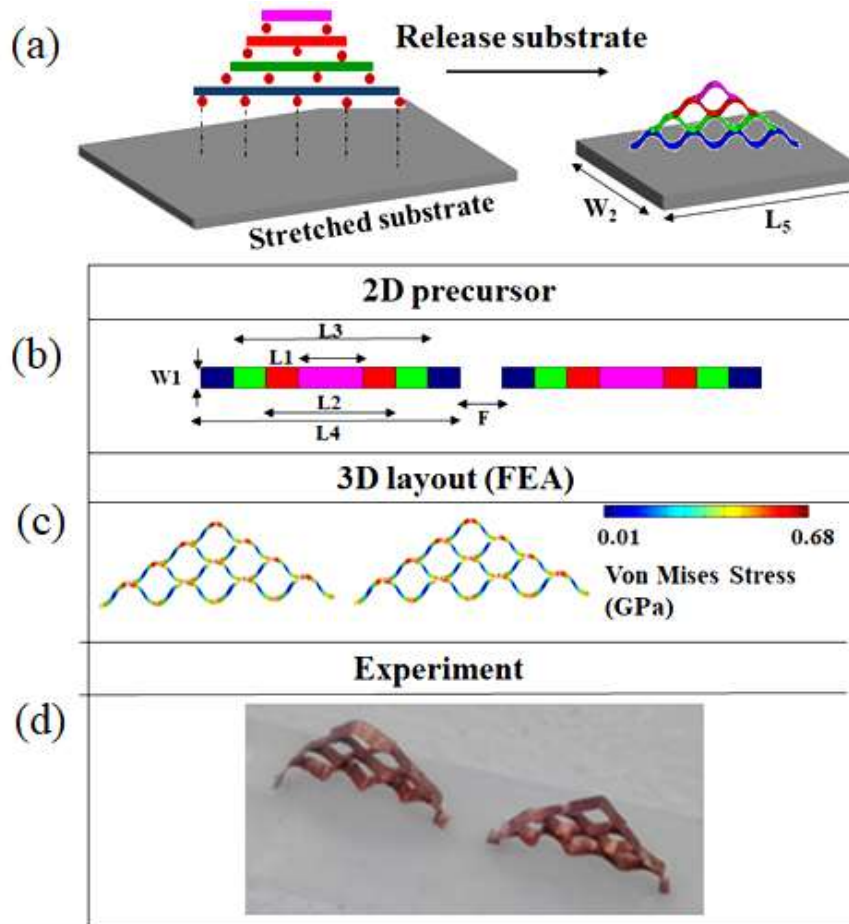


Fig. 3.11 (a) 3D assembly of multi-layer dipole antenna via compressive buckling. (b) Geometrical parameters of the design. (c) Simulation results. (d) A prototype of the design.

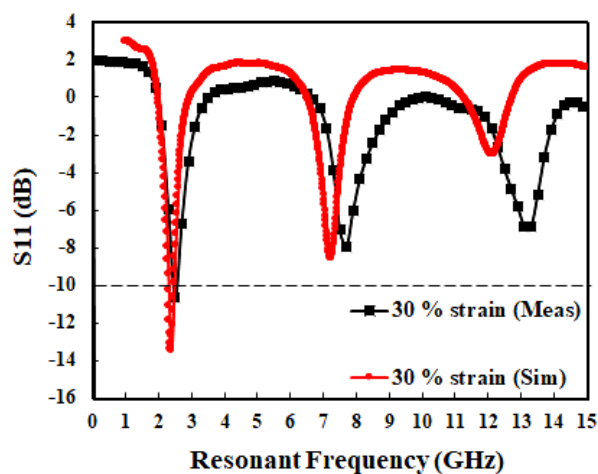
lifting them off each other and the substrate surface at the non-bonded interfaces, and thereby leading to the formation of 3D antenna. Fig. 3.11 shows the multiband feature of the proposed 3D dipole-like antenna before and after 30% strain release in its substrate. Fig. 3.12 (a) shows the reflection coefficient (dB) plot for the proposed antenna when fully stretched and Fig. 3.12 (a) illustrates the reflection coefficient (dB) plot for the multiband antenna when relaxed. While fully stretched, the single matched band is at 2.4 GHz, after buckling, the capacitive interaction between insulated layers led to the emergence of other additional resonant frequencies at 8.5, 12 and 13.5 GHz, as presented in Table 3.6.

Table 3.5 Dimensions of the designed multi-layered antenna.

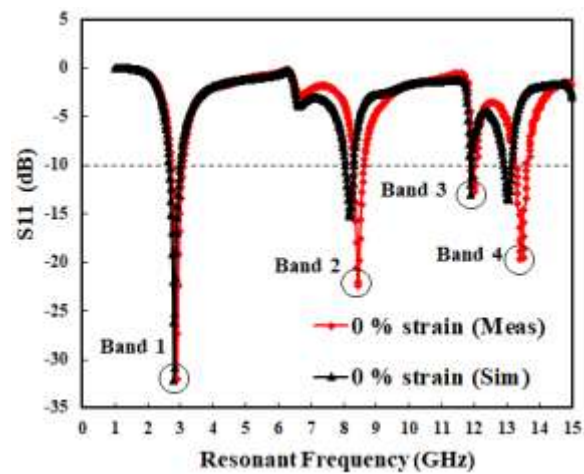
Parameter	$L_1$	$L_2$	$L_3$	$L_4$	F	$L_5$	$W_1$	$W_2$
Dimension (mm)	6.2	12.5	18.7	25	4	60	2	20

Table 3.6 Matched frequency bands, simulated gain and simulated total efficiency of the 3D multi-layered antenna as a function of sensing strain.

Strain (%)	Frequency (GHz)	Gain (dBi)	Total efficiency (%)
30	2.4	1.95	83
20	2.57	1.78	97
	7.05	3.65	84
	9.85	3.45	98
	10.63	4.92	88
10	2.63	1.88	97
	7.79	3.79	98
	10.3	3.49	84
	11.9	5.03	88
0	2.9	1.94	98
	8.45	3.1	98
	12	3.66	84
	13.5	6.22	98



(a)



(b)

Fig. 3.12 Reflection coefficient (dB) as a function of resonant frequency for (a) fully stretched substrate (30% strain) and (b) relaxed substrate (0% strain).

### 3.4.6 Summary and conclusion

Two designs for stretchable and reconfigurable 3D antennas based on mechanically guided assembly have been reported. First design presents a 3D convoluted loop, which can detect up to 30% biaxial strain in its substrate and the second design represents a 3D multi-layered dipole-like antenna, which works at single band while 30% stretched and shows multi-frequency feature after buckling. The proposed sensors show higher response rate ( $\Delta f/\Delta \epsilon, \epsilon$  denotes the strain) in comparison to the designs reported in the literature [69], [116], [117]. This factor along with the simplicity of the fabrication in comparison to the direct 3D fabrication routes, which are expensive, limited in shapes and materials make the both designs of interest for strain sensing applications, such as on-body sensing which will be the future research effort. Combined experimental and computational studies based on multi-physics FEA simulation are in good agreement.

## 3.5 Antenna-Based Pop-up Vapor Sensor Guided by Controlled Compressive Buckling [121]

### 3.5.1 Abstract

A novel highly stretchable gas sensor is reported that is based on pop-up antenna reconfiguration due to the strain induced by the swelling of a polydimethylsiloxane (PDMS) substrate when exposed to diethyl ether. When the swollen substrate is removed from the volatile solvent environment, the PDMS volume increase is reversed leading to compressive stress in an attached antenna transforming a 2D structure to a 3D structure through mechanically induced shaping. This provides a low cost and simple route to tune the antenna resonant frequency and gain in direct response to a chemical stimulus. Our proposed solvent sensor is able to measure 0 to 60% PDMS swelling corresponding to diethyl ether concentrations up to 1620 ppm via a resonant frequency shift from 4 to 2.4 GHz. A fatigue life study indicated  $10^{3.5}$  life cycles which demonstrates the durability of these sensors to accommodate large strain and repeatability of the sensing process. Multiphysics Finite Element Method (FEM) modelling of the mechanical and RF simulations along with analytical results based on an equivalent circuit model were in good agreement with experimental data and demonstrate the potential of these structures as sensors.

*Index Terms*—Compressive stress, pop-up antenna, diethyl ether, vapor, PDMS, sensor.

### 3.5.2 Introduction

Chemical vapor environmental exposure can occur from accidental spill during manufacture, distribution, and handling. These gases are often combustive and can threaten public safety [122]. Therefore, designing cost effective low profile wireless sensors capable of monitoring the presence of chemical vapor is of great interest. Diethyl ether is a common laboratory solvent extensively used in chemical and pharmaceutical industries and as an anesthetic for humans in developing countries. Inhalation can irritate the throat and nose, and long-term exposure can cause drowsiness, respiratory issues or even death [123], [124]. It is a volatile chemical that is highly flammable and potentially explosive. Thus, the hazards associated with diethyl ether make monitoring necessary. To date various attempts have been made to integrate smart materials into antenna designs for wireless gas sensing [125]-[132]. For example, changes to the conductivity of carbon nanotubes or graphene integrated in an antenna, in the presence of chemical vapors led to a shift in resonant frequency [125]-[130]. Furthermore, the variation in optical, electrical and chemical properties of customized nanoparticle dispersion inks with

exposure to a particular gas to tune antenna responses have been exploited. For instance, the authors of [131] proposed a gas sensor by embedding an electrode coated with copper acetate-based chemi-resistive ink in a loop antenna, while [132] integrated Tin oxide ( $\text{SnO}_2$ ) nanoparticles into a microstrip patch for detection of ethylene gas. However, the reported materials and fabrication processes can be expensive and complex.

The potential of PDMS (polydimethylsiloxane) swelling in sensing applications is reported in [133]-[141] with antenna properties when embedded in PDMS substrate in [142]-[145]. These studies focused on the substrate flexibility due to its low Young's modulus (less than 2 MPa) at room temperature [146]. However, only a few publications have applied the swelling behavior of PDMS to vapor detection [147], [148]. These designs are spacious and complex, respectively. This paper contributes by combining the swelling properties of PDMS on exposure to chemical vapor with the compressive buckling technique reported in [149]-[155] to introduce a state of the art and robust design for a highly stretchable gas sensor. The elastomeric nature of the substrate allows it to conform to different mounting surfaces [14] and the compressive buckling mechanism transforms the planar antenna design to 3D without complicated fabrication methods. Previous literature has focused on the mechanical aspects of the method and to the authors' knowledge, no research has been reported to use this technique for engineering the antenna performance.

### **3.5.3 Sensor design and working principle**

The proposed vapor sensor mechanism is based on the resonant frequency shift of a half wavelength dipole antenna made of 30  $\mu\text{m}$  thick copper by swelling and deswelling of its elastomeric substrate. The antenna was designed at 2.4 GHz when flat on a double-layer substrate comprising a top layer of thin PDMS and a bottom layer of high permittivity ceramic. In order to achieve a stretchable layout, the dipole is selectively bonded to the fully swollen PDMS substrate. This enables the unbonded sections to buckle out of plane in response to the induced strain from PDMS swelling and deswelling to avoid fracture. Fig. 3.13 presents a schematic of the described system including the dipole, PDMS and ceramic substrate. The proposed antenna was designed for 3 different swelling PDMS thicknesses of 0.4 mm, 0.8 mm and 1 mm. All geometrical dimensions and electrical parameters are given in Table 3.7 and Table 3.8, respectively. Note that the dimension values in Table 3.6 are for PDMS before swelling.

Table 3.7 Parameters for the designed antenna.

Parameters	$l_1$			$W_1$	$l_2$	$W_2$	$l_3$	$W_3$	F	$T_3$
	$T_2=0.4$	$T_2=0.8$	$T_2=1$							
dimensions (mm)	16.31	17.68	18	1	50	18	80	30	3	1

Table 3.8 Properties of the substrate used in the sensor design at 2.4 GHz.

Electrical constant	Value
$K_{PDMS}$	2.55
Conductivity <sub>PDMS</sub> (S/m)	$2 \times 10^{-5}$
$K_{Ceramic}$	20
Conductivity <sub>Ceramic</sub> (S/m)	$10^{-11}$
$K_{Swollen PDMS}^*$	$2.8 \pm 0.04$
Conductivity <sub>Swollen PDMS}^*</sub> (S/m)	$0.13 \pm 0.004$

\* At the end of a complete diethyl ether vapor exposure cycle.  $K$  denotes the relative permittivity.

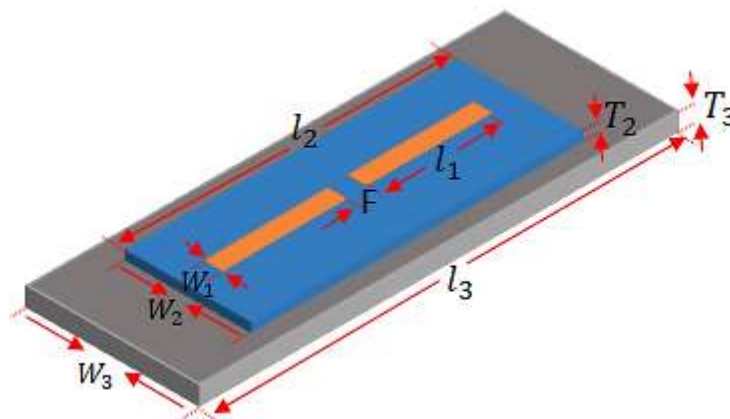


Fig. 3.13 Geometry of the designed half wavelength dipole antenna.

All dielectric properties were measured and averaged in the frequency range of 2.4 GHz to 4 GHz using a SPEAG Dak 3.5 probe with a Rohde and Schwarz ZVL 6 GHz network analyzer using the manufacturer procedure [124]. A modified equivalent circuit model was proposed to describe the pop-up dipole antenna [156], [157]. This RLC circuit was validated through comparison to multi-physics simulations which were divided into three steps:

- 1- Electromagnetic simulation to design a planar half-wave dipole antenna selectively

bonded to a fully swollen PDMS substrate at 2.4 GHz. Fully swollen PDMS was modeled by considering 60% biaxial.

strain ( $l_2^{Swollen} = 80 \text{ mm}$ ,  $W_2^{Swollen} = 28.8 \text{ mm}$ ) and assigning the measured electrical properties ( $K_{\text{Swollen PDMS}}$  and  $\text{Conductivity}_{\text{Swollen PDMS}}$ ) reported in Table 3.7. Thickness increment in the fully swollen PDMS was theoretically predicted by the Flory–Huggins model [154] which shows 48  $\mu\text{m}$  increase in the PDMS thickness.

- 2- Mechanics simulation to model the antenna deformation with respect to 0 to 60% strain release in the elastomeric substrate. Strain is:  $\epsilon_x = \Delta l_2 / l_2$  and  $\epsilon_y = \Delta W_2 / W_2$ , where  $l_2$  and  $W_2$  are the length and width of the PDMS support before swelling. Note that, based on the simulation results, 60 % biaxial deformation of the PDMS substrate is the maximum strain level leading to a buckled antenna without the adjacent buckled sections becoming short-circuited. Therefore, 60% swollen PDMS is considered as fully swollen throughout this paper.
- 3- Electromagnetics simulation of the deformed antenna resulting from step 2 on a relaxed PDMS.

The finite element method was adopted in electromagnetic simulations to calculate reflection coefficient values (dB) of the antenna. The simulations were performed using COMSOL multiphysics v. 5.3a [7] in which adaptive meshing convergence were used. For efficiency and simplicity, all the metal layers are modelled with transition boundary condition with prescribed thicknesses.

The designed dipole was coupled to the structural mechanics module in COMSOL Multiphysics® software for evaluating the antenna shape after releasing 0-60% biaxial strain due to the PDMS swelling in the presence of chemical vapor (Fig. 3.14). The degree of PDMS swelling in exposure to diethyl ether was measured experimentally and will be discussed in detail later.

To model the PDMS, a Young's modulus of 549 kPa, a Poisson ratio of 0.5 and mass density of 927  $\text{kg/m}^3$  were used as the materials is considered as a nearly incompressible hyper-elastic material [159]. The Yeo model in the nonlinear structural materials module of COMSOL was used to simulate the mechanical behavior of the substrate which can appropriately fit the measured nonlinear stress-strain data of isotropic elastic materials [160]. The strain energy density function for this hyper-elastic model is given by:

$$W = \sum_{i=1}^3 c_i (I_1 - 3)^i \quad (3.2)$$

where  $W$  is strain energy density function,  $I_1$  is the first invariant of the Cauchy-Green deformation tensor,  $c_1$ ,  $c_2$  and  $c_3$  are Yeo material parameters with values of 36.85, 5.81 and 0.97 kPa respectively.

The high permittivity ceramic (commercial name: E-20) is a  $\text{MgTiO}_3\text{-CaTiO}_3$  composite provided by T-Ceram [161]. Its function is to reduce the dipole length by dielectric loading and increase the amount of frequency shift after deformation. The simulated antenna was fed with  $50 \Omega$  coaxial cable and a perfectly matched layer (PML) was used

for the radiation boundary condition. Mesh refinement was adopted to increase the simulation accuracy.

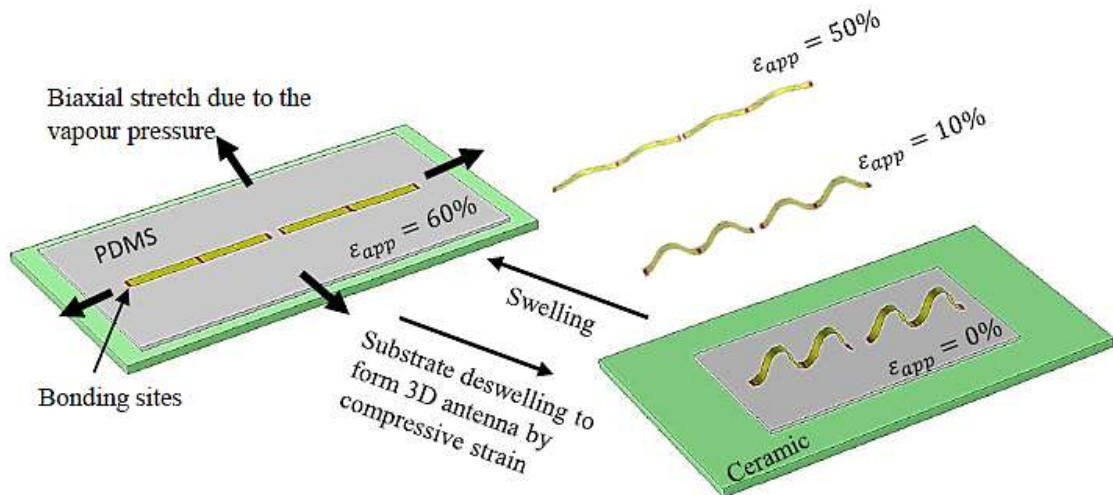


Fig. 3.14 Schematic illustration of the designed popup sensor by mechanically guided 3D assembly through PDMS swelling and deswelling.

### 3.5.4 Equivalent circuit model

The pop-up dipole antenna is a buckled version of its straight counterpart with similarities in terms of radiation pattern and current distribution. In [156] a four-element circuit model for a straight dipole antenna was derived which can be adapted to the pop-up dipole antenna by altering the lumped components values, as shown in Fig. 3.15(a). The proposed circuit model including  $L_{31}$ ,  $R_{31}$ ,  $C_{31}$  and  $C_{32}$  represents the feed-point impedance of a half wavelength dipole and the element values depend only on the physical dimensions of the antenna. To adapt the model, we need to consider the post-buckling behaviour of the antenna. As shown in Fig. 3.15, the buckled structure is formed by compressive buckling of a flat 2D ribbon which is bonded at either end to a strained elastomeric support. Relaxing the strain induces compressive forces

which buckle the ribbon into an arc, as shown in Fig. 3.15(c). The compressive strain ( $\epsilon_{comp}$ ) induced in the antenna is defined as [154]:

$$\epsilon_{comp} = -\frac{l_{rib}^0 - l_{rib}}{l_{rib}^0} \quad (3.3)$$

where  $l_{rib}$  is the distance between bonding sites after compression and  $l_{rib}^0$  is the total length of the ribbon.

between two bonding sites. The vertical displacements of the ribbon during the buckling were considered in [154]-[156] and the static deflection amplitude of the buckled ribbon ( $A$ ) is given by [154]:

$$A = \frac{2l_{rib}^0}{\pi} \sqrt{\frac{l_{rib}^0 - l_{rib}}{l_{rib}^0} - \epsilon_c} \quad (3.4)$$

where  $\epsilon_c = \pi^2 h^2 / [3(l_{rib}^0)^2]$  is the critical strain for the buckling of the ribbon antenna which is the maximum strain that the antenna can bear while staying flat and  $h$  is the ribbon thickness ( $30\mu m$ ). By substituting the post buckling parameters into the equations derived in [152], the value of each lumped element in the equivalent circuit model can be calculated by (3.5) -(3.7).

$$C_{31} = \left\{ \frac{12.0674(Nl_{rib})}{(\log(\frac{2Nl_{rib}}{T}) - 0.7245)} \right\} \text{ pF} \quad (3.5)$$

$$C_{32} = 2Nl_{rib} \left\{ \frac{\frac{0.89075}{0.89075}}{((\log(\frac{2Nl_{rib}}{T}))^{0.8006} - 0.861)} - 0.02541 \right\} \text{ pF} \quad (3.6)$$

$$L_{31} = 0.2 l_1 \left\{ (1.4813 \log(\frac{2l_1}{T}))^{1.012} - 0.6188 \right\} \mu H \quad (3.7)$$

where  $l_{rib} = \frac{l_{rib}^0}{(1 + \epsilon_{app})}$ ,  $\epsilon_{app}$  is the strain value in the PDMS,  $N$  is the number of bends,  $T = \frac{W_1}{4}$ ,

$l_1$  is the length of each dipole arm and  $W_1$  is the width. As the total length of the buckled ribbon has not changed, the self-inductance  $L_{31}$  is approximately equal to the self-inductance of a straight dipole. However, buckling introduces mutual capacitances between adjacent ribbon arcs that form a meander section. The mutual capacitance of a meander section is given by:

$$C_m = \frac{\pi K_0 A}{\ln\left[\left(\frac{l_{rib}}{T}\right) + \sqrt{\left(\frac{l_{rib}}{T}\right)^2 - 1}\right]} \quad (3.8)$$

where  $K_0$  is the relative permittivity of free space. The resonant frequency shift can be described in terms of the variation in the antenna capacitance. Therefore, the resonant frequency  $f_0$  of a pop-up dipole is as follows:

$$f_0 = \frac{1}{2\pi \sqrt{L_{31}(C_{31} + C_{32} + C_m/2N)}} \quad (3.9)$$

To validate our proposed theoretical model, the predicted resonant frequencies of the dipole antenna with  $N = 2$  over 0 to 60% strain in the PDMS substrate are compared with numerical simulations in COMSOL Multiphysics and presented in Fig. 3.16. The largest deviation in the resonant frequency observed between our model and simulation result was 3.8%.

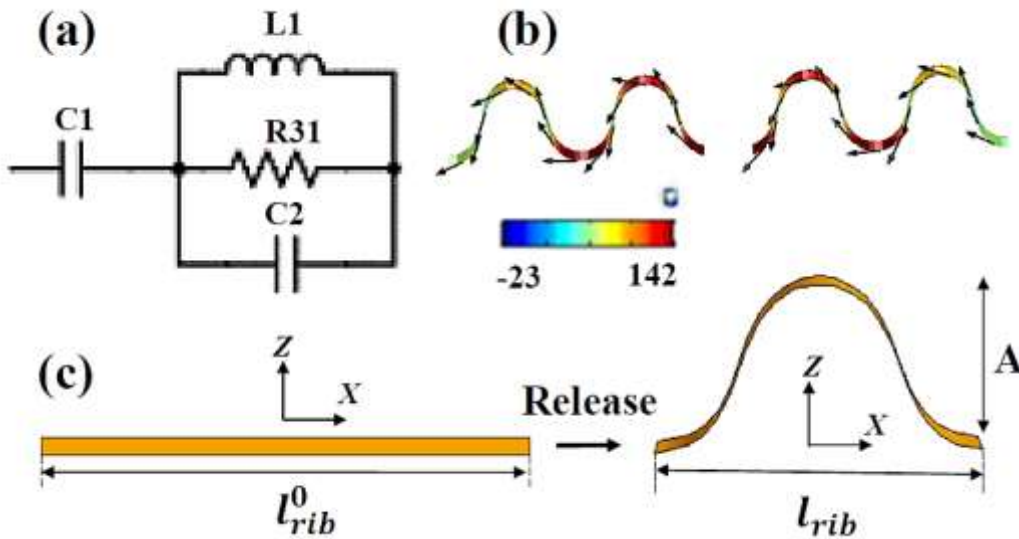


Fig. 3.15 (a) Equivalent circuit model used for modelling pop-up dipole antenna [152]. (b) Surface current (A/m) on the buckling dipole after deswelling and returning to the original PDMS size. (c) Diagram of mechanics model for a meander section of a buckled ribbon.

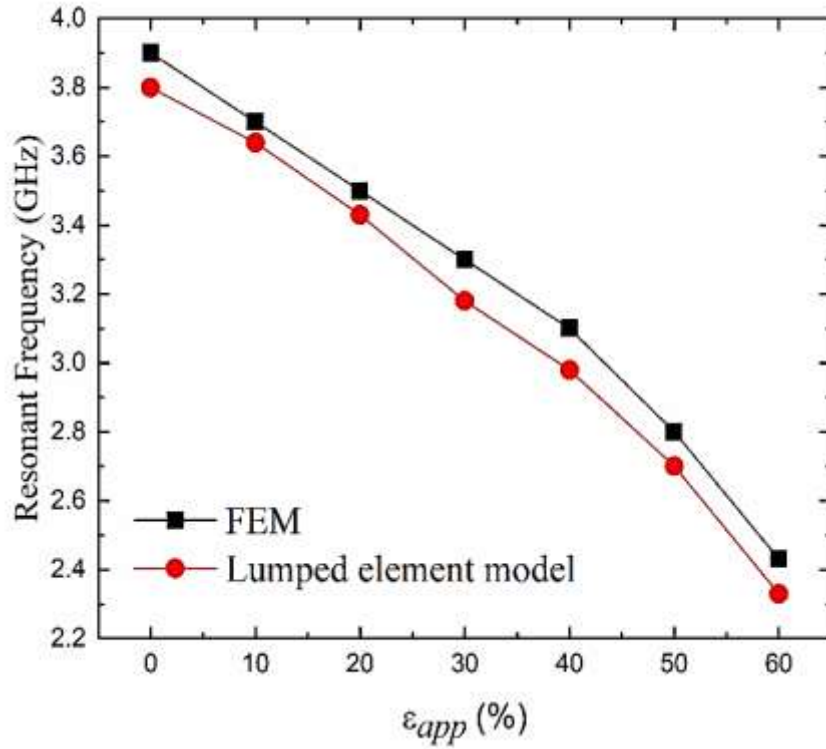


Fig. 3.16 Resonant frequency as a function of strain value in PDMS ( $\epsilon_{app}$ ). Plot compares the results from numerical simulation in COMSOL and predictions from geometry-based model. Note that  $N = 2$  in this study.

### 3.5.5 Numerical results and discussion

In order to study the effect of thickness on the antenna input reflection coefficient ( $S_{11}$ ) and the effect on sensitivity when the sensors are repeatedly stressed and relaxed, three sensor designs with PDMS thicknesses of 0.4, 0.8 and 1mm on a 1mm ceramic substrate are considered. Initially, a dipole was designed for 2.4 GHz on 0.4 mm thick PDMS. The antenna and substrate were placed on a 1 mm thick high-permittivity ceramic substrate to reduce the antenna size. In the next step, the model was coupled to the COMSOL mechanics simulation module to capture all mechanics aspects of 2D to 3D antenna transformation process including strain distribution during compressive buckling after releasing 0 to 60% strain in the PDMS. These amounts of strain are due to the PDMS swelling after exposure to specific concentrations of diethyl ether and will be discussed in Section 3.5.6. Hollow shell mesh elements were used for the 2D precursor of copper ribbon which is a good conductor with small skin depth meaning the hollow elements will adequately model current flow, while dielectric materials (PDMS and ceramic) require solid elements as E-field penetrates them. The load ramping technique was applied to model the nonlinear buckling process. This method solves a nonlinear problem with gradually increasing load values and using the solutions from each step as the starting value for the next step [162]. As the structure will become unstable when a load reaches its buckling value, applying load in small steps helps for better convergence. By changing the number of

bonding sites between dipole and PDMS, the number of buckles ( $N$ ) in each arm of the dipole can be determined. Fig. 3.17 presents the Von Mises stress (MPa) in both the antenna (for  $N = 2$  and  $N = 5$ ) and PDMS substrate (with 60% strain release). It can be seen that the amount of stress at the bend apexes plus the locations near the bonding sites is higher than all other locations for all dipole configurations. This high amount of cyclic stress could cause damage to the substrate and dipole after a finite number of cycles.

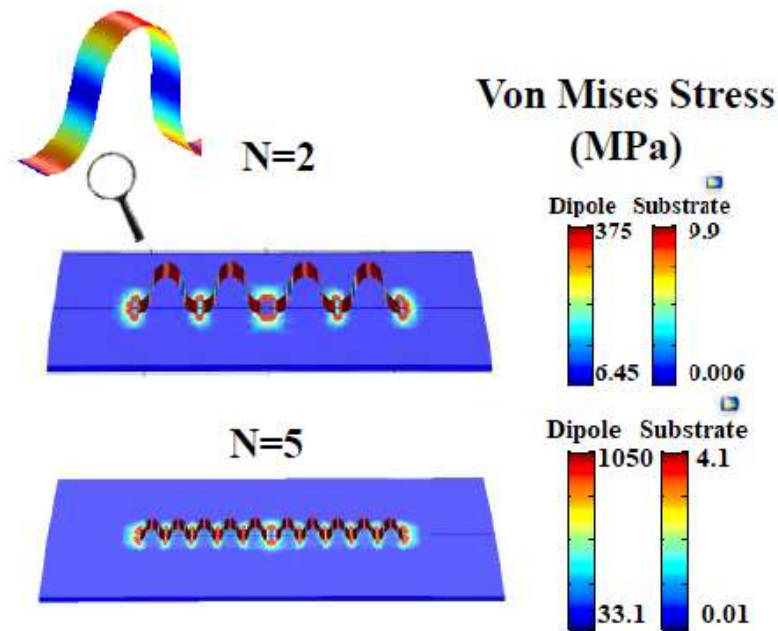


Fig. 3.17 Von Mises stress (MPa) in the antenna and substrate after release of 60% strain in the PDMS

Simulation results show that the maximum level of stress on the dipole significantly increases for higher values of  $N$ , and the number of high stress regions increases with  $N$ . As the PDMS substrate has a Young's modulus nearly 5 orders of magnitude lower than the metallic ribbon ( $E_{\text{copper}} = 130$  GPa), there are high stress levels at the bonding sites. In the final step, the buckled antenna was again coupled to the RF simulation to determine the amount of resonant frequency shift in the  $S_{11}$  plot. When planar, the high permittivity substrate serves to reduce the antenna electrical size. When buckled, the pop-up structure achieves a reduction in length by expanding the antenna into the third dimension off the substrate.

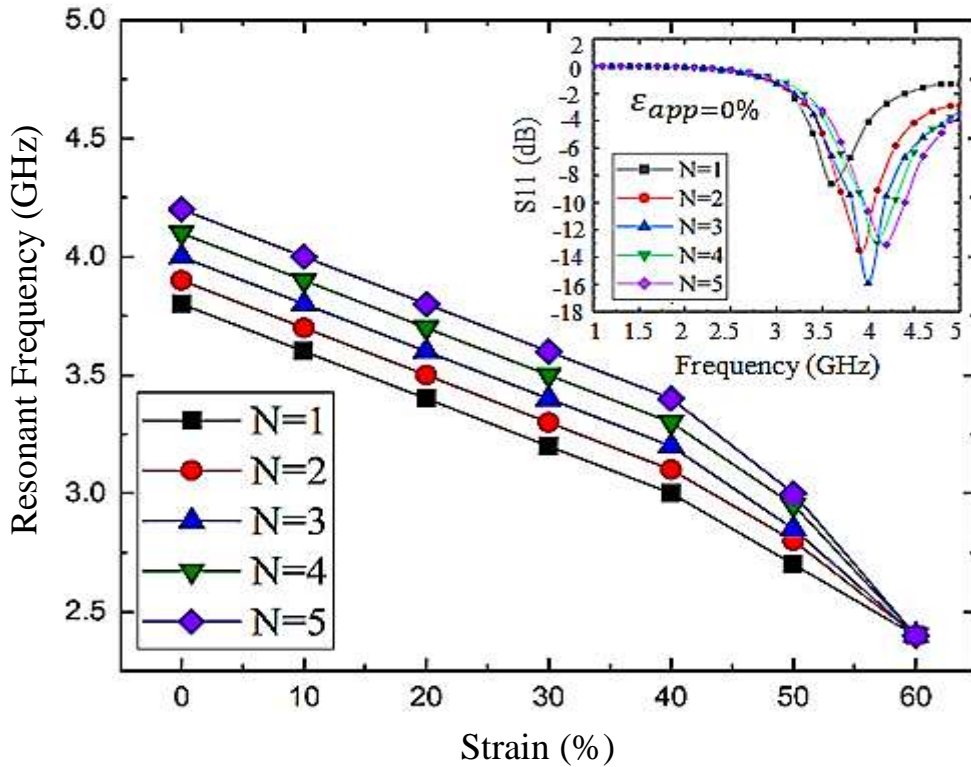


Fig. 3.18 Resonant frequency shift vs strain value in the PDMS substrate for the half wavelength dipole antenna with buckled sections  $N = 1$  to  $N = 5$ . Inset figure presents reflection coefficient (dB) versus frequency (GHz) for the sensor in the relaxed mode with unswollen PDMS and shows a good antenna match with  $N = 2$  and  $N = 3$ .

Simulation results show that the maximum level of stress on the dipole significantly increases for higher values of  $N$ , and the number of high stress regions increases with  $N$ . As the PDMS substrate has a Young's modulus nearly 5 orders of magnitude lower than the metallic ribbon ( $E_{\text{copper}} = 130 \text{ GPa}$ ), there are high stress levels at the bonding sites.

In the final step, the buckled antenna was again coupled to the RF simulation to determine the amount of resonant frequency shift in the  $S_{11}$  plot. When planar, the high permittivity substrate serves to reduce the antenna electrical size. When buckled, the pop-up structure achieves a reduction in length by expanding the antenna into the third dimension off the substrate. During nonlinear buckling the dipole is bent severely and the number of bends, the height from the PDMS substrate, and finally the distance between neighboring conductors in each arc are crucial factors in determining the amount of resonant frequency shift. The currents flow in opposite directions on adjacent vertical paths and have a cancelling effect, as seen in Fig. 3.15(b), which is stronger when the antenna has multiple bends which are closely packed. In this case, the effective electrical length of the antenna becomes smaller while the physical length remains constant. During compressive buckling, mutual series capacitance arises between the two dipole arms which decreases the overall capacitance. This factor as well as the reduced dielectric loading caused by the separation between the substrate and the bent

dipole leads to a resonant frequency up-shift. Fig. 3.18 shows the simulated resonant frequency (GHz) versus strain values in the PDMS substrate for  $N$  values of 1 to 5. The up shift in the  $S_{11}$  graph, confirms that the dipole becomes electrically shorter as expected. The impedance match varies with  $N = 2$  or  $N = 3$  providing the best match. Although antennas with  $N > 2$  show better frequency shift (and better impedance match for  $N = 3$ ), in order to decide which  $N$  value is optimum, the mechanical performance must also be considered. As discussed, cyclic mechanical buckling exerts stress at the antenna–elastomer bonding sites which could lead to eventual failure. Therefore, the mechanical aspects of the design as well as durability should be taken into account and a fatigue study is presented to characterize the optimum  $N$  value. Fatigue is a primary cause of damage to structures when subjected to a cyclic loading and can lead to failure at loads below the yield stress limit. The fatigue mechanism consists of crack initiation and crack propagation which leads to progressive and unrecoverable damage. Therefore, the *number of cycles* required for fatigue *crack initiation* with the COMSOL Multiphysics fatigue module was studied. A stress-life method using the Wöhler curve approach [163] was applied to predict the number of stress cycles the dipole sustains before failure. Fig. 3.19 presents the fatigue study results for the buckled dipole where it can be seen that the peaks and the bonding sites are the locations most likely to fail. The possibility of failure at these points is almost a thousand times higher than other locations. The practical values will be somewhat lower in practice because the FEA simulation assumes a perfect bonding of dipole with PDMS substrate without any delamination, while in experiment, all bonds are imperfect. Similarly, by investigating the stress at the bonding locations (Fig. 3.17) it was realized that with more buckles ( $N$ ) and thus larger bend angles at the bonding sites the possibility of failure due to the fatigue increases. Therefore,  $N = 2$  is considered as an optimum value for the remaining analysis as it provides a good input match with a lower fatigue risk. The same 0 to 60% strain analysis was performed on a 0.8 mm PDMS substrate causing a frequency shift from 3.74 GHz to 2.4 GHz and on a 1 mm thick substrate causing a shift of 3.58 GHz to 2.4 GHz. Fig. 3.20 shows the reflection coefficient ( $S_{11}$ ) plot for 60% strained and strain-free substrates with different thicknesses of 0.4 mm, 0.8 mm and 1 mm. It can be seen that thinner PDMS provides an improved antenna input match for both the swollen and unswollen modes and the stress simulation results in Table 3.9 show the maximum Von Mises stress on the PDMS substrate decreases with increasing thickness.

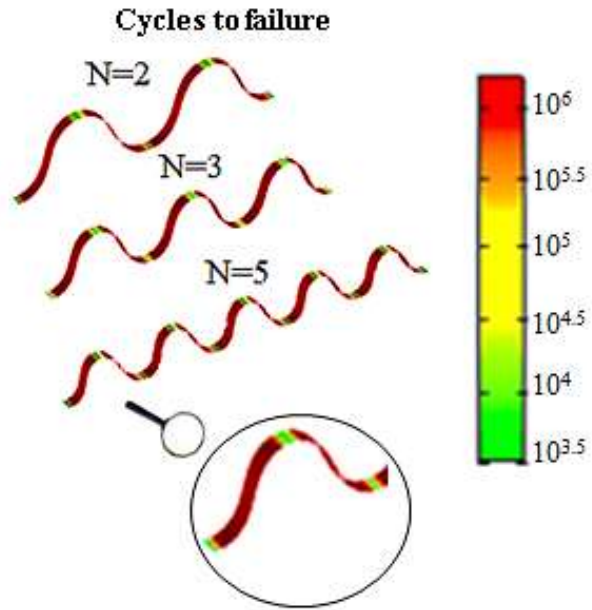


Fig. 3.19 Number of cycles to failure for the half wavelength dipole antenna on a PDMS substrate after release of 60% strain.

Table 3.9 Maximum stress level in the PDMS substrate with different thicknesses.

Maximum Von Mises Stress	$T_2 = 0.4 \text{ mm}$	$T_2 = 0.8 \text{ mm}$	$T_2 = 1 \text{ mm}$
MPa	9.9	4.8	4.44

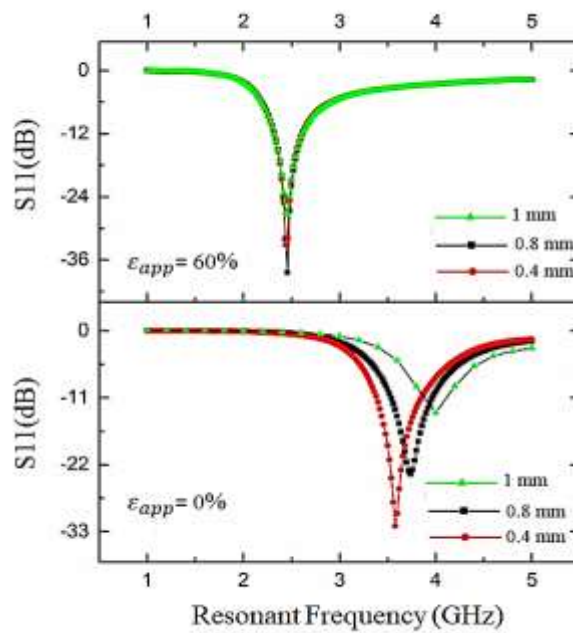


Fig. 3.20 Reflection coefficient (dB) versus frequency (GHz) for half wave dipole on a PDMS substrate with thicknesses of 0.4, 0.8 and 1mm for 60% strained PDMS and strain-free PDMS substrate.

### 3.5.6 Experiment

PDMS pads were cast using the procedure mentioned in [147]. The test environment was a desiccator with an internal diameter of 17 cm, external diameter of 21 cm and internal height of 24 cm. 50 cm<sup>3</sup> of diethyl ether was added to the bottom of the desiccator beneath a perforated disk which supported the PDMS elastomer while allowing exposure to the vapor. Three rectangular PDMS pads with the same width and the length as in Table I but different thicknesses of 0.4 mm, 0.8 mm and 1 mm were placed onto the perforated disk. A flat glass lid was used to seal the desiccator to allow view of the elastomeric substrates. To measure the degree of PDMS swelling with respect to the vapor exposure time, photographs were taken every 30 s. ImageJ software was used to calculate the degree of swelling (biaxial strain percentage) in each photograph. Fig. 3.21(a) presents the degree of swelling in the three PDMS samples with thicknesses of 0.4 mm, 0.8 mm and 1 mm. From this graph it can be concluded that as the original PDMS thickness is decreased, the swelling response gets faster and thus response time drops. Therefore, 0.4 mm thickness was chosen for the rest of the experiment. For fabricating the sensor, three PDMS substrates of 0.4 mm were placed in the desiccator for 45 min, this led to 60 % swelling in the PDMS. At this point, three flat dipoles with dimensions given in Table I were bonded to each of the fully swollen PDMS substrates with six bonding sites using commercial adhesive (Super Glue, Loctite Company). Then the samples were removed from the desiccator to deswell. Fig. 3.21(b) presents the fabrication process. When the PDMS/ceramic samples with the antennas were completely deswelled, they were placed into the desiccator above 50 cm<sup>3</sup> diethyl ether and a concave lid with a hole was used to allow connection to a network analyzer (Rohde and Schwarz ZVL 6 GHz) during the gas exposure period. Fig. 3.22(a) shows the measurement set up. By removing the sensors from the desiccator, the dielectric constant, conductivity and thickness of PDMS layers returned to the pre-exposure values after 25 seconds (for a complete exposure cycle). Therefore, the sensor could be utilized multiple times. Each sensor function was experimentally measured twice for a complete cycle of exposure-removal of vapor-exposure to reveal fabrication errors. No noticeable resonant frequency drift occurred throughout the experiments which demonstrated the repeatability of the process. To evaluate the sensitivity, the gas concentration needed to trigger a noticeable shift in the resonant frequency was determined [164]-[166]. Table 3.10 presents the vapor concentration in the desiccator with respect to the exposure time and the range of resonant frequency shift due to the PDMS swelling. These values are the average performance of three sensor samples with PDMS thickness of 0.4 mm. Measurements in Fig 3.22(b) show that the minimum detectable vapor concentration is 36 ppm which corresponds to 180 MHz frequency shift and once the sensor is activated, it can detect

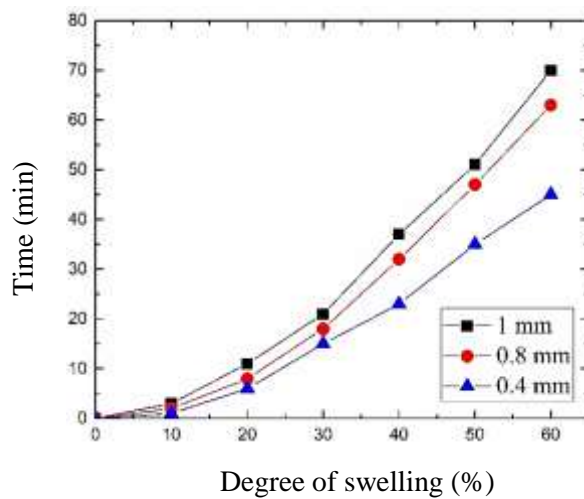
vapor at the minimum rate of 0.6 MHz/ ppm (between low and high concentrations) which is better than the values reported in the recent publications [125], [131], [132], [133]. This rate value is greater (1.1 MHz/ppm) for low vapor concentrations (lower than 300 ppm) which is attributed to the saturation effect in the PDMS substrate. We repeated the same experimental procedure for the solvent acetone. Measurement verified that the swelling degree of the PDMS upon exposure to the acetone vapor is around 63% lower than for diethyl ether. Therefore, by extracting the resonant frequency vs gas concentration graph, our proposed sensor can distinguish between these two vapors. Fig. 3.22(b) represents the experimental frequency response upon the introduction of various concentration of diethyl ether. It is interesting to note that the response is linear (slope of  $-6.23 \times 10^{-4}$ ) and Fig. 3.22(c) compares the resonant frequency shift with respect to the vapor concentration of diethyl ether and acetone. Linear interpolation was used to obtain the curves. Finally, we compare the proposed gas sensor with previous works in the literature in Table 3.11.

Table 3.10 Summary of measure

<b>Time (min)</b>	<b>Vapor concentration (ppm)</b>	<b>Degree of swelling (%)</b>	<b>Frequency shift (<math>\Delta f = f1 - f2</math>) MHz <math>f1 = 4</math> GHz</b>
<b>1</b>	36	10	180
<b>6</b>	217	20	440
<b>15</b>	540	30	620
<b>23</b>	828	40	790
<b>35</b>	1260	50	1020
<b>45</b>	1620	60	1520

Table 3.11 Comparison with other works.

Method	Target gas	Response rate (MHz/ppm)	Recovery time(s)	Reference
<b>Carbon Nanotube (CNT) integrated with patch antenna</b>	ammonia (NH <sub>3</sub> )	0.4	30	[4]
<b>Graphene Oxide and nano-silver ink loaded on patch antenna</b>	ammonia (NH <sub>3</sub> )	0.05	----	[10]
<b>Tin Oxide nanoparticles integrated with patch antenna</b>	Ethylene	0.07	----	[12]
<b>Pop-up dipole antenna integrated with PDMS</b>	diethyl ether	0.6-1.1	25	This work

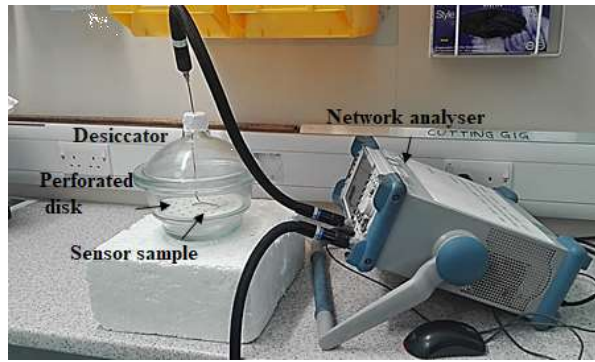


(a)

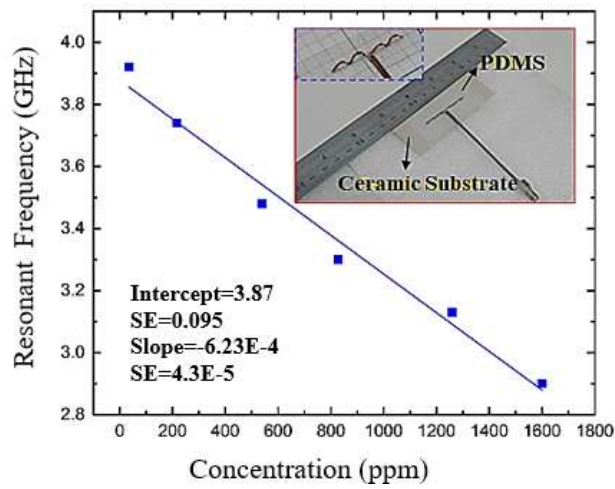


(b)

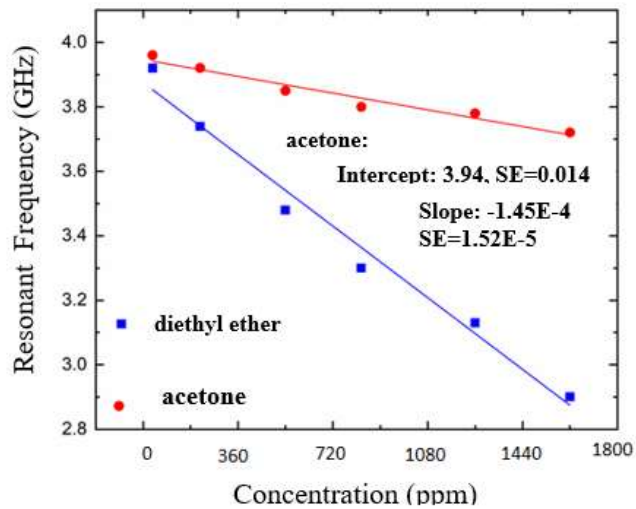
Fig. 3.21 (a) Swelling degree vs exposure time for three thicknesses (0.4 mm, 0.8 mm and 1 mm). (b) Fabrication process. Step one, the flat dipole antenna is superglued at six bonding zones (specified with red color). In step two, the antenna is attached to the fully swollen PDMS in the desiccator. Note that all experiments were performed in clean room to ensure the safety and finally in step three, the sample is removed from the desiccator to deswell. At this point due to the induced compressive force, buckled dipole is formed.



(a)



(b)



(c)

Fig. 3.22 (a) Experimental set up, sensor placement in desiccator. (b) Experimental curve for resonant frequency vs diethyl ether concentration (ppm), Linear correlation between frequency and gas concentration could be used for calibrating the sensor. (c) A comparison of resonant frequency vs gas concentration curve between diethyl ether and acetone.

### **3.5.7 Summary and conclusion**

The design principle and assembly of a 3D vapor sensor based on compressive buckling is reported. The resonant frequency of the antenna sensor varies with diethyl ether concentration which is attributed to the stretch and compression of the antenna through swelling/deswelling of the PDMS support. Our proposed sensor has the advantage of improved sensitivity, simple fabrication and low cost compared to reported alternatives, which makes it a good candidate for cost-effective environmental monitoring for places such as laboratories and hospitals. Repeatability of the sensor performance was verified by both fatigue study (simulation) and experiment through measuring the outputs of three sensor prototypes and repeating each experiment twice. Future research will focus on wireless remote reading of the sensor using radar or link coupling techniques.

## 3.6 Pop-up Tunable Frequency Selective Surfaces for Strain Sensing [163]

### 3.6.1 Abstract

A 3D pop-up frequency selective surface (FSS) is presented that can be tuned by the amount of strain due to mechanical loading in its elastomeric substrate. The proposed FSS structure comprises periodic 2D crossed dipoles attached to the substrate at selective bonding sites. Strain release in the substrate induces compressive stress in the attached FSS, converting it to a 3D periodic pattern. With the out-of-plane displacement, the interaction with the incident field and mutual interactions between the elements are altered, resulting in a resonant frequency shift and a more stable response regarding the incident angles from  $0^\circ$  to  $45^\circ$ . A design of pop-up FSS structure is introduced for strain sensing applications. The potential sensor can measure up to 50% strain in the substrate by frequency down-shift from 3.1 to 2.4 GHz. Multiphysics finite element method modelling of the mechanical and RF simulation was in good correlation with the experimental data and demonstrates the potential of these structures as sensors.

*Index Terms*—Mechanical sensors, compressive stress, frequency selective surface (FSS), multiphysics simulation, strain.

### 3.6.2 Introduction

Frequency selective surfaces (FSS) also called spatial filters are periodic arrangement of metal patches or perforated metal screen elements on a dielectric substrate. These repetitive structures can modify the incident electromagnetic radiation by completely or partially transmitting (pass-band) or reflecting (stop-band), depending on the nature of the array element [168]. Low profile, tunability, dual polarization, angular stability and easy fabrication route are among the desired properties of FSSs. However, achieving all mentioned characteristics has been a challenge for FSS designers. To date various attempts have been made to design electronically or mechanically tunable FSS structures [169]-[174]. For example, the authors of [169] proposed a dual layer FSS layout loaded with variable capacitors to adjust the resonant frequency. Furthermore, an FSS structure consists of periodic pattern of circular loops connected through varactor diodes introduced in [170], which exhibits tunable operation. Although electronic tuning has many benefits, it suffers from several disadvantages, especially for large area FSSs, as it requires lots of controlling lumped elements for each unit cell as well as bias circuits to ensure RF/DC isolation. Other researchers [171]-[173] obtained tunability by integrating stimuli-responsive substrates such as liquid crystals and ferrites into the FSS structures. In this way, a resonant frequency shift achieved by changing the electrical properties

of the substrate is exposed to external excitation. Mechanical tunability is also proposed in [174] where the rotation of each 3D unit cell was controlled using a shaft connected to a motor. However, the reported method suffers from complex fabrication routes.

An alternative approach for tuning FSS layouts is introduced in this chapter, based on stretch/release or shrinkage of the substrate due to external stimuli such as force or temperature change to convert a 2D unit cell to a 3D one in a pop-up like fashion. Recently, more attention has focused on 3D FSS designs as they offer more frequency stability for different incident angles and polarization [175], [176]. However, most designs encounter difficulties in implementation and fabrication, as current 3D direct print is constrained by a limited range of 3D geometry shapes and reliance on expensive metallic inks and plastics. Pop-up techniques introduce a simple 3D indirect fabrication route for any shape and type of materials, based on mechanical deformation of the soft substrate. According to this technique, two ends of a 2D precursor are strongly bonded to the pre-strained substrate, while the other parts are free on the substrate [170]. Following the complete release of the substrate pre-strain, the 2D precursor goes under compression and may buckle up. Our proposed FSS design operates between two states of planar and fully buckled in response to environmental stimuli such as strain and temperature, which lends itself well for sensing applications. It can measure up to 50% strain frequency shift in the range of 2.4 GHz - 3.1 GHz. Moreover, as it starts buckling, it provides a more stable frequency response for incident angles up to 60°.

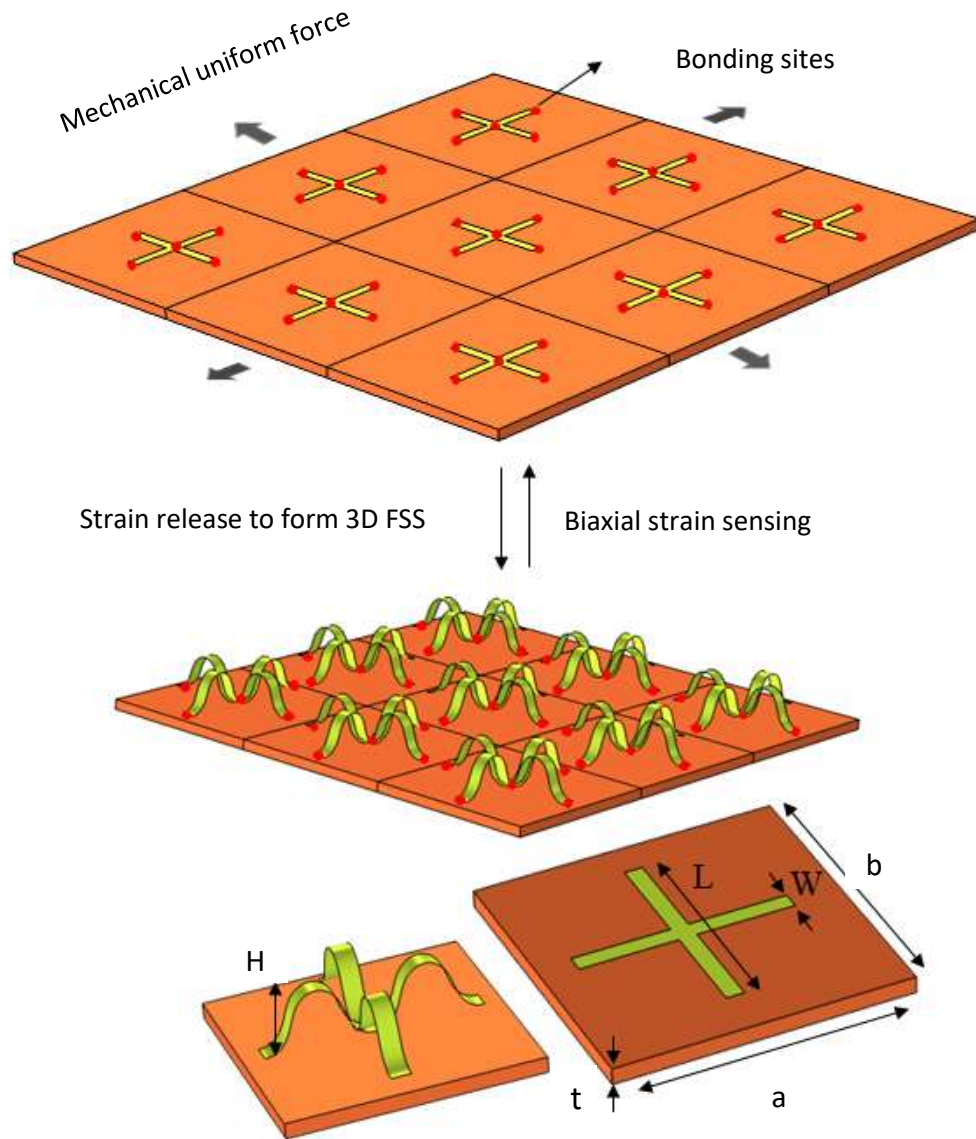


Fig. 3.23 Popup formation procedure of the FSS structure. A) Elastomeric substrate is under strain (2D unit cells), B) Substrate is relaxed and 3D unit cells are formed due to induced compressive force, C) Geometry parameters of each unit cell.

### 3.6.3 Design and working principle

#### *A Geometry of the Unit Cell*

The unit cell of the proposed FSS structure, when flat consists of 2D crossed dipoles, as shown in Fig. 3.23. The cell is repeated periodically along two directions  $\hat{x}$  and  $\hat{y}$  with length  $a$  and  $b$ . All geometrical dimensions are presented in Table 3.12. the spacing between adjacent unit cells defines the periodicity of the FSS structure which was tuned through parameter sweep to receive a good performance in terms of resonant frequency while keeping the whole dimension as small as possible. Moreover, this spacing must also be optimized to be sufficient enough to prevent the adjacent cells becoming short-circuited after the maximum stretch and release.

Table 3.12 Parameters for the designed FSS

Parameters	<i>A</i>	<i>B</i>	<i>L</i>	<i>W</i>	<i>T</i>
Dimensions(mm)	68.2	68.2	54	2	1

The substrate is made of Silicone rubber with a commercial name of Dragon Skin [119] with relative permittivity of 1.8 and conductivity of 0.004 S/m and thickness of 1 mm. The metallic patterns are made up of 35  $\mu\text{m}$ -thick copper foil.

### ***B. Fabrication method***

The fabrication began with cutting a copper sheet (Cu, 35  $\mu\text{m}$ ) into the desired shape using a cutting machine (Cricut Explore Air <sup>TM</sup> 2). The next step involved transferring the precursors onto a pre-stretched elastomer substrate (Dragon Skin, Smooth on). A commercial adhesive (Super Glue, Loctite Company) dispensed at desired bonding sites. There are some techniques reported in the literature for an almost perfect bonding [177], [182]. However, here our aim was the simplicity of fabrication, while receiving sufficient loading cycles. Slowly releasing of the pre-stain initiates the assembly process. The proposed design was a  $3 \times 3$  array on an elastomeric substrate. For mechanical stability, the sample was backed with a 12 mm thick sheet of Polystyrene foam ( $\epsilon_r = 1.04$ ), as depicted in Fig 3.24.



Fig. 3.24 Biaxial stretching of an elastomeric substrate.

### ***C. Simulation Procedure***

Multiphysics simulation using COMSOL V. 5.4 [7] has been performed to analyze the proposed structure. The simulation procedure is divided into three steps.

**Step one:** Full-wave electromagnetic simulation of the flat FSS unit

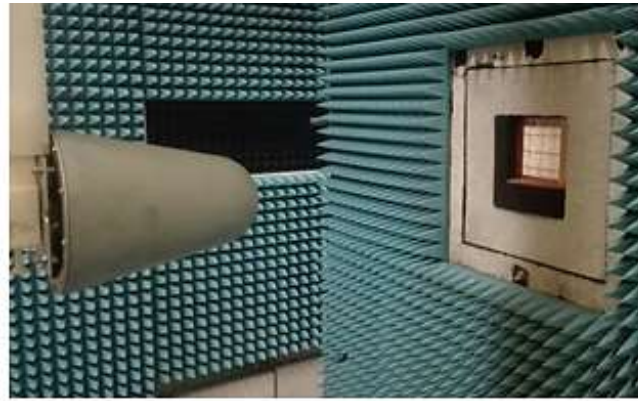
cell using the RF module, at 2.45 GHz. The finite element method was adopted to determine the functionality under different incident angles for both TE and TM polarizations. Adaptive meshing convergence was used and for simplicity and time, all metal strips were modelled imposing a transition boundary condition with prescribed thickness. The geometry of the unit cell in flat state was optimized through parameter sweep in order to resonate at 2.45 GHz.

**Step two:** Mechanics simulation using the structural mechanics module to model the unit cell deformation for up to 50% strain in the substrate. The elastomeric substrate was modeled as a solid element with Young's modulus of 166 [kPa], Poisson's ratio of 0.49 and mass density of  $927 \text{ kg/m}^3$ . Copper precursors were modeled by shell elements with prescribed thickness. The load ramping method was adopted to model nonlinear buckling. This method ensures the solution convergence by gradually increasing the applied load and using the solution of each step as the initial value for the following step.

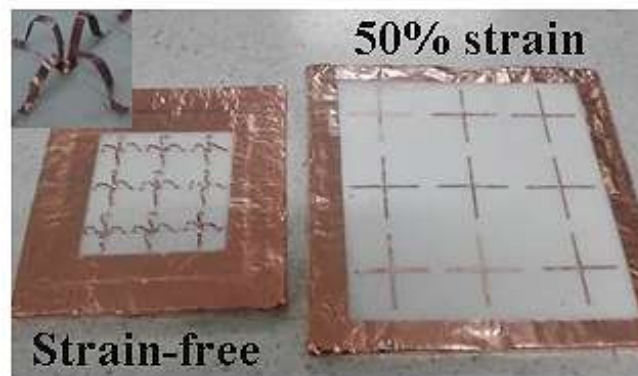
**Step three:** Full-wave electromagnetics simulation of the deformed unit cell (corresponding to 0 to 50 % deformation) obtained from step two on the relaxed substrate to recalculate the transmission responses under various incident conditions.

### **3.6.4 Results and discussion**

Measurement was carried out using two Rohde and Schwarz HL050 log periodic antennas at 0.6 m from a  $3 \times 3 \text{ m}^2$  absorbing panel containing the FSS and a Hewlett Packard 8722ES VNA for transmission system. The absorbing panel was loaded with a rotatable screen, thus allowing for angular measurement. To ensure consistency in the test, the system was calibrated before each measurement. Fig. 3.25 shows the prototypes and the experimental set-up. A unit cell of the proposed FSS design was illuminated by a normal plane wave, first with electric field polarized along the x-axis and the propagation vector along the z-axis (TE polarization) and next with electric field polarized along the y-axis and the same direction of propagation vector (TM polarization). A resonant frequency is clearly seen near 2.45 GHz for the flat state (50% strain in the elastomeric substrate). Tuning the FSS is accomplished by changing the strain value in the substrate and a resonance is seen at a higher frequency, around 3.1 GHz for a relaxed substrate (0% strain).



(a)



(b)

Fig. 3.25 (a) Experimental set-up and (b) FSS prototypes. The right-hand side sample has been undergone 50% strain in its elastomeric substrate and the left hand side sample is strain free.

Fig. 3.26 shows the resonant frequency shift of the FSS structure at normal incidence and for TM polarization as a function of equi-biaxial strain values in the elastomeric substrate. This frequency shift is mainly due to two effects after buckling. First, the induced compressive force causes the flat copper precursor to deform out of plane and expand into the third dimension. This out of plane displacement (which is specified by  $H$  in Fig. 3.23) leads to a gap between the substrate and the conductors and thus a change in effective permittivity felt by the crossed dipole patterns. Moreover, the buckled shape is observed to be electrically small viewed from the above. This can be understood by considering current cancellation between opposite conductors after buckling, as seen in Fig. 3.27.

The second reason for the observed resonant frequency shift is the fact that by relaxing the elastomeric substrate from its 50% stretched state, the inter-element spacing or periodicity of the FSS structure changes bi-axially and this factor affects the frequency response and causes a shift.

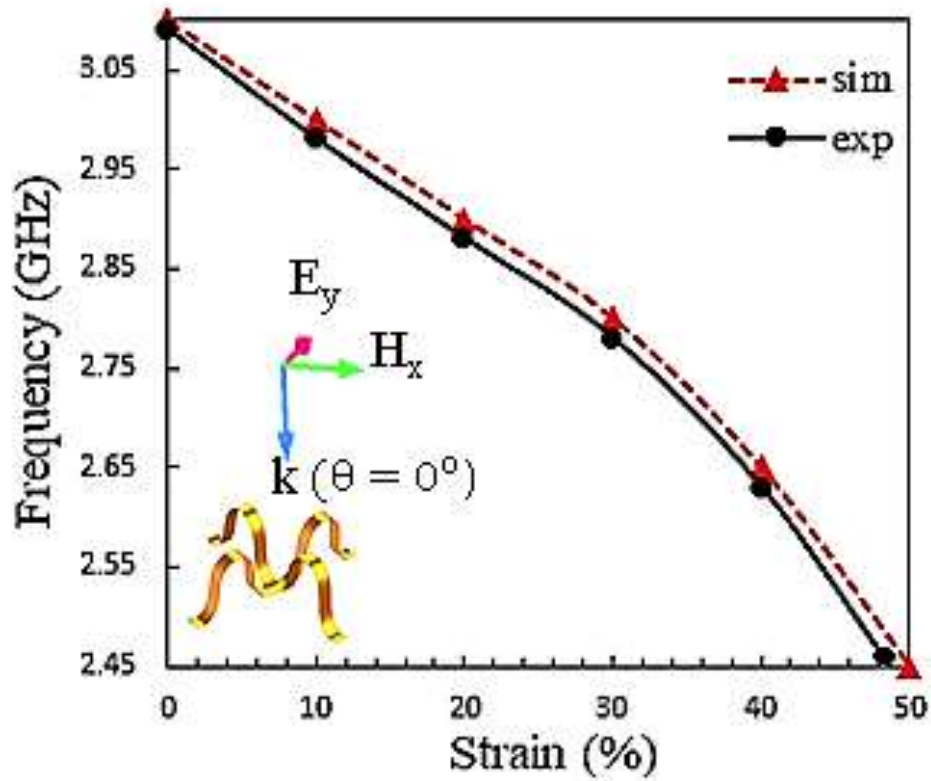


Fig. 3.26 Numerical and experimental results for resonant frequency shift vs strain values in the elastomeric substrate for normal incidence and TM polarization.

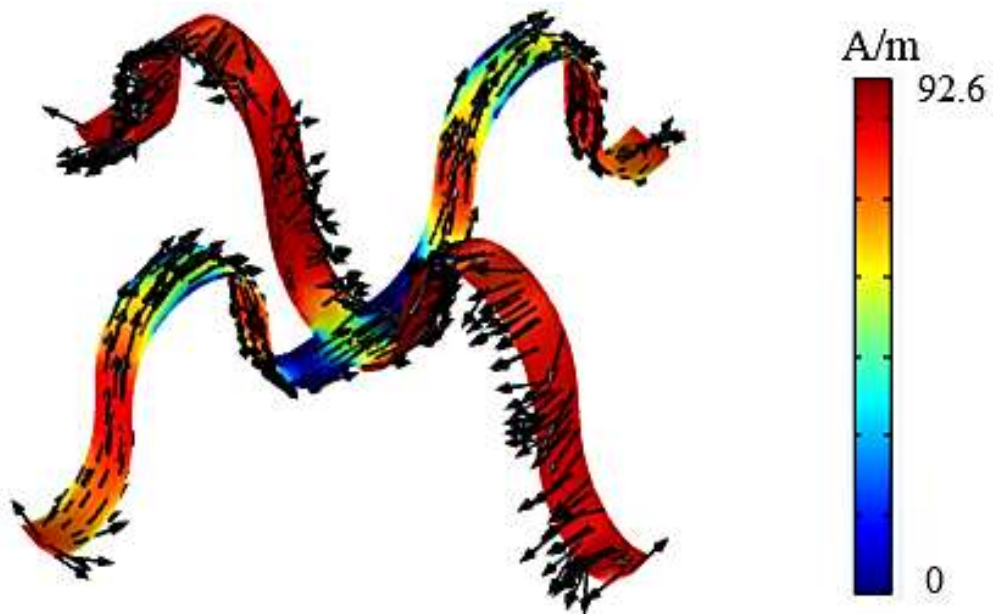


Fig. 3.27 Surface current (A/m) on the buckled cross dipole. The currents flow in opposite directions on adjacent vertical arms and have cancelling effect leading the structure to be electrically smaller than the actual physical size.

To investigate the stability of the proposed FSS design with regard to angle of incidence, the performance of the structure has been evaluated for oblique incidences. Therefore, the originally z-directed propagation vector was rotated at angles of  $\theta = 0^\circ, 15^\circ, 30^\circ$  and  $45^\circ$  from the z-axis.

In order to perform a thorough comparison between the stability of the flat FSS and the pop-up one, two types of structure are investigated. The first structures are strain free 3D FSS layouts after 10%, 20%, 30%, 40% and 50% strain release in the substrate and the second structures are scaled versions of the flat FSS, with the same periodicity as the first series. The purpose of choosing these two structures is to keep the periodicity factor the same and then compare the stability of 2D and 3D unit cells. Fig. 3.28 demonstrates the improved stability of the pop-up FSS for TM polarization in comparison to the flat counterpart. Fig. 3.29 shows the transmission responses vs frequency for different angles of incidence and TE polarization.

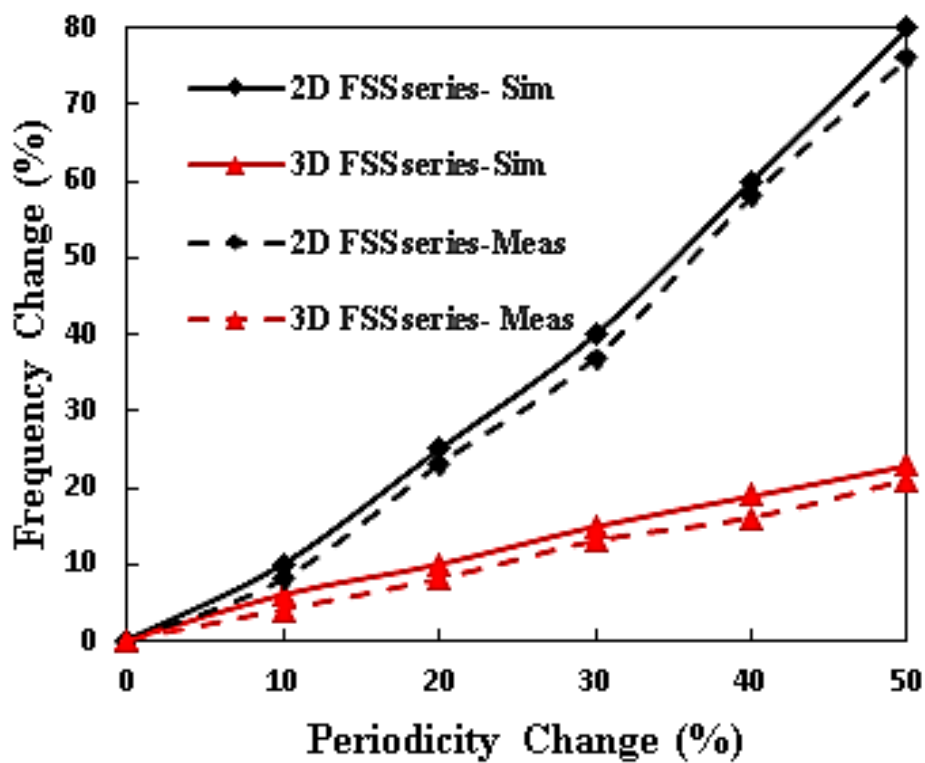


Fig. 3.28 A comparison between an FSS structure with 3D buckled crossed dipole unit cell and similar flat counterparts with equal periodicity in terms of stability.

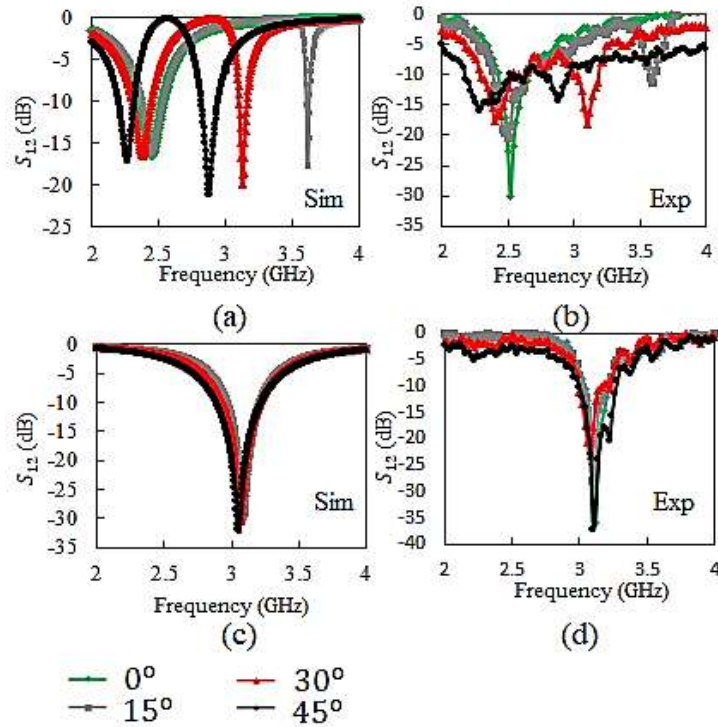


Fig. 3.29 Numerical and experimental results for TE incidence at four angles of  $0^\circ$ ,  $15^\circ$ ,  $30^\circ$  and  $45^\circ$ . (a) 50% strain in the elastomeric substrate (simulation). (b) 50% strain in the elastomeric substrate (experiment). (c) Strain-free elastomeric substrate (simulation). (d) Strain-free elastomeric substrate (experiment).

### 3.6.5 Summary and conclusion

The design and assembly of a 3D pop-up FSS structure based on a compressive buckling is briefly presented. The proposed FSS design can detect 0 to 50% strain in its elastomeric support by resonant frequency change in the range of 2.45 to 3.1 GHz. This pop-up design provides a good level of stability and compared to any other 3D FSS designs reported in the literature which are fabricated using direct routes such as 3D printing, the proposed layout is fabricated indirectly via simple and cost-effective way of stretch and release. This design has a potential in sensing applications such as temperature where an environmental change causes a strain variation in the embedded substrate. Therefore, future research will focus on integration of the designed pop-up FSS with smart polymers.

## Chapter 4

### Pop-up Capacitive Sensors

---

#### **4.1 Wireless Finger-Worn Strain Sensing Using Passive RFID Technology submitted paper.**

##### **4.1.1 Abstract**

Single-chip sensing capability via affordable sensor tags enables substantially lower cost, easily deployed, maintenance-free, battery-free and multiple stimuli monitoring platform. The sensing mechanism is based on the chip self-tuning which can provide a digital data about the change in the local environment. Using this capability, here we propose a passive UHF radio frequency identification tag design which is worn on the finger to detect the level of bending wirelessly. The design includes a small loop antenna integrated with a RFID chip and a pop-up capacitive sensor. The proposed capacitive sensor tag is tuned for EPC Class 2 Generation 2 UHF RFID readers at 866 MHz and can detect the degree of finger bending by transmitting a 5-bit sensor code which provides a direct measure of the antenna's impedance. Our proposed sensor tag has been tested on three candidates each for three times to assure reliability and durability. Electromagnetic simulation was in good correlation with the experimental results and demonstrates the potential of this design for discreet real-time monitoring of finger bending which could be utilized for paralyzed patients who requires, constant, or remote monitoring as needed.

*Index Terms*— Passive, Radio frequency identification, Self-tuning, Sensor code, Wireless.

##### **4.1.2 Introduction**

Finger joint movement monitoring is of great importance for health monitoring including rehabilitation of patients, particularly after stroke. Hand therapists record any changes before and after any treatment by measuring joint angles [179]. Rehabilitative treatments with assistive devices have been effectively used for these patients particularly for large motions and extremity function. However, long-term rehabilitation, such as finger movement and , remains challenging. The ideal assistive rehabilitation device for joint movement monitoring should be inexpensive, portable and comfortable so that it can be easily used for daily monitoring [180], [181]. One approach to estimating finger angles is through sensory gloves

[182]-[187]. Many commercial devices and research samples have been developed involving embedded bend sensors, to detect joint movements. The main drawback of most of these gloves is that they are bulky and expensive and some required complicated calibration [188].

To date various attempts have been made to design stretchable sensors for finger bending monitoring purpose. For example, in [189] a wearable hand module based on fiber Bragg grating (FBG) strain sensor is introduced. measurement based on the reflective principle of light passing through the optical fibre varies with degree of bending in fingers. Researchers in [190] proposed a textile-based strain sensor which can be used for monitoring joint motions by easily integrating them onto different non-planar surfaces of human body. Similarly, in [191] a novel graphene woven fabric (GWF)/polydimethylsiloxane (PDMS) composite is suggested as a highly flexible, sensitive strain sensor capable of detecting joint motions. Although these studies provide good methods for finger bending level measurements, they suffer from several disadvantages including complex mechanical structure and digital calibration methods. Wireless capabilities enabling radio frequency waves to be sent over long distances with no degradation is feasible through passive RFID tags.

In this paper we report a novel strain sensor for finger joint movement detecting based on capacitive sensing using RFID technology. According to this method, our proposed system comprises of three elements, a small loop antenna, a self-tuning RFMicron Magnus S2 transponder chip [188] and a pop-up capacitive sensor. The chip provides two key features: a 5-bit sensor code and a 5-bit on-chip RSSI (Received Signal Strength Index) code which can be transmitted to an external RFID reader. The sensor code indicates the impedance mismatch between the chip and the tag antenna, while the RSSI code relays the strength of the incoming signal from the reader. The antenna has been designed to work at 866 MHz. The performance of the antenna and the pop-up capacitive sensor will be explained in detail further. The novelty of this design mainly lies in the sensing part as the initial design for a RFID antenna on a ring was proposed in [193] and we have adapted that design to the new chip that allows for sensing. This paper is organized as follows, Section 4.1.3 describes the design and simulation of the antenna, Section 4.1.4 provides the designing procedure of the pop-up capacitive sensor. Section 4.1.5 analyzes the experimental result and Section 4.1.6 concludes the paper.

### **4.1.3 Antenna Design and Numerical Results**

Loop antenna is considered small when conductor length is around ten times less than resonant wavelength. The loop behaves as a lumped inductance which can be resonated at the

desired frequency with an integrated capacitor, forming a high-Q parallel tuned circuit. This variable capacitor helps to tune the antenna in a wide range of frequencies. The designed antenna is linearly polarized and the far field radiation pattern of it is equivalent to that of a small electric dipole normal to the loop plane [193]. Gamma matching is employed here for impedance matching purpose. As a small diameter conductor parallel and in close vicinity with the main radiating element, which carries only a fraction of the main element current while being exposed to the same electrical field strength [190]. This can act as effective transformer of the antenna input impedance. The designed antenna has been designed for three middle finger diameters, 19 mm, 21 mm and 23 mm. CST MWS™ [195] simulations were performed for 2 mm foam substrate. The simulation model consisted of the main copper foil element, substrate material, lumped element tuning capacitor, source and finger phantom. Fig. 4.1 illustrates the schematic of the antenna. Table 4.1 presents the dimension values.

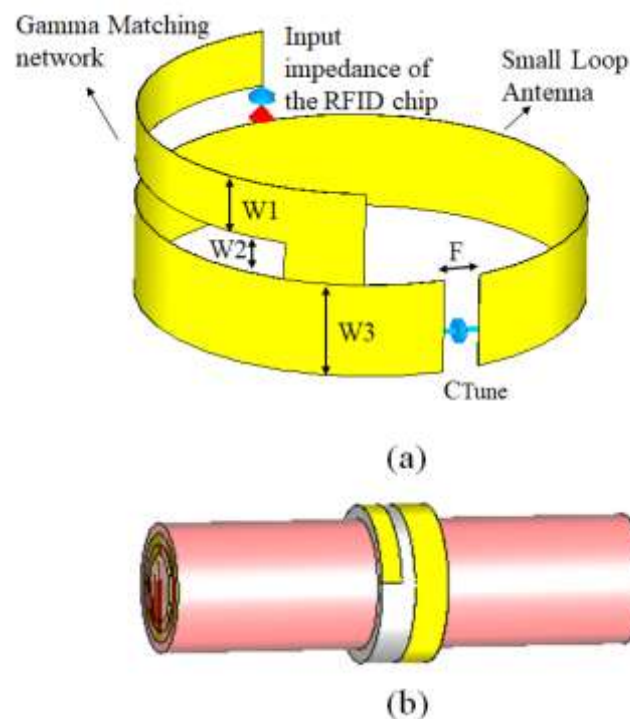


Fig. 4.1 Schematic of the antenna design. (a) Dimension parameters of the antenna layout. (b) Antenna design on a finger model.

Table 4.1 Dimension values of the antenna structure.

<b>F</b>	<b>W1</b>	<b>W2</b>	<b>W3</b>
2 mm	3mm	2mm	5mm

The prototype antennas were fabricated from copper foil with a thickness of 35  $\mu\text{m}$ . For input coupling, the gamma match is presented here, where also the additional inductance offered by the gamma match can be utilized in cancelling or part-cancelling the capacitive reactance of the RFID chip. An empirical method was used to design the gamma match and achieve an efficient match to the impedance of the RFID device, which in this case is the RFMicron Magnus S2 transponder chip with an input impedance of  $1.63\Omega - j 61.07 \Omega$  at 866 MHz and a read sensitivity of -18.5 dBm. The simulated finger model was an 80 mm long four-layer cylindrical human tissue model, as shown in Fig. 4.1 (b) and Fig. 4.2, with the parameters given in Table 4.2 [193].

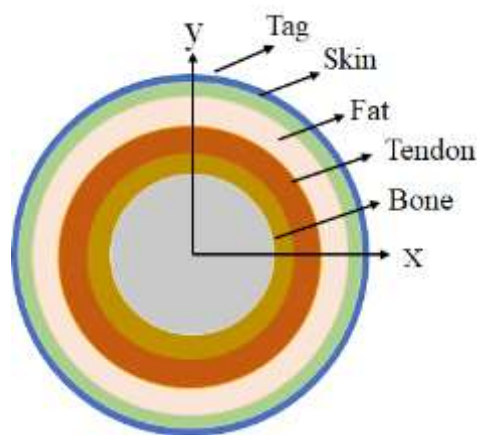


Fig. 4.2 Finger phantom 4-layer cylindrical model, including bone, tendon, fat, skin and the mounted tag.

Table 4.2 Electrical properties of different layers of the finger phantom

Material	$\epsilon_r$	$\sigma$ (S/m)	Outer Radius (mm)
Bone	20.6	0.33	5
Tendon	45.6	0.79	6.5
Fat	11.3	0.11	9
Skin	41	0.9	10.5
Foam	1.05	<0.0002	9.5/10.5/11.5

Initial simulations have been performed using the main loop and 50  $\Omega$  discrete port. Starting from the smallest diameter, the inductance values are 50 nF, 54 nF, 58 nF, resulting in tuning

capacitor values of 0.6 pF, 6.25 pF, 0.58 pF at center frequency of 866 MHz. Adding the equivalent impedance of the RFID port and initial CTune values, a process was employed to adjust CTune and the gamma match starting point for best reflection coefficient values for the three ring sizes. Fig. 4.3(a) depicts the reflection coefficient- frequency plot of the designed antenna. Surface currents and radiation pattern plots are shown in Fig. 4.3(b) and 4.3(c). The main beam direction is in the plane of the ring. The prototypes were made from self-adhesive copper foil. Immersing the foam substrate in hot water it to be formed easily around the finger without crack. 80 gsm office paper was used as the tuning capacitor dielectric [193]. With the ring on the finger, the capacitor was adjusted to tune the antenna to the European RFID band. Adjustment of the gamma match starting point was also carried out to optimize the read range.

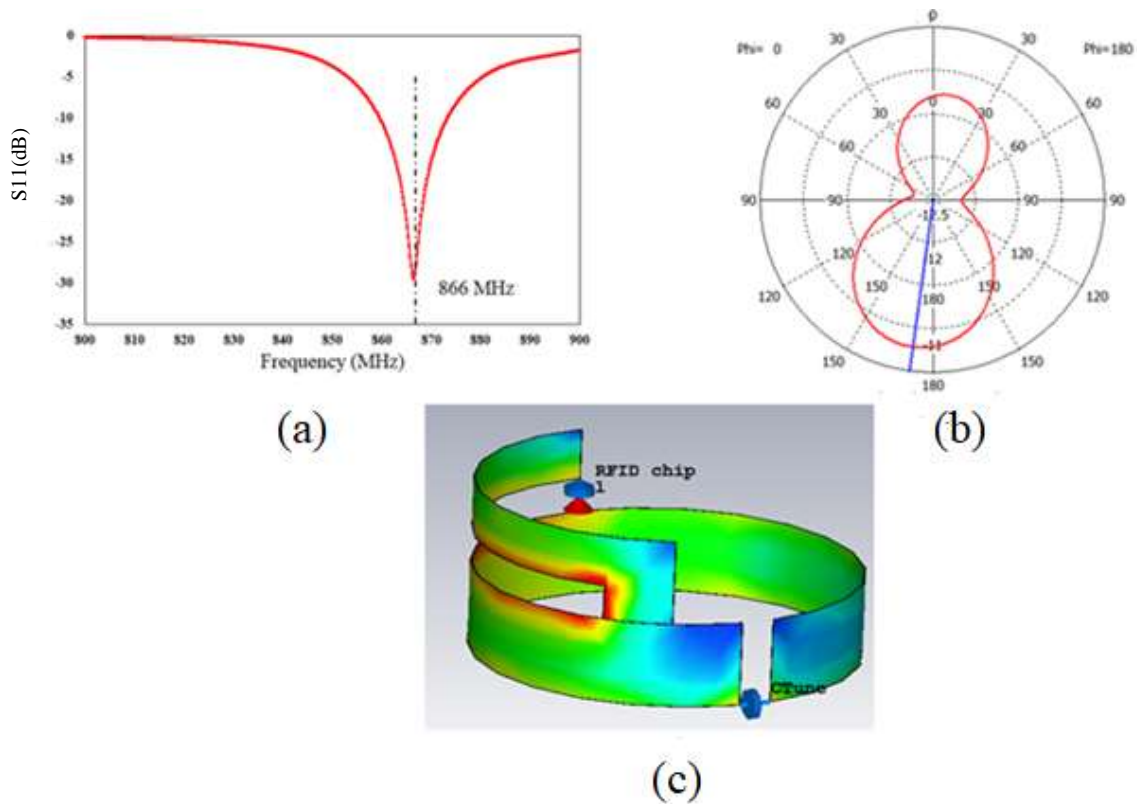


Fig. 4.3 (a) Reflection coefficient values (dB) versus frequency (S11). The antenna resonates at 866 MHz with the bandwidth of ~15 MHz. (b) Simulated realized gain plot for the ring (diameter: 21 mm) which denotes -11.3 dB. (c) Simulated surface current for the single finger phantom.

#### 4.1.4 Pop-up Capacitive Sensor Design

A capacitive sensor has been designed using compressive buckling technique [149]. This sensor simply consists of two metallic plates, an elastomeric substrate and silicone sheet as the dielectric (with dielectric constant ( $\epsilon_r$ ) of 1.8, conductivity ( $\sigma$ ) of 0.0004 [192]) with thickness

of 1.5 mm between two terminals , one plate (ground) is perfectly bonded to the elastomeric substrate and the second terminal is selectively bonded to the substrate which gives it the freedom to buckle when the substrate undergoes stress. This sensor can be tuned mechanically by changing the distance between the two metallic plates when working between two states, fully flat and fully popped-up. This sensor is installed on PIP joint of the finger and the capacitance values are changed with respect to the bending degree of the finger joint. Fig. 4.4 illustrates the schematic of the designed sensor in flat state.

The Simulation has been performed using COMSOL Multiphysics by coupling five main modules, Structural mechanics module to simulate the deformation of the capacitive sensor with respect to the degree of strain, Multibody Dynamic module for modeling the finger joints, nonlinear material module to model the hyper-elastic elastomeric substrate and electrostatics module to measure the capacitance at each bending state [7]. The simulation procedure is divided into two steps.

**Step one:**

Mechanics simulation using the structural mechanics module to model the multilayered finger model and the multibody dynamics module to model the joints by hinges. The finger and elastomeric substrate were modeled solid elements and copper precursors were modeled by shell elements with prescribed thickness. The load ramping method was adopted to model nonlinear buckling. This method ensures the solution convergence by gradually increasing the applied load and using the solution of each step as the initial value for the following step.

**Step two:**

Electrostatic simulation of the designed sensor on the multi-layered finger model to calculate the capacitance value while the finger is deforming from straight state ( $\theta = 0^\circ$ ) to the fully bent state ( $\theta = 90^\circ$ ).

Fig. 4.5 shows the working mechanism. Table 4.3 presents the dimension of the sensor design. Fabrication of the designed capacitive sensor starts from fully conforming the moving plate on a finger phantom when it is fully bent and then gluing both ends of it to the elastomeric substrate. Fig. 4.6 illustrates the fabrication route.

In order to model the finger joints to provide a more accurate simulation results, hinges have been simulated using Dynamic Multibody module in COMSOL. Fig. 4.7 presents the model. The designed sensor is placed on the first joint which is called proximal interphalangeal joints (PIP) [193]. The second joint, distal interphalangeal (DIP) joints help to stretch the elastomeric substrate while bending on the joint. The capacitive sensor changes the distance between two

plates while buckling from 0.06 pF to 1.04 pF when fully bent.

Table 4.3 Dimension values of the capacitive sensor design

Parameter	Dimension (mm)
<b>L</b>	50
<b>W</b>	20
<b>L1</b>	10
<b>W1</b>	10
<b>L2</b>	10
<b>W2</b>	5
<b>B</b>	0.1

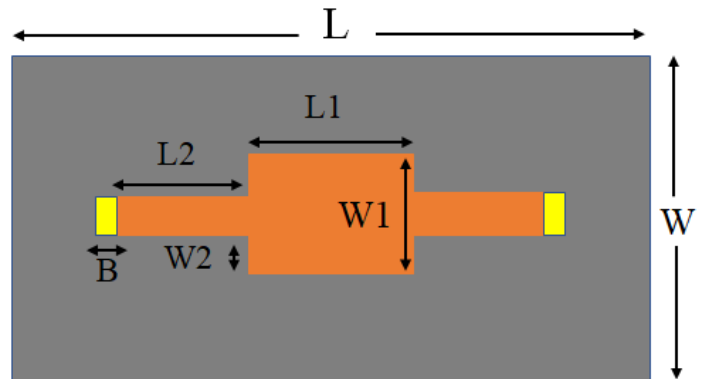


Fig. 4.4 Geometry of the capacitive sensor.

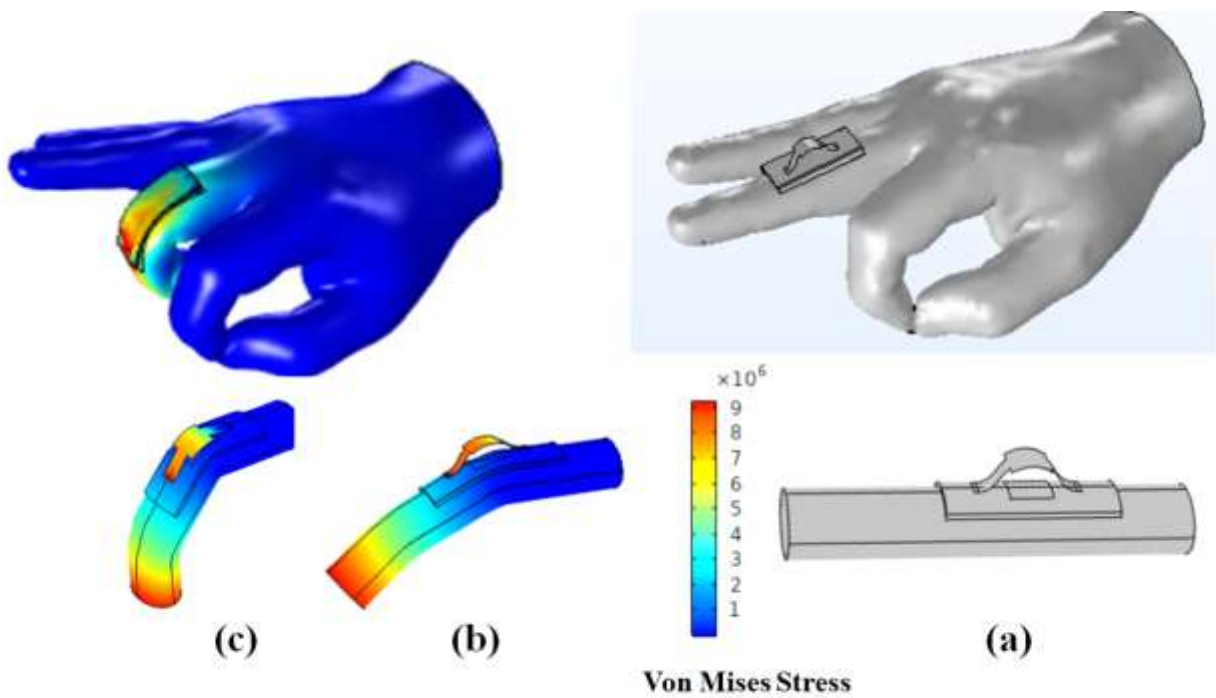


Fig. 4.5 Schematic of pop-up capacitor sensor on hand phantom. (a) When finger is straight ( $\theta = 0^\circ$ ), (b)  $\theta = 30^\circ$ , (c)  $\theta = 60^\circ$ .

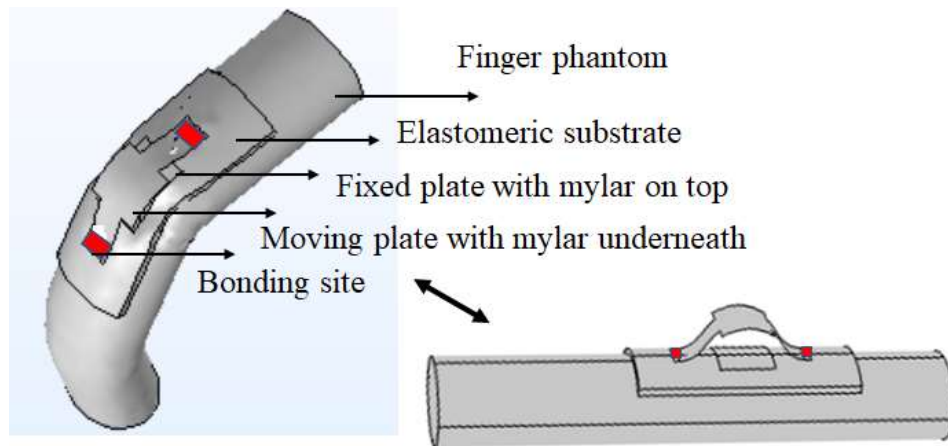


Fig. 4.6 Fabrication route of the capacitive sensor on finger phantom.

capacitive sensor on finger phantom.

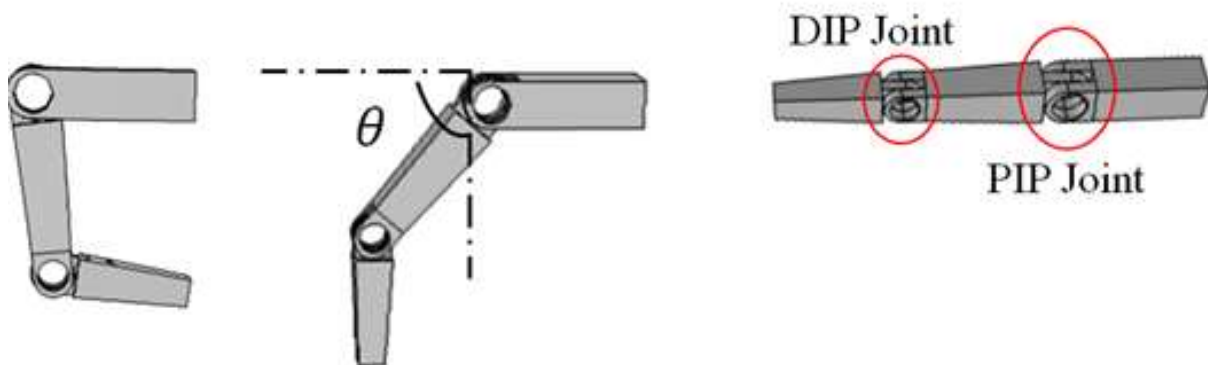


Fig. 4.7 Schematic of finger joints modelled with hinges in Comsol Multiphysics.

### 4.1.5 Experiments

The RFMicron Magnus S2 chip required turn-on power is  $-16.1$  dBm and the tuning capacitance range is  $2-3$  pF in parallel with  $2284 \Omega$  [188]. The chip covers all international RFID frequency bands from  $860$  MHz to  $960$  MHz and can change its capacitance between  $2$  to  $3$  pF in the presence of a detuning element. The total capacitance for the antenna model is [198]:

$$C_{total}(n) = C_{min} + nC_o \quad (4.1)$$

where  $C_{total}(n)$  is the total capacitance,  $C_{min}$  is  $2$  pF based on data sheet of the chip,  $n$  is the

sensor value in the range of 0–31 and  $C_0$  is a tunable step (1 pF/31) within the 1 pF tunable range. Therefore, for antenna simulation, the chip impedance was fixed to  $1.63\Omega - j 61.07 \Omega$ , at 866 MHz (corresponding to 3 pF). As the received sensor codes from the RFID reader indicates the capacitance change, it can be an effective indirect way to measure capacitance values below 1pF which is problematic due to the stray capacitance introduced by the meter and associated leads. In this case, the received sensor codes were compared to the results received from a tag connected to different capacitors in the range of 0 pF to 1pF.

Using a Voyantic UHF RFID measurement system, sensor codes and read range measurements were performed over five angles given in Fig. 4.8, where  $0^\circ$  denotes the straight finger, and  $90^\circ$  denotes the fully bent finger. The experiment has been performed on three candidates to demonstrate the applicability of the design. Each experiment has been repeated two times to ensure the durability of the sensor. Fig. 4.8 shows the sensor prototype on finger and different level of joint bending is illustrated.

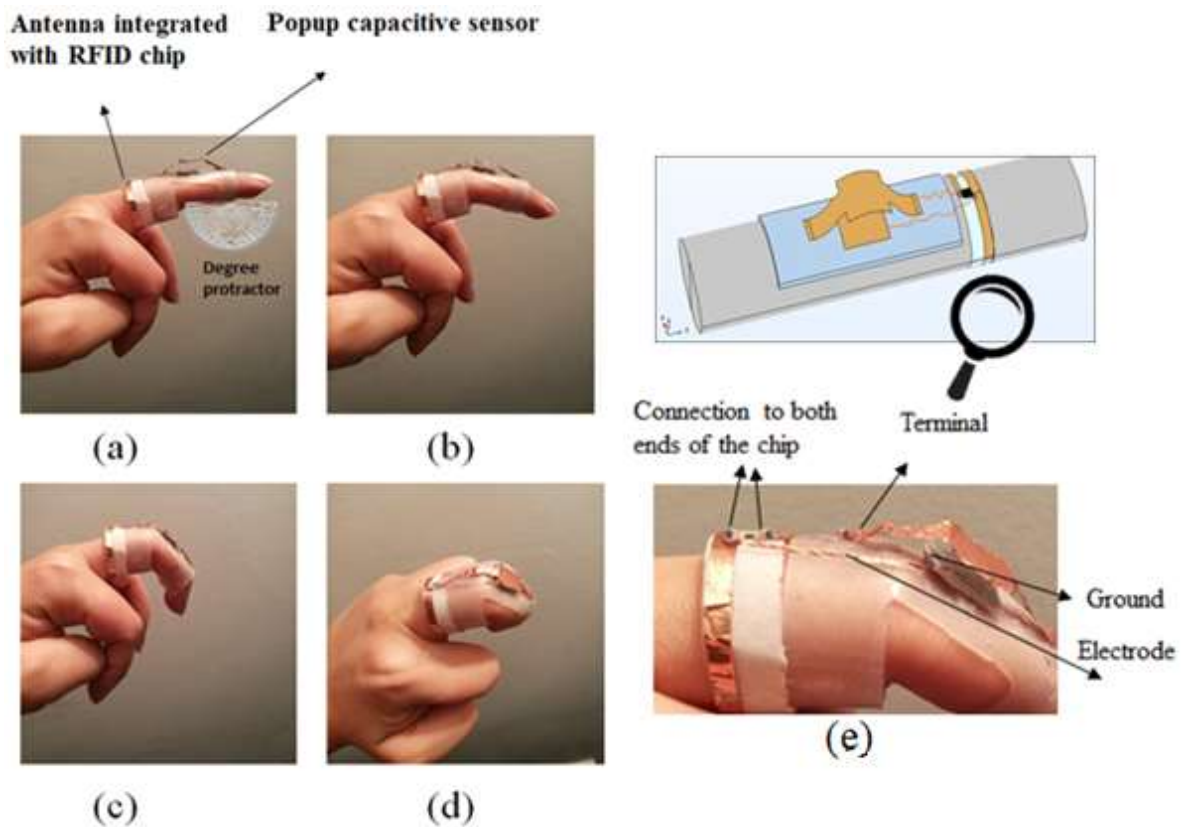


Fig. 4.8 Sensor prototype. (a) Straight finger, (b) 22.5 degree bending, (c) 45 degree and (d) 90 degree corresponding to fully bent finger. (e) Schematic of the sensor design with focus on the connection sites, two electrodes from ground and terminal of the popup capacitive sensor have been connected to both ends of the chip (black color).

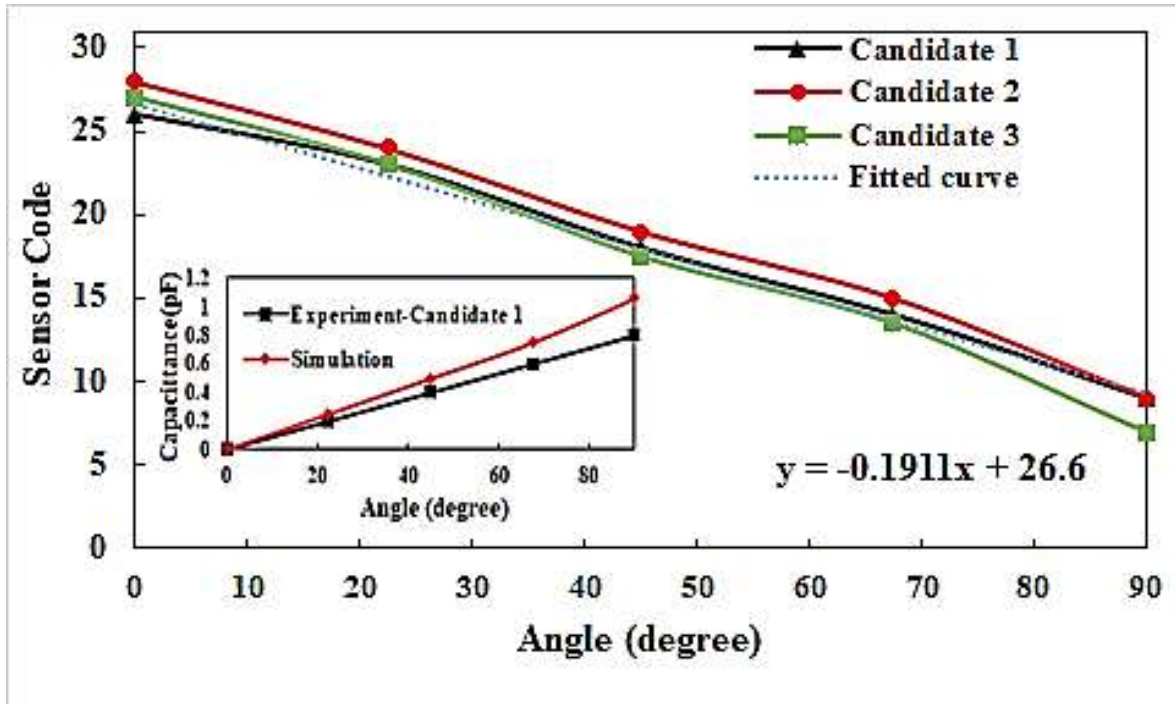


Fig. 4.9 Sensor code versus different degrees of finger bending. Inset graph illustrates a comparison between capacitance values obtained by simulation and experiment using the tag provider sample as reference [188]. This difference is mainly due to introduction of electrodes.

Fig. 4.9 shows the received sensor codes versus five degrees of finger bending which has been tested on three candidates.

Read ranges of 2.5 m for straight finger and 1.5 m at 866 MHz for fully bent finger has been achieved. This shows an average realized gain of -10 dB which shows improvement compared to the simulation which can be related to the difference between the phantom model and the actual test subject, as illustrated in Fig. 4.10. For achieving the maximum read range the RFID chip should face the Voyantic antenna. A 2.5 m read range for a small low-profile on-body RFID sensor is considered a very acceptable distance.

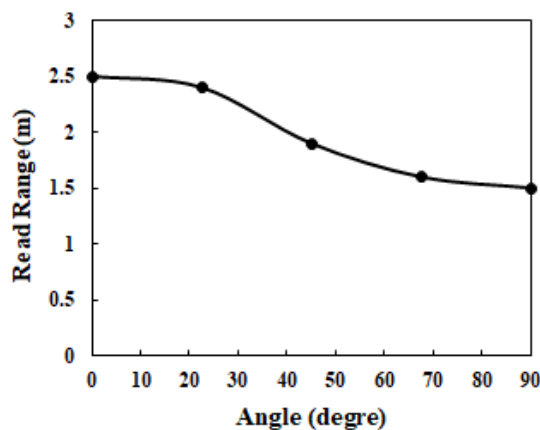


Fig. 4.10 Read range of the sensor on candidate 1 at different levels of finger bending.

#### **4.1.6 Conclusion**

The design and measurement of a wireless pop-up strain sensor is reported. This design consists of three main components, small loop antenna, pop-up capacitive sensor and RFID chip. The antenna has been matched to the input impedance of the RFID chip to resonate at European RFID band of 866 MHz. The capacitive sensor has been designed using compressive buckling technique and it is able to change the capacitance value with respect to the level of finger joint bending by buckling and thus changing the distance between the two plates. This capacitive sensor offers capacitance when moving from straight finger to a fully bent finger. Integrating the design with RFID chip makes it possible to detect this capacitance changes wirelessly by reading the sensor codes receiving from the reader. Read range of 2.5-1.5 m was achieved despite the compact sensor size and their proximity to the lossy human body.

# Conclusion and Recommendations for future works

---

## 5.1 Conclusions from this research

The research work presented in this thesis is concerned with the development of 3D pop-up strain sensors based on compressive buckling technique. Prototype systems, including pop-up antennas, pop-up FSS structures, pop-up capacitive sensors and RFID elements have been implemented and experimentally proven effective for the strain sensing measurement. The prototype system was extensively evaluated on laboratory-scale test rigs. Test results obtained have demonstrated that the developed system performs well under laboratory operating conditions. In this chapter, the conclusions that have been drawn from the research programme are summarised and the recommendations for future work are highlighted.

### 5.1.1 Modelling pop-up antennas

A numerical model of an 3D assembly of antennas based on compressive buckling technique for strain sensing application was established. Based on the developed model, the sensitivity, selectivity, frequency response and the fatigue profile of the system were analyzed. Moreover, the repeatability of the sensors was also defined. The effects of the geometric parameters of the 2D precursor on the performance of 3D final shape and subsequent optimization were achieved. For designing pop-up antennas, the following key parameters are recommended in consideration of modelling results:

- For designing and optimising the operation of pop-up sensors, multi-physics modelling is required. Thus the good knowledge of coupling of the different physics and using the data of each completed studies in another one and also optimising the features to avoid time consuming simulations by for example using shell for all thin ribbons or other useful boundary conditions to reduce the meshing are highly recommended.
- The supporting substrate must be modelled with hyperelastic option in COMSOL which provides more freedom to apply large deformations while fully recoverable.

- The copper sheet used in designing the pop-up sensors must be very thin (micro-meter scale) in order to be tolerable for elastomeric substrate. Otherwise, the substrate cannot bear the stretch-release mechanism or after a few cycles will fail.
- Choosing the right bonding locations plays a key role in designing small and at the same efficient antennas. In fact, the frequency shift which happens during the 3D conversion of the 2D precursor occurs due to creation of mutual capacitances. Therefore, by selecting the appropriate number of bonding sites and the right locations of them, we will be able to control the capacitive effect.
- When designing the 2D precursor of the antenna the maximum possible strain must be considered in choosing the feed gap length to avoid any collision and thus short circuit. This consideration also applies for defining an appropriate periodicity of pop-up FSS structures.
- By stacking several metal ribbons on each other and appropriately insulate them with glue or any other dielectrics, multiband operation can be achieved. The main step in this design is choosing the optimised dimension of the flat state to work at one of the applicable known frequency bands.

### **5.1.2 Integration of human body and pop-up antennas**

The electrical properties of human body tissues significantly affect the operation of the pop-up antennas. These interferences include a shift in frequency response of the antenna, a decrease in antenna gain and efficiency. Consideration of a layered human tissue modelling with their electrical properties is highly recommended. The Young's modulus of elastomeric substrates varies in the range of 10 kPa to a few MPa. The most available and cost-effective elastomeric substrate which matches well with flexibility of the human skin is Dragon skin which has been used in this thesis.

### **5.1.3 Integration of pop-up capacitive sensor with RFID technology**

As the compressive buckling methods can be applied to almost all available materials, it is possible to achieve bigger capacitance change range by making multi-layered electrodes including metal and dielectrics. In this thesis mylar layers have been used.

Integration of pop-up sensors with RFID technology for wireless sensing is one of the main contributions of this thesis. Single-chip sensing capability via affordable sensor tags enables substantially lower cost, easily deployed, maintenance-free, battery-free and multiple stimuli

monitoring platform. propose a passive UHF radio frequency identification tag design which can detect the level of strain.

## 5.2 Recommendations for future research

The research work presented in this thesis has demonstrated the viability and potential of pop-up sensors in the strain sensing. The strain parameter can be created directly by mechanical strain or indirectly by vapour swelling, temperature change, humidity, light emission and other parameters. In this thesis only two main parameter such as mechanical strain induced by skin and finger movement as well as vapor swelling have been studied. There are, however, other areas that need further research and improvements in the near future. The key areas are:

- Integration of pop-up sensors with stimuli-responsive polymers. These Responsive polymer-based materials can change their physical dimensions upon exposure to external stimulant such as temperature, humidity, etc.

Furthermore, there are a few lab-made polymers that can respond to a few stimuli at the same time. However, most of the available and studied stimuli-responsive polymers exhibits a very small dimension change in response of external stimulant. Therefore, more work is needed to improve these polymers to be expandable enough for the better performance of pop-up structures. The effect of sensing environment on the sensor performance is the other important factor to be considered.

For example, using pop-up antennas for humid sensing needs further consideration of the bonding method and also avoiding corrosion of the metal ribbon using as the antenna.

- Despite this significant progress, challenges remain, especially in structural designs to enable enhanced levels of comfort and minimally invasive bio-integration and to offer a high degree of mechanical deformability after solid encapsulation.

Further studies are needed to avoid the adverse effects of mechanical loads induced by the unmatched mechanical properties with the biological tissues such as cardiac muscle. developing structural substrate materials whose nonlinear, anisotropic stress–strain responses can accurately reproduce those of human tissues/organs in targeted applications, robably in a spatially variant manner is highly recommended. Encapsulation is essential in most practical applications, either to physically protect the surrounding tissues/organs, or to avoid the degradation of functional components due to the chemical reactions that can occur upon contact with biofluids.

- As the current introduced pop-up sensors are in 3D configurations, for on skin application they may cause some limitations such as difficulty in wearing cloths. Therefore, one solution can be encapsulation of these structures.
- These pop-up structures can be designed in a way to respond to stretch and release of the underlying elastomeric substrate by rotation of the selectively bonded pattern which can be used to design polarization reconfigurable pop-up antennas.

## References

- [1] Y. J. Hong *et al*, "Wearable and Implantable Devices for Cardiovascular Healthcare: from Monitoring to Therapy Based on Flexible and Stretchable Electronics," *Adv. Funct. Mater.*, vol. 29, (19), pp. 1808247, 2019.
- [2] H. Souri *et al*, "Wearable and Stretchable Strain Sensors: Materials, Sensing Mechanisms, and Applications," *Adv. Intell. Syst.*, vol. 2, (8), pp. 2000039, 2020.
- [3] H. Wu *et al*, "Energy Harvesters for Wearable and Stretchable Electronics: From Flexibility to Stretchability," *Adv Mater*, vol. 28, (45), pp. 9881-9919, 2016.
- [4] H. Jiang *et al*, "Mechanics of precisely controlled thin film buckling on elastomeric substrate," *Appl. Phys. Lett.*, vol. 90, (13), pp. 133119, 2007.
- [5] Z. Xue *et al*, "Mechanically-Guided Structural Designs in Stretchable Inorganic Electronics," *Adv Mater*, vol. 32, (15), pp. 1902254, 2020.
- [6] S. Xu *et al*, "Assembly of micro/nanomaterials into complex, three-dimensional architectures by compressive buckling," *Science*, vol. 347, (6218), pp. 154-159, 2015.
- [7] *COMSOL multi-physics v. 5.3 a. 2019. Online.* Available: [www.comsol.com](http://www.comsol.com).
- [8] T. Liimatta *et al*, "Inkjet printing in manufacturing of stretchable interconnects," in *2014 IEEE 64th Electronic Components and Technology Conference (ECTC)*, 2014, .
- [9] M. Mosallaei *et al*, "Geometry analysis in screen-printed stretchable interconnects," *IEEE Transactions on Components, Packaging and Manufacturing Technology*, vol. 8, (8), pp. 1344-1352, 2018.
- [10] J. Shao *et al*, "Nanoimprint lithography for the manufacturing of flexible electronics," *Science China Technological Sciences*, vol. 62, (2), pp. 175-198, 2019.
- [11] H. Yang, W. R. Leow and X. Chen, "3D printing of flexible electronic devices," *Small Methods*, vol. 2, (1), pp. 1700259, 2018.
- [12] L. Yin, J. Lv and J. Wang, "Structural Innovations in Printed, Flexible, and Stretchable Electronics," *Adv. Mater. Technol.*, vol. 5, (11), pp. 2000694, 2020.
- [13] Yuhao Liu, Matt Pharr and Giovanni Antonio Salvatore, "Lab-on-Skin: A Review of Flexible and Stretchable Electronics for Wearable Health Monitoring," *ACS Nano*, vol. 11, (10), pp. 9614–9635, 2018.
- [14] B. Wang, S. Bao and S. Vinnikova, "Buckling analysis in stretchable electronics," *Npj Flex Electron*, vol. 1, (5), 2017.
- [15] C. Wang *et al*, "Materials and Structures toward Soft Electronics," *Adv Mater*, vol. 30, (50), pp. 1801368, 2018.

- [16] S. Yao *et al*, "Nanomaterial-Enabled Flexible and Stretchable Sensing Systems: Processing, Integration, and Applications," *Adv Mater*, vol. 32, (15), pp. 1902343, 2020.
- [17] Fernandes Daniel Félix, Majidi Carmel and Tavakoli Mahmoud, "Digitally printed stretchable electronics: a review," *J. Mater. Chem. C*, vol. 7, (45), pp. 14035-14068, 2019.
- [18] T. Brittain Scott *et al*, "Microorigami: Fabrication of Small, Three-Dimensional, Metallic Structures," *J. Phys. Chem. B*, vol. 105, (2), pp. 347-350, 2001.
- [19] J. Overvelde, T. de Jong and Y. Shevchenko, "A three-dimensional actuated origami-inspired transformable metamaterial with multiple degrees of freedom," *Nat Commun*, vol. 10929, 2016.
- [20] A. Maziz *et al*, "Knitting and weaving artificial muscles," *Science Advances*, vol. 3, (1), pp. e1600327, 2017.
- [21] Hanqing Jiang *et al*, "Finite deformation mechanics in buckled thin films on compliant supports," *Proceedings of the National Academy of Sciences - PNAS*, vol. 104, (40), pp. 15607-15612, 2007.
- [22] Khang Dahl-Young, Rogers John A and H. Lee Hong, "Mechanical Buckling: Mechanics, Metrology, and Stretchable Electronics," *Adv. Funct. Mater*, vol. 19, (10), pp. 1526-1536, 2009.
- [23] N. Lu and D. Kim, "Flexible and Stretchable Electronics Paving the Way for Soft Robotics," *Soft Robotics*, vol. 1, (1), pp. 53-62, 2014.
- [24] Z. Yan *et al*, "Mechanical assembly of complex, 3D mesostructures from releasable multilayers of advanced materials," *Science Advances*, vol. 2, (9), pp. e1601014, 2016.
- [25] N. Lu and S. Yang, "Mechanics for stretchable sensors," *Current Opinion in Solid State and Materials Science*, vol. 19, (3), pp. 149-159, 2015.
- [26] H. Joo *et al*, "Material Design and Fabrication Strategies for Stretchable Metallic Nanocomposites," *Small*, vol. 16, (11), pp. 1906270, 2020.
- [27] S. Yang, E. Ng and N. Lu, "Indium Tin Oxide (ITO) serpentine ribbons on soft substrates stretched beyond 100%," *Extreme Mechanics Letters*, vol. 2, pp. 37-45, 2015.
- [28] Lv Jian *et al*, "Sweat-based wearable energy harvesting-storage hybrid textile devices," *Energy Environ. Sci.*, vol. 11, (12), pp. 3431-3442, 2018.
- [29] A. J. Bandodkar *et al*, "All-Printed Stretchable Electrochemical Devices," *Adv Mater*, vol. 27, (19), pp. 3060-3065, 2015.
- [30] L. Yin *et al*, "From All-Printed 2D Patterns to Free-Standing 3D Structures: Controlled Buckling and Selective Bonding," *Adv. Mater. Technol.*, vol. 3, (5), pp. 1800013, 2018.

- [31] Yihui Zhang *et al*, "Buckling in serpentine microstructures and applications in elastomer-supported ultra-stretchable electronics with high areal coverage," *Soft Matter*, vol. 9, (33), pp. 8062-8070, 2013.
- [32] D. Bishop, F. Pardo and C. Bolle, "Silicon Micro-Machines for Fun and Profit," *J Low Temp Phys*, vol. 169, pp. 386-399, 2021.
- [33] Ko Hyunhyub and Javey Ali, "Smart Actuators and Adhesives for Reconfigurable Matter," *Acc. Chem. Res*, vol. 50, (4), pp. 691–702, 2017.
- [34] K. Kuribayashi-Shigetomi, H. Onoe and S. Takeuchi, "Cell origami: self-folding of three-dimensional cell-laden microstructures driven by cell traction force," *PLoS One*, vol. 7, (12), 2012.
- [35] C. L. Randall, E. Gultepe and D. H. Gracias, "Self-folding devices and materials for biomedical applications," *Trends Biotechnol*, vol. 30, (3), pp. 138-146, 2012.
- [36] A. Cui *et al*, "nanograter" structures with unusual Fano resonances," *Light Sci Appl*, vol. 4, 2015.
- [37] Y. Tang *et al*, "Programmable Kiri-Kirigami Metamaterials," *Adv Mater*, vol. 29, (10), pp. 1604262, 2017.
- [38] Liu Qingchang and Xu Baoxing, "Two- and three-dimensional self-folding of free-standing graphene by liquid evaporation," *Soft Matter*, vol. 14, (29), pp. 5968-5976, 2018.
- [39] V. Y. Prinz, "A new concept in fabricating building blocks for nanoelectronic and nanomechanic devices," *Microelectronic Engineering*, vol. 69, (2), pp. 466-475, 2003.
- [40] O. Schmidt and K. Eberl, "Thin solid films roll up into nanotubes," *Nature*, vol. 168, pp. 410, 2001.
- [41] W. Pang *et al*, "Electro-mechanically controlled assembly of reconfigurable 3D mesostructures and electronic devices based on dielectric elastomer platforms," *National Science Review*, vol. 7, (2), pp. 342-354, 2020.
- [42] Py Charlotte *et al*, "Capillary Origami: Spontaneous Wrapping of a Droplet with an Elastic FSheet," *Phys. Rev. Lett.*, vol. 98, (15), 2007.
- [43] M. Jamal, A. Zarafshar and D. Gracias, "Differentially photo-crosslinked polymers enable self-assembling microfluidics," *Nat Commun*, vol. 2, (527), 2011.
- [44] H. C. Ko *et al*, "Curvilinear Electronics Formed Using Silicon Membrane Circuits and Elastomeric Transfer Elements," *Small*, vol. 5, (23), pp. 2703-2709, 2009.
- [45] H. Wu, W. Gao and Z. Yin, "Materials, Devices and Systems of Soft Bioelectronics for Precision Therapy," *Adv. Healthcare Mater.*, vol. 6, (10), pp. 1700017, 2017.
- [46] G. J. Lee *et al*, "Bioinspired Artificial Eyes: Optic Components, Digital Cameras, and Visual Prostheses," *Adv. Funct. Mater.*, vol. 28, (24), pp. 1705202, 2018.

- [47] S. Xu *et al*, "Materials science. Assembly of micro/nanomaterials into complex, three-dimensional architectures by compressive buckling," *Science (American Association for the Advancement of Science)*, vol. 347, (6218), pp. 154-159, 2015.
- [48] Zhang Yihui *et al*, "A mechanically driven form of Kirigami as a route to 3D mesostructures in micro/nanomembranes," *Proc Natl Acad Sci U S A*, vol. 112, (38), pp. 11757-11764, 2015.
- [49] Y. Liu *et al*, "Harnessing the interface mechanics of hard films and soft substrates for 3D assembly by controlled buckling," *Pnas*, vol. 116, pp. 15368-15377, .
- [50] H. Fu *et al*, "Morphable 3D mesostructures and microelectronic devices by multistable buckling mechanics," *Nature Materials*, vol. 17, (3), pp. 268-276, 2018.
- [51] Q. Zhang and J. Yin, "Spontaneous buckling-driven periodic delamination of thin films on soft substrates under large compression," *J. Mech. Phys. Solids*, vol. 118, pp. 40-57, 2018.
- [52] H. Luan *et al*, "Design and Fabrication of Heterogeneous, Deformable Substrates for the Mechanically Guided 3D Assembly," *ACS Appl Mater Interfaces*, vol. 11, (3), pp. 3482-3492, 2019.
- [53] L. Yin *et al*, "From All-Printed 2D Patterns to Free-Standing 3D Structures: Controlled Buckling and Selective Bonding," *Adv. Mater. Technol.*, vol. 3, (5), pp. 1800013, 2018.
- [54] Y. Ling *et al*, "Laser-Induced Graphene for Electrothermally Controlled, Mechanically Guided, 3D Assembly and Human-Soft Actuators Interaction," *Adv Mater*, vol. 32, (17), pp. 1908475, 2020.
- [55] W. Lee *et al*, "Two-dimensional materials in functional three-dimensional architectures with applications in photodetection and imaging," *Nat Commun*, vol. 9, 2018.
- [56] F. Zhang, F. Liu and Y. Zhang, "Analyses of mechanically-assembled 3D spiral mesostructures with applications as tunable inductors," *Science China Technological Sciences*, vol. 62, (2), pp. 243-251, 2019.
- [57] X. Guo *et al*, "Controlled mechanical assembly of complex 3D mesostructures and strain sensors by tensile buckling," *Npj Flexible Electronics*, vol. 2, (1), pp. 1-7, 2018.
- [58] Y. Liu *et al*, "Postbuckling analyses of frame mesostructures consisting of straight ribbons for mechanically guided three-dimensional assembly," *Proceedings of the Royal Society A*, vol. 475, (2225), pp. 20190012, 2019.
- [59] Z. Fan *et al*, "A finite deformation model of planar serpentine interconnects for stretchable electronics," *Int. J. Solids Structures*, vol. 91, pp. 46-54, 2016.
- [60] Y. Shi *et al*, "An analytic model of two-level compressive buckling with applications in the assembly of free-standing 3D mesostructures," *Soft Matter*, vol. 14, (43), pp. 8828-8837, 2018.

- [61] Fu Haoran *et al*, "Morphable 3D mesostructures and microelectronic devices by multistable buckling mechanics," 268–276, vol. 17, pp. 268–276, 2018.
- [62] H. Liu, Q. Li, *et al*, "Electrically conductive polymer composites for smart flexible strain sensors: a critical review", *J. Mater. Chem. C*, vol. 6, (45), pp. 12121-12141, 2018.
- [63] W. Lu, M. Jian, *et al*, "Hollow core–sheath nanocarbon spheres grown on carbonized silk fabrics for self-supported and nonenzymatic glucose sensing, *Nanoscale*, vol. 24, (11), pp. 11856-11863, 2019.
- [64] Y. Zou, P. Tan, B. Shi, *et al*, "A bionic stretchable nanogenerator for underwater sensing and energy harvesting", *Nat. Commun*, vol. 10, 2019.
- [65] X. Chen, K. Parida, J. Wang, *et al*, "A Stretchable and Transparent Nanocomposite Nanogenerator for Self-Powered Physiological Monitoring", *ACS Appl. Mater. Interfaces*, vol. 9, (48), pp. 42200-42209, 2017.
- [66] Z. Xie *et al*, "Flexible and Stretchable Antennas for Biointegrated Electronics," *Adv Mater*, vol. 32, (15), pp. 1902767, 2020.
- [67] J. Zhu and H. Cheng, "Recent development of flexible and stretchable antennas for bio-integrated electronics," *Sensors*, vol. 18, (12), pp. 4364, 2018.
- [68] J. Zhu *et al*, "Structural Design for Stretchable Microstrip Antennas," *ACS Applied Materials & Interfaces*, vol. 11, (9), pp. 8867-8877, 2019.
- [69] M. R. Ramli *et al*, "Stretchable Conductive Ink Based on Polysiloxane–Silver Composite and Its Application as a Frequency Reconfigurable Patch Antenna for Wearable Electronics," *ACS Applied Materials & Interfaces*, vol. 11, (31), pp. 28033-28042, 2019.
- [70] A. Ghasemi and E. S. Sousa, "Spectrum sensing in cognitive radio networks: requirements, challenges and design trade-offs," *IEEE Communications Magazine*, vol. 46, (4), pp. 32-39, 2008.
- [71] H. Zahir *et al*, "Design fabrication and characterisation of polyaniline and multiwall carbon nanotubes composites-based patch antenna," *IET Microwaves, Antennas & Propagation*, vol. 10, (1), pp. 88-93, 2016.
- [72] K. Shin, S. Cho and J. Jang, "Graphene/Polyaniline/Poly (4-styrenesulfonate) Hybrid Film with Uniform Surface Resistance and Its Flexible Dipole Tag Antenna Application," *Small*, vol. 9, (22), pp. 3792-3798, 2013.
- [73] A. R. Ravindran *et al*, "Effects of graphene nanoplatelet size and surface area on the AC electrical conductivity and dielectric constant of epoxy nanocomposites," *Polymers*, vol. 10, (5), pp. 477, 2018.
- [74] H. A. E. Elobaid *et al*, "A transparent and flexible polymer-fabric tissue UWB antenna for future wireless networks," *IEEE Antennas and Wireless Propagation Letters*, vol. 16, pp. 1333-1336, 2016.

- [75] T. Leng *et al*, "Graphene nanoflakes printed flexible meandered-line dipole antenna on paper substrate for low-cost RFID and sensing applications," *IEEE Antennas and Wireless Propagation Letters*, vol. 15, pp. 1565-1568, 2016.
- [76] X. Zhou *et al*, "Graphene printed flexible and conformal array antenna on paper substrate for 5.8 GHz wireless communications," in *2020 14th European Conference on Antennas and Propagation (EuCAP)*, 2020, .
- [77] W. Li *et al*, "Compact inkjet-printed flexible MIMO antenna for UWB applications," *IEEE Access*, vol. 6, pp. 50290-50298, 2018.
- [78] S. G. Kirtania *et al*, "Flexible Antennas: A Review," *Micromachines*, vol. 11, (9), pp. 847, 2020.
- [79] W. T. Li *et al*, "Inkjet printing of wideband stacked microstrip patch array antenna on ultrathin flexible substrates," *IEEE Transactions on Components, Packaging and Manufacturing Technology*, vol. 8, (9), pp. 1695-1701, 2018.
- [80] S. Das and D. Mitra, "A compact wideband flexible implantable slot antenna design with enhanced gain," *IEEE Transactions on Antennas and Propagation*, vol. 66, (8), pp. 4309-4314, 2018.
- [81] M. Rizwan *et al*, "Possibilities of fabricating copper-based RFID tags with photonic-sintered inkjet printing and thermal transfer printing," *IEEE Antennas and Wireless Propagation Letters*, vol. 16, pp. 1828-1831, 2017.
- [82] S. M. Saeed, C. A. Balanis and C. R. Birtcher, "Inkjet-printed flexible reconfigurable antenna for conformal WLAN/WiMAX wireless devices," *IEEE Antennas and Wireless Propagation Letters*, vol. 15, pp. 1979-1982, 2016.
- [83] K. Saraswat and A. R. Harish, "Flexible dual-band dual-polarised CPW-fed monopole antenna with discrete-frequency reconfigurability," *IET Microwaves, Antennas & Propagation*, vol. 13, (12), pp. 2053-2060, 2019.
- [84] M. A. Riheen *et al*, "Inkjet-printed cpw fed wideband bowtie slot antenna on PET substrate for flexible iot applications," in *ECS Meeting Abstracts*, 2020, .
- [85] S. F. Jilani and A. Alomainy, "Planar millimeter-wave antenna on low-cost flexible PET substrate for 5G applications," in *2016 10th European Conference on Antennas and Propagation (EuCAP)*, 2016, .
- [86] S. Pacchini *et al*, "Inkjet-printing of hybrid ag/conductive polymer towards stretchable microwave devices," in *2015 European Microwave Conference (EuMC)*, 2015, .
- [87] J. Hou, L. Qu and W. Shi, "A survey on internet of things security from data perspectives," *Computer Networks*, vol. 148, pp. 295-306, 2019.
- [88] D. Qi *et al*, "Stretchable Electronics Based on PDMS Substrates," *Adv Mater*, pp. 2003155, 2020.

- [89] D. E. Anagnostou *et al*, "A direct-write printed antenna on paper-based organic substrate for flexible displays and WLAN applications," *Journal of Display Technology*, vol. 6, (11), pp. 558-564, 2010.
- [90] Y. Wang *et al*, "Flexible RFID Tag Metal Antenna on Paper-Based Substrate by Inkjet Printing Technology," *Adv. Funct. Mater.*, vol. 29, (29), pp. 1902579, 2019.
- [91] G. DeJean *et al*, "Liquid crystal polymer (LCP): A new organic material for the development of multilayer dual-frequency/dual-polarization flexible antenna arrays," *IEEE Antennas and Wireless Propagation Letters*, vol. 4, pp. 22-26, 2005.
- [92] M. Venkateswara Rao *et al*, "Circularly polarized flexible antenna on liquid crystal polymer substrate material with metamaterial loading," *Microwave Opt Technol Lett*, vol. 62, (2), pp. 866-874, 2020.
- [93] A. Rida *et al*, "Inkjet-printing UHF antenna for RFID and sensing applications on liquid crystal polymer," in *2009 IEEE Antennas and Propagation Society International Symposium*, 2009, .
- [94] S. Soltani and J. C. Batchelor, "Highly flexible strain sensor based on pop-up dipole antenna for on-body applications," 2018.
- [95] A. Benchirouf *et al*, "Flexible Strain Sensor based Microstrip Patch Antenna," 2015 .
- [96] D. Tang *et al*, "Highly sensitive wearable sensor based on a flexible multi-layer graphene film antenna," *Science Bulletin*, vol. 63, (9), pp. 574-579, 2018.
- [97] S. Kanaparthi, V. R. Sekhar and S. Badhulika, "Flexible, eco-friendly and highly sensitive paper antenna based electromechanical sensor for wireless human motion detection and structural health monitoring," *Extreme Mechanics Letters*, vol. 9, pp. 324-330, 2016.
- [98] U. Tata *et al*, "Exploiting a patch antenna for strain measurements," *Measurement Science and Technology*, vol. 20, (1), pp. 015201, 2008.
- [99] X. Chen, L. Ukkonen and T. Björninen, "Passive E-textile UHF RFID-based wireless strain sensors with integrated references," *IEEE Sensors Journal*, vol. 16, (22), pp. 7835-7836, 2016.
- [100] P. Martins, R. M. Natal Jorge and A. Ferreira, "A comparative study of several material models for prediction of hyperelastic properties: Application to silicone-rubber and soft tissues," *Strain*, vol. 42, (3), pp. 135-147, 2006.
- [101] M. A. Ziai and J. C. Batchelor, "Temporary on-skin passive UHF RFID transfer tag," *IEEE Transactions on Antennas and Propagation*, vol. 59, (10), pp. 3565-3571, 2011.
- [102] *Tissue properties database | IT IS Foundation [online]*, available: <https://itis.swiss/virtual-population/tissue-properties/database/dielectric-properties/>
- [103] O. Olaode, "Esearch and Development of Low-Profile, Small Footprint Antennas for VHF-UHF Range Applications." , Duke University, 2012.

- [104] S. Soltani, P. S. Taylor and J. C. Batchelor, "A dual-band strain sensor based on pop-up half wavelength dipole antenna," in *2019 IEEE International Symposium on Antennas and Propagation and USNC-URSI Radio Science Meeting*, 2019, .
- [105] H. Nakamoto *et al*, "Stretchable strain sensor with anisotropy and application for joint angle measurement," *IEEE Sensors Journal*, vol. 16, (10), pp. 3572-3579, 2016.
- [106] H. A. H. Omer *et al*, "Structural health monitoring sensor based on a flexible microstrip patch antenna," *Indonesian J.Electr.Eng.Comp.Sci*, vol. 10, pp. 917-924, 2018.
- [107] S. Jang and J. Kim, "Passive wireless structural health monitoring sensor made with a flexible planar dipole antenna," *Smart Mater. Struct.*, vol. 21, (2), pp. 027001, 2012.
- [108] A. Daliri *et al*, "Circular microstrip patch antenna strain sensor for wireless structural health monitoring," in *Proceedings of the World Congress on Engineering*, 2010, .
- [109] Z. Qian *et al*, "Analysis and design of a strain sensor based on a microstrip patch antenna," in *2012 International Conference on Microwave and Millimeter Wave Technology (ICMMT)*, 2012, .
- [110] S. Soltani, P. S. Taylor and J. C. Batchelor, "Mechanically influenced antennas for strain sensing applications using multiphysics modelling," in *2020 14th European Conference on Antennas and Propagation (EuCAP)*, 2020, .
- [111] C. Wang *et al*, "Materials and structures toward soft electronics," *Adv Mater*, vol. 30, (50), pp. 1801368, 2018.
- [112] J. Visser *et al*, "Reinforcement of hydrogels using three-dimensionally printed microfibrils," *Nature Communications*, vol. 6, (1), pp. 1-10, 2015.
- [113] C. Votzke *et al*, "3D-printed liquid metal interconnects for stretchable electronics," *IEEE Sensors Journal*, vol. 19, (10), pp. 3832-3840, 2019.
- [114] W. Dang *et al*, "Hybrid structure of stretchable interconnect for reliable E-skin application," in *2017 IEEE 26th International Symposium on Industrial Electronics (ISIE)*, 2017, .
- [115] A. Kiourti and J. L. Volakis, "Stretchable and flexible E-fiber wire antennas embedded in polymer," *IEEE Antennas and Wireless Propagation Letters*, vol. 13, pp. 1381-1384, 2014.
- [116] K. Pan *et al*, "Soft Wireless Battery-Free UHF RFID Stretchable Sensor Based on Microfluidic Technology," *IEEE Journal of Radio Frequency Identification*, vol. 3, (4), pp. 252-258, 2019.
- [117] Z. Li *et al*, "Rational Design of a Printable, Highly Conductive Silicone-based Electrically Conductive Adhesive for Stretchable Radio-Frequency Antennas," *Advanced Functional Materials*, vol. 25, (3), pp. 464-470, 2015.
- [118] *Circuit explore air machine*. Available: <https://www.hobbycraft.co.uk>.

- [119] *Smooth-on Dragon Skin, FX-Pro*, available: <https://www.smooth-on.com/product-line/dragon-skin>.
- [120] *Dak 3.5 | SPEAG*. Accessed: June 06, 2018. [Online], available:<https://www.speag.com/products/dak/dak-dielectric-probe-systems/dak-3-5-200-mhz-20-ghz>.
- [121] S. Soltani *et al*, "Antenna-Based Pop-up Vapor Sensor Guided by Controlled Compressive Buckling," *IEEE Sensors Journal*, vol. 20, (5), pp. 2304-2312, 2019.
- [122] S. Singh, "Sensors—An effective approach for the detection of explosives," *J. Hazard. Mater.*, vol. 144, (1-2), pp. 15-28, 2007.
- [123] *Hazardous Substance Fact Sheet | New Jersey Department of Health and Senior Services, 1996*, available: <https://nj.gov/health/eoh/rtkweb/documents/fs/0701.pdf>, [Accessed: April-2002].
- [124] *Dak 3.5 | SPEAG*. Accessed: June 06, 2018. [Online]. Available: <https://www.speag.com/products/dak/dak-dielectric-probe-systems/dak-3-5-200-mhz-20-ghz>.
- [125] H. Lee *et al*, "Carbon-nanotube loaded antenna-based ammonia gas sensor," *IEEE Trans. Microwave Theory Tech.*, vol. 59, (10), pp. 2665-2673, 2011.
- [126] K. G. Ong, K. Zeng and C. A. Grimes, "A wireless, passive carbon nanotube-based gas sensor," *IEEE Sensors Journal*, vol. 2, (2), pp. 82-88, 2002.
- [127] H. Lee *et al*, "A novel highly-sensitive antenna-based "smart skin" gas sensor utilizing carbon nanotubes and inkjet printing," in *2011 IEEE International Symposium on Antennas and Propagation (APSURSI)*, 2011, .
- [128] M. M. Tentzeris and S. Nikolaou, "RFID-enabled ultrasensitive wireless sensors utilizing inkjet-printed antennas and carbon nanotubes for gas detection applications," in *2009 IEEE International Conference on Microwaves, Communications, Antennas and Electronics Systems*, 2009, .
- [129] K. Na *et al*, "Graphene-based wireless environmental gas sensor on PET substrate," *IEEE Sensors Journal*, vol. 16, (12), pp. 5003-5009, 2016.
- [130] ]B. Wu *et al*, "High-performance wireless ammonia gas sensors based on reduced graphene oxide and nano-silver ink hybrid material loaded on a patch antenna," *Sensors*, vol. 17, (9), pp. 2070, 2017.
- [131] A. Quddious *et al*, "Disposable, paper-based, inkjet-printed humidity and H<sub>2</sub>S gas sensor for passive sensing applications," *Sensors*, vol. 16, (12), pp. 2073, 2016.
- [132] M. D. Balachandran *et al*, "SnO<sub>2</sub> capacitive sensor integrated with microstrip patch antenna for passive wireless detection of ethylene gas," *Electron. Lett.*, vol. 44, (7), pp. 464-466, 2008.

- [133] M. H. Zarifi *et al*, "Detection of volatile organic compounds using microwave sensors," *IEEE Sensors Journal*, vol. 15, (1), pp. 248-254, 2014.
- [134] H. Guo *et al*, "PDMS-coated piezoresistive NEMS diaphragm for chloroform vapor detection," *IEEE Electron Device Lett.*, vol. 33, (7), pp. 1078-1080, 2012.
- [135] A. Sohrabi *et al*, "A novel technique for rapid vapor detection using swelling polymer covered microstrip ring resonator," in *2014 IEEE MTT-S International Microwave Symposium (IMS2014)*, 2014, .
- [136] X. Ning *et al*, "PDMS-coated fiber volatile organic compounds sensors," *Appl. Opt.*, vol. 55, (13), pp. 3543-3548, 2016.
- [137] U. Altenberend *et al*, "Contribution of polymeric swelling to the overall response of capacitive gas sensors," *Analytical and Bioanalytical Chemistry*, vol. 405, (20), pp. 6445-6452, 2013.
- [138] N. Gao *et al*, "Polymer swelling induced conductive wrinkles for an ultrasensitive pressure sensor," *ACS Macro Letters*, vol. 5, (7), pp. 823-827, 2016.
- [139] S. H. Jeong *et al*, "PDMS-based elastomer tuned soft, stretchable, and sticky for epidermal electronics," *Adv Mater*, vol. 28, (28), pp. 5830-5836, 2016.
- [140] C. Martínez-Hipatl *et al*, "Detection of volatile organic compounds by an interferometric sensor," *Sensors Actuators B: Chem.*, vol. 147, (1), pp. 37-42, 2010.
- [141] H. Chang *et al*, "Ultra-fast responsive colloidal-polymer composite-based volatile organic compounds (VOC) sensor using nanoscale easy tear process," *Scientific Reports*, vol. 8, (1), pp. 1-11, 2018.
- [142] N. Tiercelin *et al*, "Polydimethylsiloxane membranes for millimeter-wave planar ultra flexible antennas," *J Micromech Microengineering*, vol. 16, (11), pp. 2389, 2006.
- [143] Q. Tang *et al*, "Frequency-tunable soft composite antennas for wireless sensing," *Sensors and Actuators A: Physical*, vol. 179, pp. 137-145, 2012.
- [144] H. Kou *et al*, "Wireless flexible pressure sensor based on micro-patterned Graphene/PDMS composite," *Sensors and Actuators A: Physical*, vol. 277, pp. 150-156, 2018.
- [145] A. Nag *et al*, "A transparent strain sensor based on PDMS-embedded conductive fabric for wearable sensing applications," *IEEE Access*, vol. 6, pp. 71020-71027, 2018.
- [146] M. Liu *et al*, "Thickness-dependent mechanical properties of polydimethylsiloxane membranes," *J Micromech Microengineering*, vol. 19, (3), pp. 035028, 2009.
- [147] C. V. Rumens *et al*, "Swelling of PDMS networks in solvent vapours; applications for passive RFID wireless sensors," *Journal of Materials Chemistry C*, vol. 3, (39), pp. 10091-10098, 2015.

- [148] K. E. Belsey *et al*, "Switchable disposable passive RFID vapour sensors from inkjet printed electronic components integrated with PDMS as a stimulus responsive material," *Journal of Materials Chemistry C*, vol. 5, (12), pp. 3167-3175, 2017.
- [149] S. Xu *et al*, "Assembly of micro/nanomaterials into complex, three-dimensional architectures by compressive buckling," *Science*, vol. 347, (6218), pp. 154-159, 2015.
- [150] Y. Zhang *et al*, "A mechanically driven form of Kirigami as a route to 3D mesostructures in micro/nanomembranes," *Proceedings of the National Academy of Sciences*, vol. 112, (38), pp. 11757-11764, 2015.
- [151] L. Gao *et al*, "Optics and nonlinear buckling mechanics in large-area, highly stretchable arrays of plasmonic nanostructures," *Acs Nano*, vol. 9, (6), pp. 5968-5975, 2015.
- [152] Z. Yan *et al*, "Controlled mechanical buckling for origami-inspired construction of 3D microstructures in advanced materials," *Advanced Functional Materials*, vol. 26, (16), pp. 2629-2639, 2016.
- [153] R. Li *et al*, "An analytical mechanics model for the island-bridge structure of stretchable electronics," *Soft Matter*, vol. 9, (35), pp. 8476-8482, 2013.
- [154] H. Wang *et al*, "Vibration of mechanically-assembled 3D microstructures formed by compressive buckling," *J. Mech. Phys. Solids*, vol. 112, pp. 187-208, 2018.
- [155] S. Li *et al*, "Mechanics of buckled serpentine structures formed via mechanics-guided, deterministic three-dimensional assembly," *J. Mech. Phys. Solids*, vol. 125, pp. 736-748, 2019.
- [156] T. G. Tang, Q. M. Tieng and M. W. Gunn, "Equivalent circuit of a dipole antenna using frequency-independent lumped elements," *IEEE Transactions on Antennas and Propagation*, vol. 41, (1), pp. 100-103, 1993.
- [157] O. O. Olaode, W. D. Palmer and W. T. Joines, "Characterization of meander dipole antennas with a geometry-based, frequency-independent lumped element model," *IEEE Antennas and Wireless Propagation Letters*, vol. 11, pp. 346-349, 2012.
- [158] W. Mönch *et al*, "Flory-Huggins swelling of polymer Bragg mirrors," *Appl. Phys. Lett.*, vol. 89, (16), pp. 164104, 2006.
- [159] D. Armani, C. Liu and N. Aluru, "Re-configurable fluid circuits by PDMS elastomer micromachining," in *Technical Digest. IEEE International MEMS 99 Conference. Twelfth IEEE International Conference on Micro Electro Mechanical Systems (Cat. no. 99CH36291)*, 1999, .
- [160] P. Martins, R. M. Natal Jorge and A. Ferreira, "A comparative study of several material models for prediction of hyperelastic properties: Application to silicone-rubber and soft tissues," *Strain*, vol. 42, (3), pp. 135-147, 2006.
- [161] *T-Ceram RF and Microwave Company*, available: <http://www.t-ceram.com>.

- [162] *Load Ramping of Nonlinear Problems,* Comsol Blog, available: <https://uk.comsol.com/blogs/load-ramping-nonlinear-problems>.
- [163] W. Schütz, "A history of fatigue," *Eng. Fract. Mech.*, vol. 54, (2), pp. 263-300, 1996.
- [164] M. Abdolrazzaghi, N. Kazemi and M. Daneshmand, "Sensitive spectroscopy using DSR array and linvill negative impedance," in *2019 IEEE MTT-S International Microwave Symposium (IMS)*, 2019, .
- [165] M. Abdolrazzaghi and M. Daneshmand, "Sensitivity optimization in SRRs using interferometry phase cancellation," in *2019 IEEE MTT-S International Microwave Symposium (IMS)*, 2019, .
- [166] M. Abdolrazzaghi, M. Daneshmand and A. K. Iyer, "Strongly enhanced sensitivity in planar microwave sensors based on metamaterial coupling," *IEEE Trans. Microwave Theory Tech.*, vol. 66, (4), pp. 1843-1855, 2018.
- [167] S. Soltani *et al*, "Pop-up Tunable Frequency Selective Surfaces for Strain Sensing," *IEEE Sensors Letters*, vol. 4, (4), pp. 1-4, 2020.
- [168] R. S. Anwar, L. Mao and H. Ning, "Frequency selective surfaces: a review," *Applied Sciences*, vol. 8, (9), pp. 1689, 2018.
- [169] Y. Cui *et al*, "A novel tunable FSS of miniaturized unit cell for lower frequency," in *2018 International Applied Computational Electromagnetics Society Symposium-China (ACES)*, 2018, .
- [170] B. Sanz-Izquierdo and E. A. Parker, "3-D printing of elements in frequency selective arrays," *IEEE Transactions on Antennas and Propagation*, vol. 62, (12), pp. 6060-6066, 2014.
- [171] T. K. Chang, R. J. Langley and E. A. Parker, "Frequency selective surfaces on biased ferrite substrates," *Electron. Lett.*, vol. 30, (15), pp. 1193-1194, 1994.
- [172] A. D. Lima, E. A. Parker and R. J. Langley, "Tunable frequency selective surface using liquid substrates," *Electron. Lett.*, vol. 30, (4), pp. 281-282, 1994.
- [173] E. A. Parker and S. B. Savia, "Active frequency selective surfaces with ferroelectric substrates," *IEE Proceedings-Microwaves, Antennas and Propagation*, vol. 148, (2), pp. 103-108, 2001.
- [174] D. Ferreira *et al*, "3-D mechanically tunable square slot FSS," *IEEE Transactions on Antennas and Propagation*, vol. 65, (1), pp. 242-250, 2016.
- [175] M. Mahmoodi and K. M. Donnell, "Performance metrics for frequency selective surface-based sensors," *IEEE Sensors Letters*, vol. 1, (6), pp. 1-4, 2017.
- [176] E. Kinzel, "Design of a frequency-selective surface strain sensor," in *2014 IEEE Antennas and Propagation Society International Symposium (APSURSI)*, 2014, .

- [177] Y. Cao *et al*, "Direct fabrication of stretchable electronics on a polymer substrate with process-integrated programmable rigidity," *Advanced Functional Materials*, vol. 28, (50), pp. 1804604, 2018.
- [178] M. Cai *et al*, "Soft elastomers with programmable stiffness as strain-isolating substrates for stretchable electronics," *ACS Applied Materials & Interfaces*, vol. 11, (15), pp. 14340-14346, 2019.
- [179] P. B. Shull *et al*, "Hand gesture recognition and finger angle estimation via wrist-worn modified barometric pressure sensing," *IEEE Transactions on Neural Systems and Rehabilitation Engineering*, vol. 27, (4), pp. 724-732, 2019.
- [180] Z. Shen *et al*, "A soft stretchable bending sensor and data glove applications," *Robotics and Biomimetics*, vol. 3, (1), pp. 22, 2016.
- [181] D. Lin, "A test bed for detecting and mimicking finger joint bending," in *2016 IEEE MIT Undergraduate Research Technology Conference (URTC)*, 2016, .
- [182] V. Stornelli *et al*, "A 10-17 DOF sensory gloves with harvesting capability for smart healthcare," *Journal of Communications Software and Systems*, vol. 15, (2), pp. 166-172, 2019.
- [183] M. Borghetti, E. Sardini and M. Serpelloni, "Sensorized glove for measuring hand finger flexion for rehabilitation purposes," *IEEE Transactions on Instrumentation and Measurement*, vol. 62, (12), pp. 3308-3314, 2013.
- [184] A. Leoni *et al*, "A human body powered sensory glove system based on multisource energy harvester," in *2018 14th Conference on Ph. D. Research in Microelectronics and Electronics (PRIME)*, 2018, .
- [185] B. Lin *et al*, "A modular data glove system for finger and hand motion capture based on inertial sensors," *Journal of Medical and Biological Engineering*, vol. 39, (4), pp. 532-540, 2019.
- [186] H. Ryu *et al*, "A knitted glove sensing system with compression strain for finger movements," *Smart Mater. Struct.*, vol. 27, (5), pp. 055016, 2018.
- [187] B. Lin *et al*, "Design of an inertial-sensor-based data glove for hand function evaluation," *Sensors*, vol. 18, (5), pp. 1545, 2018.
- [188] J. W. Park *et al*, "Measurement of finger joint angle using stretchable carbon nanotube strain sensor," *PloS One*, vol. 14, (11), pp. e0225164, 2019.
- [189] C. K. Jha and A. L. Chakraborty, "A fiber bragg grating strain sensor-based glove to accurately measure the bend angle of the finger flexed at the proximal interphalangeal joints," in *2018 Ieee Sensors*, 2018, .
- [190] X. Li *et al*, "An ultra-flexible polyurethane yarn-based wearable strain sensor with a polydimethylsiloxane infiltrated multilayer sheath for smart textiles," *Nanoscale*, vol. 12, (6), pp. 4110-4118, 2020.

- [191] X. Liu *et al*, "A highly sensitive graphene woven fabric strain sensor for wearable wireless musical instruments," *Materials Horizons*, vol. 4, (3), pp. 477-486, 2017.
- [192] RfMicron Magnus S2 transponder chip, available: <http://rfmicron.com/magnus-family/>
- [193] P. S. Taylor and J. C. Batchelor, "Finger-Worn UHF Far-Field RFID Tag Antenna," *IEEE Antennas and Wireless Propagation Letters*, vol. 18, (12), pp. 2513-2517, 2019.
- [194] D. J. Healy, "An examination of the Gamma match," *Qst*, vol. 57, pp. 11-15, 1969.
- [195] *CST-Dassault Systemes, Oct. 2018, [online] Available:www.cst.com.*
- [196] S. Soltani and J. C. Batchelor, "Highly flexible strain sensor based on pop-up dipole antenna for on-body applications," 2018.
- [197] Y. Chen, "Arthroscopy of the wrist and finger joints." *Orthop. Clin. North Am.*, vol. 10, (3), pp. 723-733, 1979.
- [198] I. Ullah *et al*, "RFID AC Current Sensing Technique," *IEEE Sensors Journal*, vol. 20, (4), pp. 2197-2204, 2019.
- [199] X. Cheng and Y. Zhang, "Micro/nanoscale 3D assembly by rolling, folding, curving, and buckling approaches," *Adv Mater*, vol. 31, (36), pp. 1901895, 2019.
- [200] Z. Yan *et al*, "Deterministic assembly of 3D mesostructures in advanced materials via compressive buckling: a short review of recent progress," *Extreme Mechanics Letters*, vol. 11, pp. 96-104, 2017.